Hydrogen doping for controlling electrical properties of p- and n-type oxide semiconductors for thin-film transistors

by

Rostislav Velichko

Student ID Number: 1236002

A dissertation submitted to the
Engineering course, Department of Engineering,
Graduate School of Engineering,
Kochi University of Technology,
Kochi, Japan

in partial fulfillment of the requirements for the degree of
Doctor of Engineering

Assessment Committee:

Supervisor: Mamoru Furuta
Co-Supervisor: Norbert Fruehauf, University of Stuttgart
Co-Supervisor: Hisao Makino
Hiroshi Furuta
Chaoyang Li

March 2022

Abstract

Hydrogen doping for controlling electrical properties of p- and n-type oxide semiconductors for thin-film transistors

Modern society is directly connected with the development of digital and information technology, while about 70% of all everyday information is perceived through vision. In addition, during the worldwide pandemic of the COVID-19, interaction and remote working have increased and become massively ubiquitous. All these attributes of daily activity are inevitably associated with displays interaction, which have become an integral part of our life. Current trends in the technology of flat panel display (FPD) are aimed for improving the image quality, increasing the refresh rate of the displayed image, increasing the resolution, the creation of flexible devices and so-called "transparent electronics". However, the development of next-generation displays requires improvements in the performance of the thin-film transistors (TFTs) that drive the individual image pixels, and make up the active control matrix of the liquid crystal display (LCD). Ultimately, it is clear that the development of semiconductor materials that can meet the requirements of future FPD parameters is a key goal. From the beginning of the 2000s, both amorphous and polycrystalline oxide semiconductors (OS) have been shown to be promising candidates to replace amorphous silicon technology. Owing better properties, including high mobility of over 10 cm^2/Vs, high transparency, and synthesis at a room temperature. Currently, there is a need to further improve the OS based TFT mobility.

Since the unique structure of OS consists of a large spatial overlap of metal *s*-orbitals without a pronounced directionality, forming the bottom of the conduction band (CBM), while the top of valence band (VBM) is formed by oxygen *p*-orbitals, which ensures their high transparency. However, OS synthesis is always accompanied by the formation of various high-density defects due to oxygen deficiency. Thus, we propose a method of synthesizing OS in a hydrogen-containing atmosphere, which is one of the ways to control the electrical properties, as well as a way to passivate defects improving the device characteristics. Nevertheless, despite the fact that H is the most common impurity, its role and influence in each particular case can vary significantly. This

fact requires further study and comprehensive analysis, while the mechanism in each specific case still remains without proper explanation.

In this study, in order to improve electrical properties of the p- and n-type OS, the effects of H doping in OS for TFT application were studied. The H adding effect was investigated in the three following topics: 1) Hydrogen doping effect in polycrystalline SnO_x for p-type conductivity TFT; 2) Defect passivation and carrier reduction mechanisms in hydrogen doped n-type In-Ga-Zn-O (IGZO:H) films upon low-temperature annealing for flexible device applications; 3) Hydrogenated polycrystalline n-type In-Ga-O (IGO:H) for high-mobility TFTs.

The purpose of this dissertation is to study the effects of H doping to improve the electrical properties of OSs, to establish the mechanism of H influence in p- and n-type OS, and to determine the positive and negative effects of H addition both on the properties of thin films and on the characteristics of devices. This thesis is organized as follows through the 5 chapters.

Chapter 1 is an overview of main directions of the development of FPD technology. The main stages and history of the OS development are considered. Key features, unique structure and characteristics, advantages and disadvantages of both polycrystalline and amorphous OS are summarized and presented, as well as the main trends in the development and their device applications. The focus of the chapter is on the role and effect of hydrogen in OS. The main known effects, including change in electrical properties, passivation of defects, and improvement of device performance and what role H plays are discussed.

Chapter 2 describes the research of OS with p-type conductivity based on tin oxide (SnO_x) for TFT application. Most of the OS materials are those with n-type conductivity. However, p-type materials development is important because achieving high performance p-type oxide TFTs will promote a new era for electronics in rigid and flexible substrates. In addition, it will allow the production of complementary metal-oxide-semiconductor (CMOS) logic devices and make possible use of highly compact circuits with low power consumption.

Optimization and development of a reference synthesis process for obtaining the films with p-type conductivity is presented. Both the comprehensive analysis of thin-film properties and the fabrication of TFTs confirming the nature of p-type conductivity were performed. A basic optimal process window was developed, which is very narrow and limited to control due to the rapid and easy oxidation of Sn in oxygen-excess condition and the instability of SnO at 250 °C.

In order to optimize and improve the characteristics of both the thin-films and TFT, we focused on the H doping to SnO_x films. The effects of different H ratios on the change of optical, structural, electrical properties, chemical composition, and TFT performance were investigated. Both the positive and negative effects of H doped SnO_x films were found. Thus, it was found that H doping resulted in the change of the initial Sn/SnO/SnO_2 phase composition. Initial metal content in the film decreased by 3% suggesting additional formation of tin vacancies (V_{Sn}) and V_{Sn}–H complexes, resulting in increased concentration of holes. In addition, the SnO_x films deposition in H containing atmosphere leads to oxygen vacancy (V_O) termination by H. This substitution results in formation of Sn–H^+ bonds, which leads to slight increase in Hall mobility of holes after annealing because of reduction of carrier traps. Thus, the H doping can be used as one of the ways to improve the characteristics of p-type TFT.

Chapter 3 represents research results of the H adding effect on the n-type IGZO film properties, and mechanism causing the activation temperature reduction is presented.

Synthesis of IGZO films is always accompanied by the formation of various defects. These defects affect not only the film properties, but also the TFT performance. Therefore, they should be properly mitigated during post-processing in order to achieve quality films and high performance devices. The most common treatment method for IGZO is post-deposition annealing at 300 °C. However, this temperature is not suitable for flexible or wearable electronics applications, whose processing temperature is limited due to polymer substrate utilization. This limitation requires the development of new approaches which will allow to achieve the comparable electrical properties at relatively low-temperature. Low-temperature activation process is a key approach

for OS materials utilization in flexible and wearable electronics. We reported that H adding during the IGZO deposition reduces the activation temperature to 150 °C, demonstrating a strong potential of this method. However, the mechanism upon H adding causing low-temperature activation has not been clarified in detail.

In this chapter, we focused on the mechanism of the H adding during the IGZO films synthesis resulting in the carrier density control and defects passivation after low-temperature activation. Thus, it was found the higher the H content the greater the O diffusion and the larger the shift of the diffusion starting temperature toward a lower temperature. Diffusion starting temperature shifted from 190 °C to 90 °C toward higher H content due to the induced structural change facilitating the O diffusion. HAXPES analysis revealed the near Fermi level defect reduction for H doped IGZO films after the 150 °C annealing. These results demonstrate that H introduction into the IGZO films holds promise for low-temperature applications, such as flexible electronics.

Chapter 4. In this chapter the properties of hydrogenated polycrystalline (poly) n-type In-Ga-O films are discussed. The results of thin film analysis and the effects on TFT characteristics both during IGO channel formation and during device fabrication are presented.

According to recent reports, active research in further increasing the mobility of the OS TFTs is focused on the use of materials with high-In content (In-rich). Thus, the mobility of monocrystalline In_2O_3 has been reported to be 160 cm^2/Vs, which makes polycrystalline InO_x a potential candidate material for high-mobility TFT application. However, such materials tend to be polycrystalline due to their ease of crystallization at low temperature, as well as spontaneous crystallization even during room temperature deposition. In addition, the electron concentration in In-rich OS is high, about 10^{20} cm^{-3}, which requires the development of methods to reduce the electron concentration for application in TFTs.

It was reported that the transparent conductive oxide (TCO) of polycrystalline InO_x can be formed by solid-phase crystallization at 200 °C by a sputtering process in the H_2O vapour contained in the Ar and O_2 atmosphere. In this study we investigated the H doping effects on electrical

and structural properties of the IGO film. It was found that intensive H doping suppressed the crystallization during the film deposition. Hydrogen incorporation into the IGO film reduced the electron concentration by two orders of magnitude from 10^{20} cm^{-3} to below 10^{18} cm^{-3} through crystallization process. On the other hand, the unintentional H doping can also occur in subsequent TFT fabrication steps. Therefore, the formation of a passivation layer is necessary to protect the channel and ensure TFT reliability. However, H can diffuse into the TFT channel, both during the passivation layer deposition and from it at a later stage. Thus, film properties and influence of H originated from the related processes are investigated. In addition, the film properties in relation to TFT performance are discussed.

Chapter 5 summarizes the content and each chapter's findings. Difficulties that need to be address are identified, and further research steps are described.

Table of content

List of Figures

List of tables

Chapter 1

Introduction

1.1. Background

The modern era of society progress is directly related to information and technology development. Vision is the most important human ability to perceive information and process it. About 60-70% of all information received in the process of a person's life comes with the help of the visual system. Communication by smartphone, personal computers usage for business, creation and consumption of entertainment content via TV, tablets and laptops, perception of information on different internet resources, news reading and many others. All these attributes of daily activity are inevitably associated with displays interaction, which have become an integral part of our lives. However, the history of display technology development began about 100 years ago, has passed several key stages and is actively continuing its development towards increasingly complex and modern applications. This is opening up new possibilities which are repeatedly shown in various science fiction works and films, additionally stimulating research and development in this area.

The main characteristics and key advantages of flat panel displays (FPDs), that they are much lighter and thinner than traditional cathode ray tubes of the last century. Many different FPDs have been successfully developed and introduced to the mass market over the past two decades. For instance, liquid crystal display (LCD), plasma display panel (PDP), electronic papers (e-papers), light-emitting diode display (LED), quantum dot (QLED) and organic light-emitting diode (OLED), the recent modern emerging FPD technology such as micro and mini-LED. Operating and switching characteristics of the LCD displays are controlled by an array of thin-film transistors (TFT) individually responsible for each pixel that forms an image. TFT is a field-effect transistor (FET) which is relatively thin and made of different materials, the key layer of which is a semiconductor material.

However, the development of next-generation displays presents new challenges. A distinctive feature of next-generation displays is the quality improvement of the displayed image. Figure 1.1 shows the image quality comparison for different display resolutions. The most widely known and used display resolution is High-definition (HD) 1080p (1920×1080), which is formed by the number of pixels in the matrix (rows and columns). With an increase in display resolution the quality, clarity and sharpness of the image increases. The next level of quality is known as Ultra-high-definition (UHD) with 4K (3840 × 2160) and 8K (7680 × 4320) resolutions. As can be seen, higher resolution increases the total number of pixels.

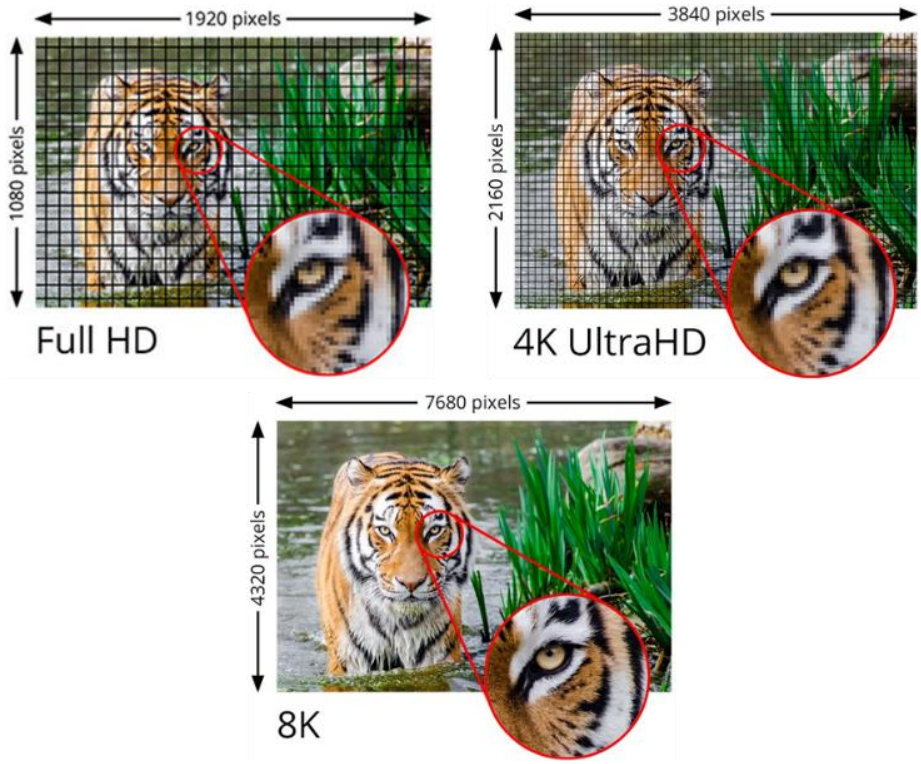

Figure 1.1 Difference between the image qualities for different display resolutions.

Higher resolution requires higher performance. In other words - fast control of individual pixels to change the image. It is necessary not only to improve the quality but also to maintain the proper refresh rate of the image, which is known as frame rate. Frame rate or frame per second (FPS) is the frequency at which consecutive images are displayed. Nowadays the minimum acceptable standard of refresh frequency is 60 Hz. Figure 1.2 demonstrates the difference between FPS and how it is perceived when viewed. Higher refresh rate produces smoother, clearer images, making them more pleasing to the eye. Thus, the FPDs performance is mostly dependent on the

TFT characteristics. It imposes additional requirements on development of the semiconductor materials for TFT. Amorphous hydrogenated silicon (a-Si:H) has been a widely used technology for production in FPD since the seventies of the last century [1].

a-Si:H possesses several major disadvantages including low mobility ~ 1 cm^2/Vs, which limits the performance of devices based on it, and the impossibility of using it in some applications due to its small band gap resulting in opacity. In contrast, the low-temperature polycrystalline silicon (LTPS) exhibits the high mobility over 100 cm^2/Vs which is suitable for high resolution display application. Nevertheless, the LTPS is a more complicated manufacturing process involving excimer laser annealing (ELA) to recrystallize the amorphous Si layer by multiplied laser irradiation [2]. This complicated technique limits LTPS application for large size displays. Moreover, it has a higher fabrication cost than a-Si:H.

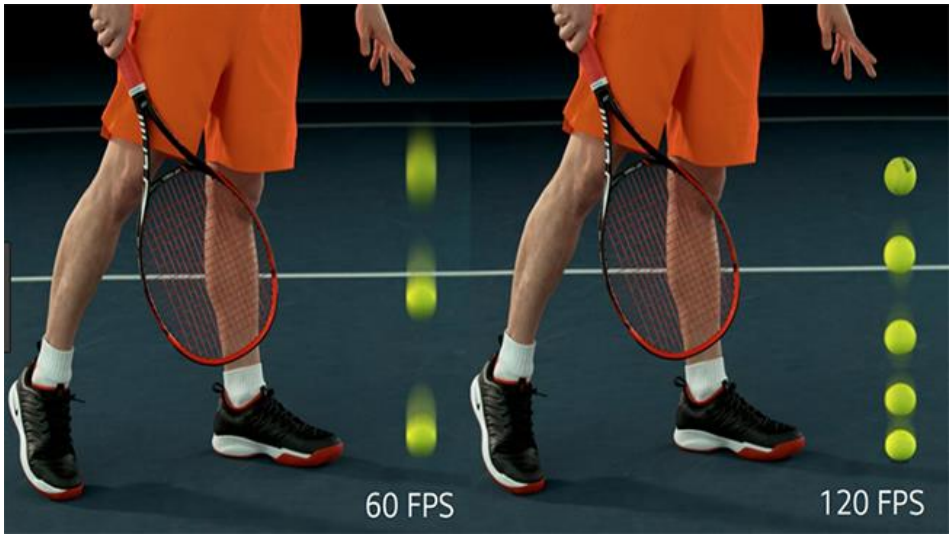

Figure 1.2 Comparative representation of the image appearance at different frame rates.

Therefore, the development of new materials is an important approach for new applications. Matsueda et al. presented the required performance of TFTs for next-generation FPDs in 2010 [3]. Figure 1.3 shows a relationship between required mobility of TFT and number of pixels in FPDs. To achieve super-high-definition TVs, required mobility increased to be over 10 cm^2/Vs, which is an impossible value for a-Si:H technology. Thus, oxide based TFTs having mobility of over 10 cm^2/Vs are proposed as a strong candidate for future super HD FPDs.

Table 1 summarizes the key features of OS technology during the FPD manufacturing process in comparison with traditional Si based ones. They possess the key advantages including high mobility (> 10 cm^2/Vs) and according to recent reports can achieve comparable mobility to LTPS, high transparency, suitability for low temperature process making it possible to use for flexible and transparent electronics, industrial friendly scalability due to high uniformity and large area deposition at room temperature, wide range of materials for various applications [4–6].

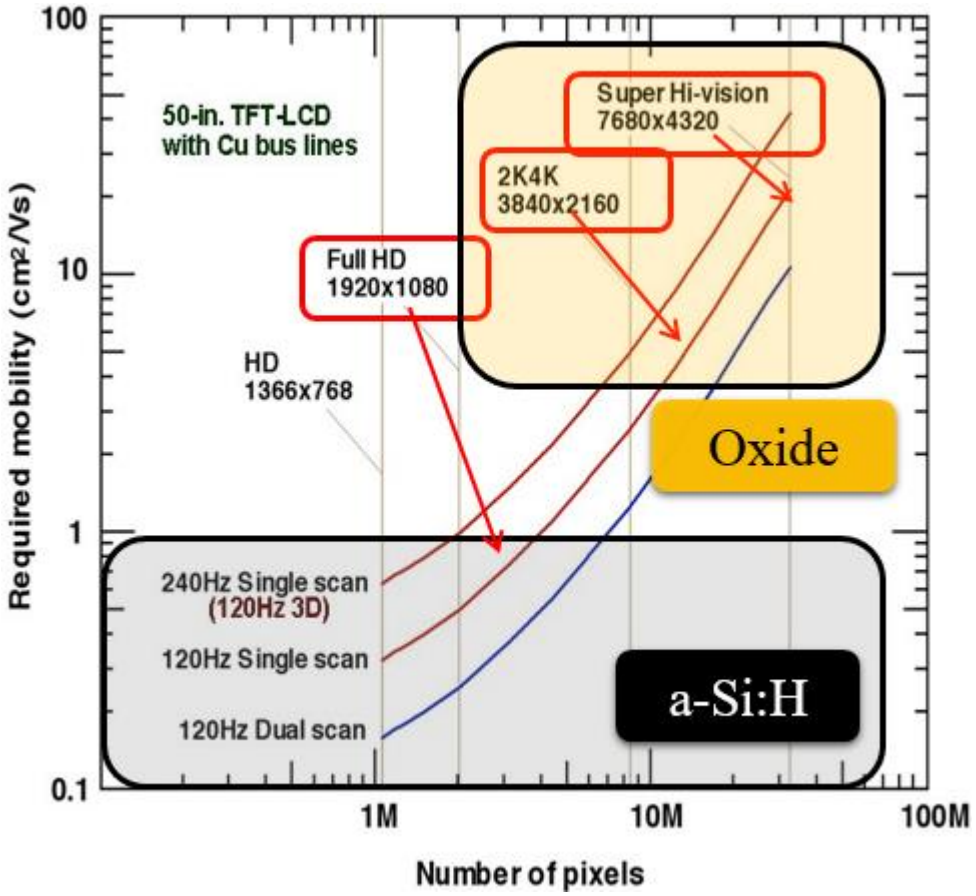

Figure 1.3 Graphical summary of required carrier mobility for next-generation displays [3].

Table 1.1 Distinctive features of different technologies for the manufacturing of FPD.

	a-Si:H	LTPS	OS
Formation method	PECVD	PECVD + ELA	Sputtering
Process temperature (°C)	150 – 350	~ 250	RT – 300
Band gap (eV)		1.1	2.0 – 3.2
mobility (cm^2/Vs)	~ 1	~ 100	10 ~ 100
structure	amorphous	polycrystalline	amorphous / polycrystalline

1.2. Historical overview of oxide semiconductors

The first oxide semiconductor based TFT was reported in 1964 by Klasens and Koelmans [7]. As a main active semiconductor layer the evaporated SnO_2 layer on anodized Al_2O_3 gate insulator was utilized. Four years later in 1968, Boesen and Jacobs demonstrated the first ZnO based TFT, suggesting the possibility of the ideal performance with more sophisticated processing [8]. On the other hand, in the next few years, several key works were published describing the mechanism of electron transport and substitutional doping in amorphous silicon [9,10]. As a result, the a-Si based FET fabricated by plasma-enhanced chemical vapor deposition (PECVD), which could be easily carried out on commercial, large-area and at low-temperature process, was demonstrated in 1979. This showed promising opportunities for use in display technology [11]. It led to the subsequent successful development and start of mass production by various companies in the early eighties. Thus, it shifted focus and research interest from oxide semiconductors for several decades. Only two decades later, new attempts were made to return to the possibility of using an OS for TFT. In 1996, the results of the successful operation and switching characteristics of the field-effect transistor were published. Antimony-doped transparent SnO_2 with n-type conductivity was utilized as the main semiconductor layer [12].

The revival period of oxide semiconductors can be considered 2003. Several research groups, almost simultaneously with a difference of several months, have reported the successful use of ZnO as the active semiconductor channel layer for TFT. Masuda et al. deposited ZnO layer by pulsed laser deposition (PLD) technique at 450 °C, demonstrating the possibility to fabricate the TFT on glass substrate. The obtained ZnO film showed relatively low carrier concentration (N_e) 5×10^{16} cm^{-3} with high transparency about 80% in visible range. While the TFT has demonstrated comparable performance to a-Si:H with field-effect mobility (μ_{FE}) and threshold voltage (V_{th}) of 0.7 cm^2/Vs and - 1.0 V, respectively [13]. Hoffman et. al formed the ZnO channel via ion beam sputtering at room temperature (RT) followed by rapid thermal annealing in O_2 atmosphere at 600 – 800 °C. The electrical characterization results of the TFT device showed the

μ_{FE} in range 0.3 – 2.5 cm^2/Vs with V_{th} from 10 V to 20 V. These results suggested the attractive application for transparent TFTs in active-matrix LCD [14]. Carcia et. al investigated the ZnO deposition condition with good electrical properties at RT. Fabricated ZnO TFT showed μ_{FE} of 2 cm^2/Vs and V_{th} of 0 V. Those results demonstrated the potential of using OS for low-temperature application such as flexible electronics [15]. Over the next several years of research, improvements were demonstrated in ZnO based TFT with a mobility over 10 cm^2/Vs, as well as theoretical modelling and simulation of their properties, thereby introducing and complementing the promising field of OS application [16–18]. In 2006, the high-performance top-gate ZnO TFT for AM-LCDs was developed. The ZnO TFT had μ_{FE} and V_{th} of 50.3 cm^2/Vs and 1.1 V, respectively. Moreover, the first 1.46”diagonal AM-LCD panel driven by the ZnO-TFTs was demonstrated [19,20]. In addition, the 2.15” AM-OLED panel driven by ZnO-TFT array was fabricated. ZnO based TFT was fabricated by atomic-layer deposition (ALD) at 100 °C demonstrating the possibility of OS utilization for transparent electronics [21]. These achievements finally demonstrated the promise of the application and use of oxide semiconductors as an alternative to a-Si:H.

Nevertheless, despite impressive and promising results, the synthesis of ZnO also showed certain issues. It is known that ZnO is a polycrystalline material, which affects the uniformity and repeatability of the characteristics of TFT. This is especially critical during the large displays manufacturing. Device simulation results assumed that the ZnO TFTs are strongly dependent on the polycrystalline nature of ZnO due to grain boundary effect [17]. For instance, the mobility strongly depends on the quality and properties of film. Synthesis parameters and methods have a direct impact on film morphology such as roughness and grain size [22–24]. With these limitations and disadvantages of polycrystalline materials, at almost the same time (2003-2004) a different idea of OS was proposed and demonstrated. Materials based on this idea demonstrated the mobility about 10 cm^2/Vs, but still retained an amorphous state. These materials were later successfully commercialized by Sharp in 2012. This is how the research and development was divided into two areas: polycrystalline and amorphous materials for TFTs.

1.3. Amorphous oxide semiconductors

1.3.1. Electronic structure and unique feature of AOS

Simultaneously with intensive progress and development in the field of binary oxides (ZnO, In_2O_3, SnO_2), another research was carried out on the part of complex oxides. Hosono et. al proposed the working hypothesis of novel transparent amorphous oxide semiconductors (AOS) with wide band gap in 1996. An electronic configuration according to equation 1.1 for heavy metal cations (HMC) was proposed as a new material design concept.

$$M\colon (n-1)d^{10}ns^{0}\ (n \geq 5), \tag{1.1}$$

where, M – heavy post transition metal cation, n - principal quantum number, describes the electron's state. The high electron mobility in such AOS is achieved by large overlap of *ns* orbitals of HMC forming the bottom of the conduction band minimum (CBM). In addition, due to the symmetry of these orbitals and the large spatial overlap it makes them insensitivity in the amorphous state, while ensuring successful electron transport. In contrast, the top of the valence band maximum (VBM) consists mainly of low-energy oxygen *2p* orbitals, providing a wide band gap [25]. As a result of this idea the three new amorphous materials, including a-$AgSbO_3$, a-Cd_2GeO_4 and a-Cd_2PbO_4, with Hall mobility about 10 cm^2/Vs were demonstrated. Later on, the same research group demonstrated a first top-gate flexible TFT based on amorphous In-Ga-Zn-O (a-IGZO) semiconductor. This material was based on the same concept [26]. The saturation mobility of the IGZO based TFT was in range of 6–9 cm^2/Vs being one order larger compared to a-Si:H. After a series of promising publications on the possibilities of AOS for application in FPD, the direction of development of OS was divided into two directions: polycrystalline and amorphous. Authors have shown and explained the electron transport and advantage over conventional covalent semiconductors. Figure 1.4 demonstrates the electron transport in crystalline IGZO (c-IGZO) and a-IGZO in comparison with crystalline Si (c-Si) and a-Si.

It can be seen that the carrier transport in Si is formed by sp^3 hybrid orbitals with a pronounced spatial orientation due to the 109°50′ angle between them. This chemical bonding feature in covalent semiconductors limits the transport resulting in low mobility in a-Si:H about 1 cm^2/Vs,

while this value contrast to monocrystalline Si with electron mobility about 1000 cm^2/Vs [27,28]. In addition, the level of forming defects such as point defects (dangling bonds and atom floating bonds), and also strain defects (large angle deviations in the bond angles), due to distorted amorphous structure is higher resulting in formation of deep localized states leading to carrier traps and transport control by hopping [26,29–31]. On the contrary, because of the spherical symmetry of the metal 5s orbitals and their large overlap the electronic transport is not strongly affected by any distortion even in the amorphous state. This allows the sufficiently high mobility > 10 cm^2/Vs in amorphous oxide semiconductors exceeding the values of a-Si:H. It should also be noted that the mobility in the a-IGZO is also lower compared to the c-IGZO, which is also due to the presence of a large number of different defects. However, in order to achieve the single-crystalline films of such complex structure oxides, a high temperature about 1400 °C is required. Thus, the c-IGZO based TFT with the μ_{FE} of 80 cm^2/Vs was demonstrated in 2003 [32].

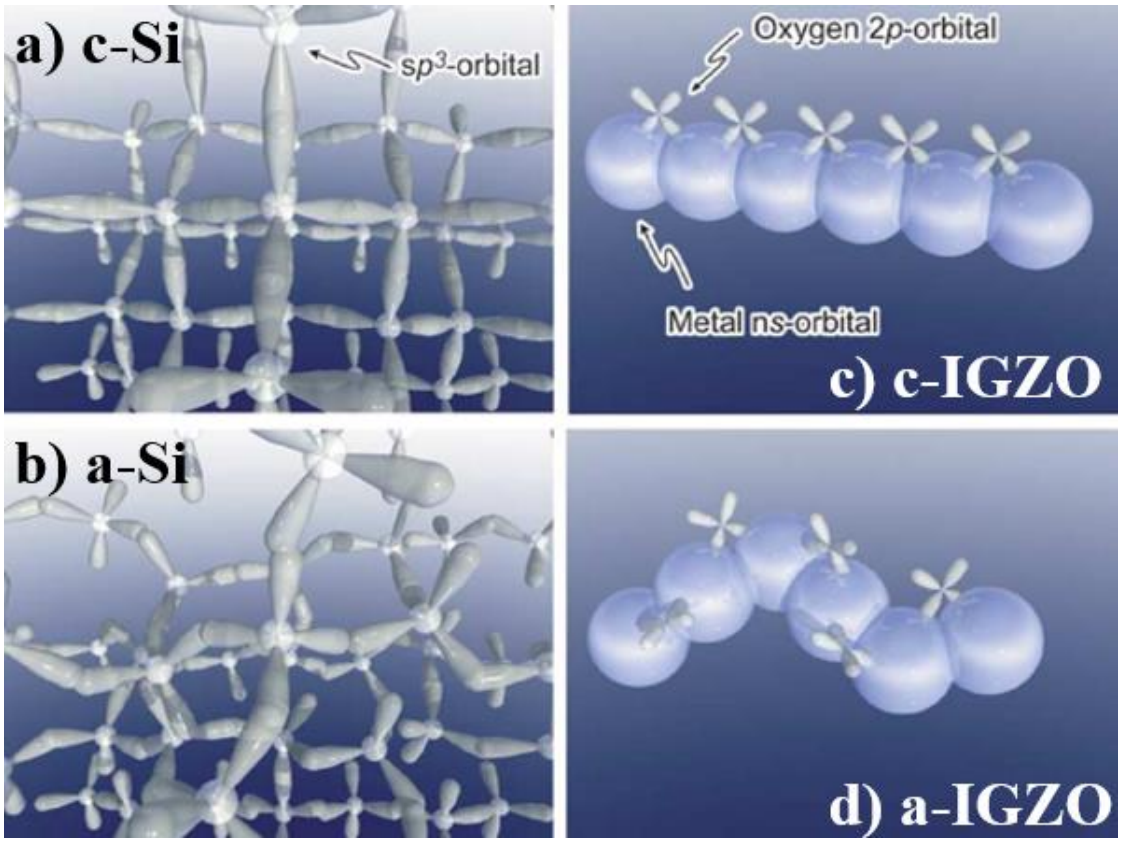

Figure 1.4 Schematic illustration of the carrier transport paths in covalent semiconductor and oxide semiconductors: (a) c-Si; (b) a-Si; (c) c-IGZO; (d) a-IGZO [26].

1.3.2. Electronic transport and origin of high mobility

Subsequently, electronic transport in a-IGZO and c-IGZO films has been studied in detail. Figure 1.5a shows the dependence of mobility as a function of electron concentration (N_e) in the different quality IGZO films and with different crystal structure. Temperature dependence of Hall effect measurement of a-IGZO demonstrated that the electron mobility increased from 3 to 13 cm^2/Vs when the N_e increased by four orders of magnitude from 6×10^{15} to 10^{19} cm^{-3} [33]. Interestingly, those values are comparable to the values obtained for c-IGZO mobility of which showed a similar tendency toward mobility increase from 1 cm^2/Vs to > 10 cm^2/Vs when N_e was increased to 4×10^{18} cm^{-3} [34]. However, this dependence in crystalline semiconductors is known to have the opposite tendency in which carrier scattering with dopant ions controls the mobility [27,35]. Thus, the observed temperature dependence in AOS of the Hall effect mobility was explained by the formation of potential barriers with an average barrier height of 40-120 meV with an energy distribution width of 20-30 meV near the conduction band edge [36]. Therefore, the conduction model in a-IGZO and c-IGZO was explained by the predominant percolation conduction model, which fit well with the description of the different results from the standard Arrhenius temperature plot [33,34,36,37].

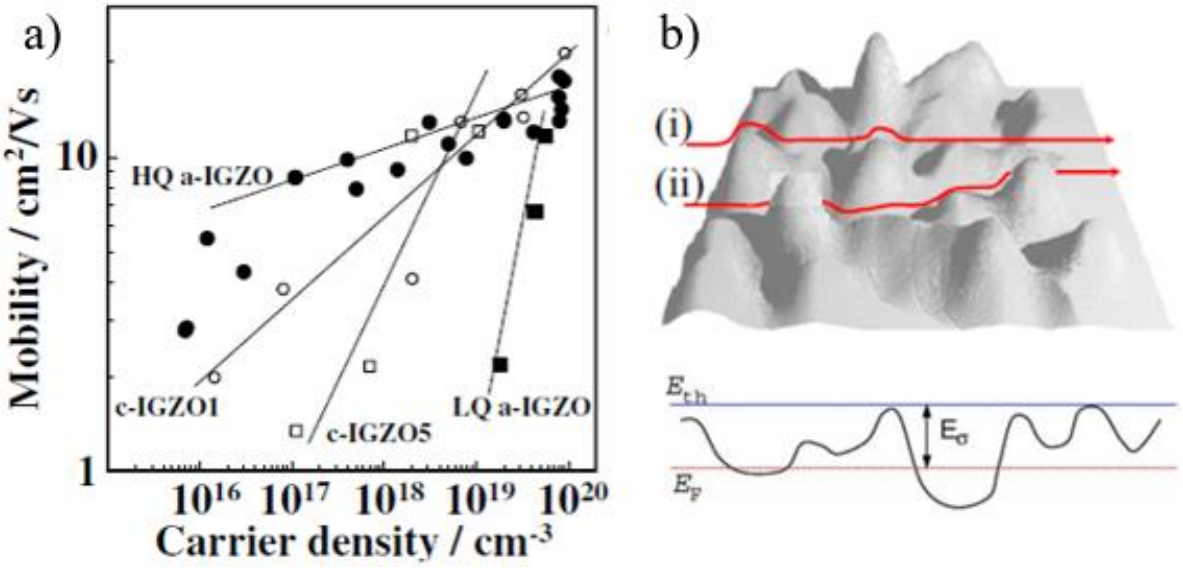

Figure 1.5 (a) Mobility as a function of electron concentration of IGZO films [33]; (b) potential barrier heights distribution near the CB and schematic illustration of electron path [34].

1.3.3. Defects in AOS

Despite the above-mentioned advantages of OS, including the ability to form them at room temperature, the synthesis of OS is always accompanied by the formation of various types of structural and electronic defects. The defects formation is caused both by (i) the process parameters such as base pressure, oxygen content during the synthesis since O plays an important role in OS, deposition pressure, power etc.; (ii) synthesis method itself. The most widely used technique is magnetron sputtering in vacuum containing high energy plasma species such as O ions and reflected Ar ions, after interacting with the target material. These defects affect not only the film properties, but also the TFT performance. Therefore they should be properly mitigated during the post-processing in order to achieve high quality films and as a result high performance devices. It was shown that subsequent temperature treatment at about 300 °C is necessary to improve the performance of the TFT [38]. This is because of the need to reduce the various in-gap defects which exist after the film formation. However, the amorphous nature of oxides imposes certain difficulties on the analysis of defects in such structures. Thus, fundamental material science of the AOS based on calculations from the first principle, such as density functional theory (DFT) in combination with direct defects analysis by Hard X-ray Photoemission Spectroscopy (HAXPES), have made it possible to construct with high confidence a model of defects in the band gap, clarifying their origin, location and their influence.

Figure 1.6 shows a schematic diagram of the electronic structure of a-IGZO which was proposed by Kamiya et al. in 2009 [39]. Thus, the HAXPES analysis revealed the tail-like states within 1.5 eV from VBM with estimated subgap density of states (DOS) about 10^{20} cm^{-3} [40–42]. Intensive research has been done regarding to the nature and affiliation of these defects near the VBM. Thus, the formation of these defects can be attributed to several causes including oxygen deficiency well known as oxygen vacancy (V_O), weakly-bonded O or undercoordinated O with insufficient coordination number (O_{uc}), hydrogen related defects such as hydroxyl groups (*O-H*) and metal-hydrogen bonds (*M-H*) [39,43–46]. Nevertheless, high-density states exist near the VBM, they can be disregarded for applications in TFT with n-type conductivity, because these

states are inactive and do not have any contribution to carrier transport.

The main defects in OS are V_O due to their relatively low formation energy. Controlling the formation or elimination of these defects determines the electrical and structural properties of the films. Figure 1.7 demonstrates the conductivity and N_e of the a-IGZO films deposited at different O ration ($R[O_2]$) in relation with TFT transfer characteristics [47]. It can be seen that the higher the $R[O_2]$ the lower N_e. These results indicate that the N_e depends on the amount of generated V_O in the film, because low $R[O_2]$ generates O deficiency. In contrast, high $R[O_2]$ can reduce the V_O resulting in decrease N_e, but TFT is not at on-state due to the formation of high-density subgap states. These states are formed because of weakly-bonded O (O_{uc}) or neutral O (O^0) atoms formed in excess conditions, which can capture electrons [47]. The origin and formation of these defects (i.e O_{uc} or O^0 or O_{in}) was observed by TDS analysis for IGZO films annealed in O_3 atmosphere [44]. The trapping way was explained by the following reaction [46]

$$O^0 + \mathrm{n}e^- \Rightarrow O^{n-} \ (\mathrm{n} = 1 \text{ or } 2), \tag{1.2}$$

Subgap defects, which are located especially near the CBM, directly affect the electron transport. It is also known that oxygen deficiency in a-IGZO is classified by two different groups, which are both the reason of subgap states origin. One of them belongs to the states which can be found near CBM. These states are formed due to the non-bonding state of metal cation, since the CBM is formed by the overlapped *ns* orbitals. It was reported the presence of donor level located inside the band gap within 0.1 – 0.15 eV from CBM [39]. On the other hand, more deeper states were found located at 0.13 eV and 0.2 eV, denoted as shallow and deeper, respectively [48]. In addition, it was shown by thermal desorption spectroscopy (TDS) analysis that hydrogen can passivate even deeper states located about 0.3 eV from CBM [47–49]. All of these states existing near CBM can be considered as electron traps deteriorating the TFT performance.

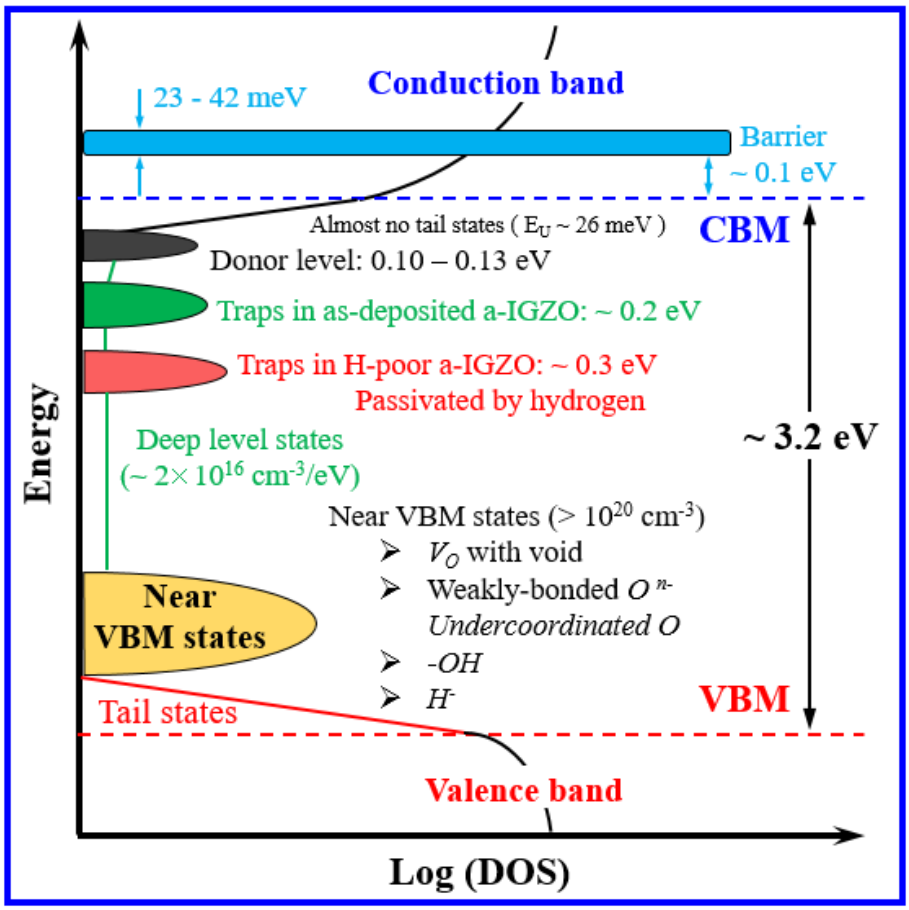

Figure 1.6 Schematic representation of the AOS electronic structure obtained from theoretical studies such as first principle calculation and experimental studies by various technique including HAXPES, TDS and others [46].

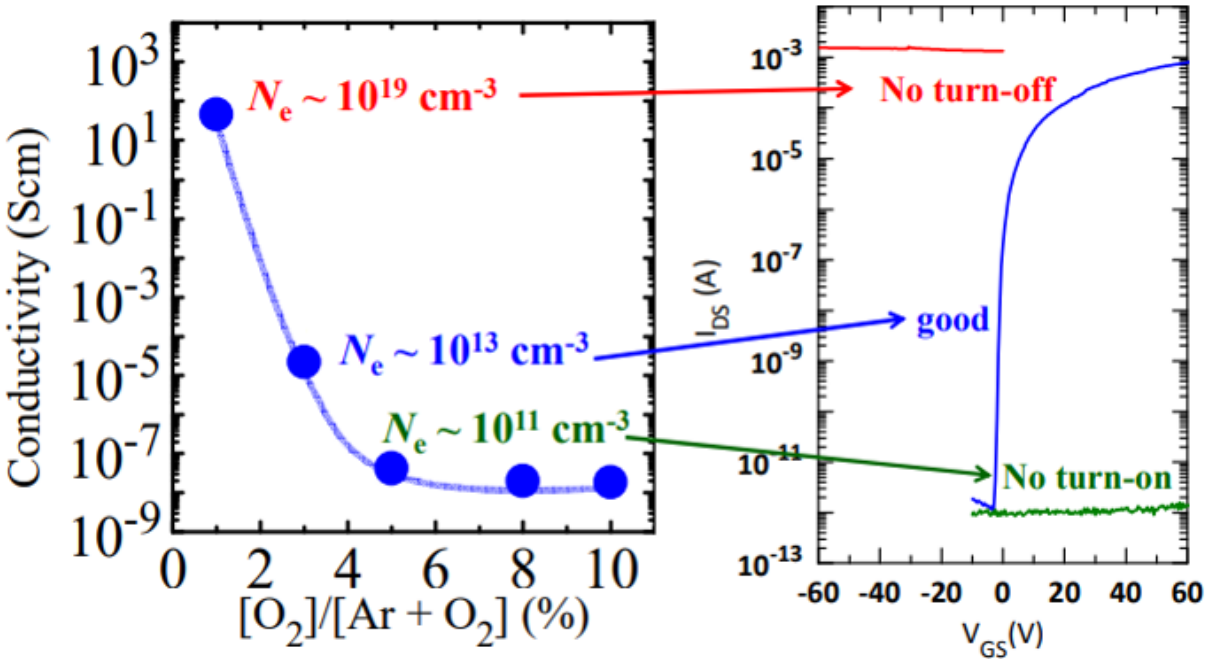

Figure 1.7 a-IGZO film electrical conductivity as a function of O ratio during the film synthesis with relationship to carrier density and TFT operation transfer characteristics [47].

1.4. Role of Hydrogen in oxide semiconductors and device performance

Hydrogen is one of the most common types of the impurity and can be found in all deposition apparatus in a form of residual H_2O or H_2 molecules, which affect the base pressure in any high vacuum deposition chamber. On the other hand, H itself is also an integral part of the technological process. For instance, as was discussed before the a-Si:H can be fabricated by PECVD process using a silane gas (SiH_4) precursor. This synthesis method was first reported by Chittick et al. in 1969, which demonstrated an increase in the effect of photoconductivity [50]. Paul and Anderson from Harvard University verified in detail the role of H in reducing defects in a-Si:H in 1981 [50]. The structural defects in a-Si such as dangling bonds result in the origin of high-density of subgap states. However, H can effectively passivate these dangling bonds by forming Si-H bonds improving device characteristic [50–56]. Figure 1.8 depicts the role of H in passivation of the dangling bonds in a-Si:H.

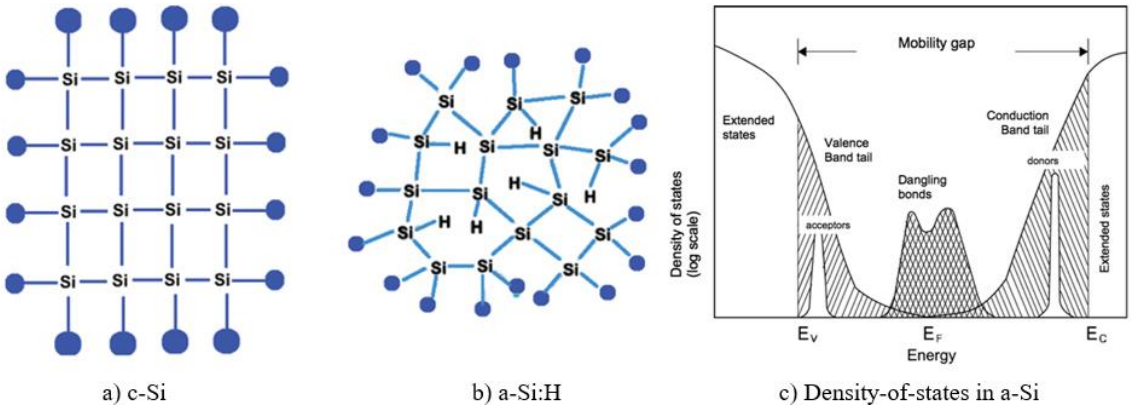

Figure 1.8 Schematic representation for the structures of (a) c-Si; (b) a-Si:H; (c) density-of-states in subgap of a-Si [57].

The first works related to the explanation of the role of H in oxide semiconductors date back to the early fifties. Solubility and diffusion of the H in ZnO single crystals were studied. In addition, it was found that growing ZnO single crystals with the introduction of H from the H_2 atmosphere allows an increase in the n-type conductivity. Thus, it demonstrated that H acts as a shallow donor type of impurity with ionization energy about 0.05 eV, affecting the electrical properties of ZnO [58–60]. Due to the fact that OS got a second boost in development in the 2000s. The mechanism and role of H based on the first principles calculation have also been studied and

clarified in detail in recent works. Van de Walle suggested that the prevailing n-type conductivity cannot be attributed to intrinsic defects, such as oxygen vacancies (V_O), because their formation energy is low and behaves as deep donors instead of the shallow ones, behaviour of which was observed before [61]. Therefore, the formation energy of several possible H configurations was analyzed. It was shown that H^+ has the lowest formation energy and is the dominant H state, resulting in the formation of hydroxyl groups (*O-H*) in ZnO. Moreover, these results showed a different role and mechanism of H, which differs from defect passivation such as dangling bonds, as described above for a-Si:H. Thus, the theoretical evidence for H behaviour as a shallow donor in ZnO was presented [61].

On the other hand, it was shown that not all H related bonds are thermally stable, which is an important factor during the processing. Thus, ZnO annealing in the H_2 gas atmosphere at 700 °C resulted in increased free carrier concentration. However, post-annealing at a relatively low temperature of 150 °C reduced the free carriers by 80% due to terminations of O-H bonds, which were originally introduced [62,63]. Interstitial H (H_i) forms bonds with lattice oxygen displacing the Zn from its original position away from the O-H group. This H_i can be easily removed by thermal annealing due to its high mobility (hopping) between neighbouring O atoms even at room temperature. In contrast, the substitutional H (H_O) at an O site is more stable at relatively high temperature up to 500 °C, since the lattice related vacancies and impurities can trap the H, also reducing the H_i concentration [62–65].

After the successful demonstration of IGZO application for TFTs, research on the role of H in amorphous oxide semiconductors also intensified. It was reported that H shows similar behaviour as in the ZnO and acts as a shallow donor. Annealing of the IGZO films in dry H_2/N_2 atmosphere, local H based plasma treatment of the IGZO film, H incorporation into the IGZO film during the SiN_x:H protection layer deposition by PECVD in H containing atmosphere resulted in increased free carrier density [39,66–68]. This similar H behaviour was also confirmed by first-principles calculations. Kamiya et al. reported that H-doped a-IGZO calculated for different models of H atom coordination resulted in regular O-H bonds formation [39,69]. Figure 1.9 depicts

the illustration of O-H bonds formation in a-IGZO. Authors concluded that the H doping results in electron doping through the following reaction:

$$H^{0}_{(from\ outside)} + O^{2-}_{(in\ a-IGZO)} \Rightarrow -OH^{-}_{(in\ a-IGZO)} + e^{-}\ , \qquad (1.3)$$

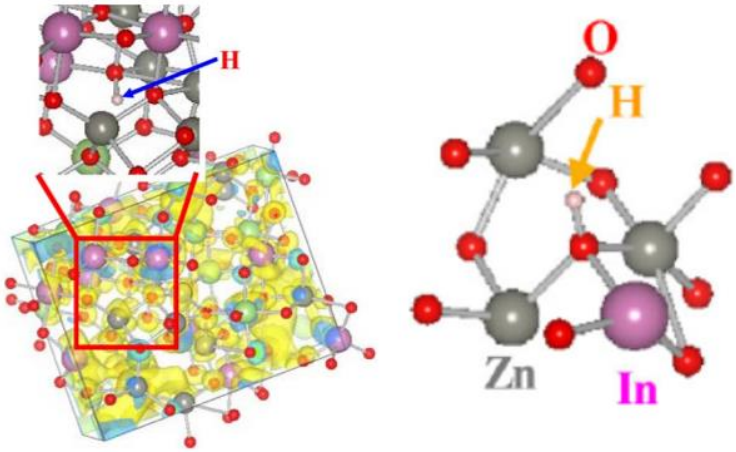

Figure 1.9 Structure around a doped H atom obtained through first-principle calculation for CBM wave function for H-doped a-IGZO [39,69].

In contrast, the H content in the a-IGZO films is varied for different sputtering tools within the same deposition parameters. Thus, it was shown that the H concentration in the a-IGZO film is about 10^{20} cm^{-3} after the deposition by standard vacuum sputtering equipment with base pressure 10^{-4} – 10^{-5} Pa. While the H concentration decreased by one order of magnitude to 10^{19} cm^{-3} for the a-IGZO film deposited by sputtering in a high-vacuum chamber with a base pressure of 10^{-7} Pa using a liquid nitrogen trap and a titanium getter pump, which reduced residual H_2O and H molecules in the atmosphere [70]. These results demonstrated the favourable effect of H such as defects passivation improving the TFT performance. According to several reports H incorporation into the film is not only limited by the IGZO synthesis condition and should be considered within the TFT fabrication process. It was shown that H can diffuse from the passivation layer, such as SiO_x etch-stopper to the IGZO channel, and that this diffusion leads to an improvement in TFT transfer characteristic [71]. Nomura et al. evaluated the H diffusion into the non-hydrogenated a-IGZO films. It was reported that H can diffuse up to 200 nm depth even at relatively low annealing temperature [72]. Thus, these results relate to the effective role of defects passivation by H improving the TFT performance.

As was explained in previous section, the a-IGZO film contains high density subgap states, such as V_O , which is required subsequent post-annealing at about 300 °C. Thus, it was reported that dry O_2 annealing at 200 – 300 °C is the most effective to improve TFT characteristics. This specific temperature range is explained by the fact that processing at higher temperatures up to 500 °C leads to complete removal of H_2O from the IGZO films due to desorption. So it was found that it leads to the formation of new trap states that degrade the TFT performance. These deeper states were attributed to H depletion (de-passivation) which can effectively passivate these defects. In addition, these states are located near the CBM within 0.3 eV which directly affect carrier transport in n-type devices [73,74]. Additionally, it has been shown that there is a correlation between the increased desorption of H_2O-related molecules when heated in the temperature range of 180 – 300 °C and the increased conductivity of the IGZO film. Nomura et. al explained such conductivity change by the following reaction:

$$M - \mathrm{OH} + M - \mathrm{OH} \rightarrow V_O^{\cdot\cdot} + M - \mathrm{O} - M + H_2\mathrm{O} \uparrow + 2e^-, \qquad (1.3)$$

where M is meal cation, $V_O^{\cdot\cdot}$ is ionized oxygen vacancy, speculating that the free electron generation is related to oxygen deficiency [75].

As seen above, the vast majority of the results indicate the H role in a-IGZO and its preferential formation of O-H bonds. In this case, H acts as a cation with a valence state +1 (H^+). However, H can act as an anion and exhibit a different valence state -1 (H^-), whose behaviour is important in terms of understanding the defect passivation effect. Körner proposed an improved model to density functional theory to investigate the origin of subgap states in a-IGZO. It was shown that the upper half of the subgap states are caused by V_O originated from the In-Zn pair defect (*M-M* bonds), which are located near the CB edge [43]. However, the hydrogen adding into the model revealed that H can form metal-hydrogen bonds (*M-H*), resulting in moving deep in subgap these defects, and away from the CB edge but remaining and increasing near VB states [43]. Thus, the first theoretical understanding and explanation of the effect of defect passivation by H was obtained. The experimental evidence of H^- presence in the a-IGZO was reported by Bang et al. in 2017. Infrared absorption spectroscopy revealed the two absorption bands at 1389

and 1523 cm^{-1} which were attributed to *M-H* bonds. The combination of experimental and DFT calculations results demonstrated the subgap states formation from the *M-H* bonds in a-IGZO, showing the clear evidence in presence of the H^-, and that as-deposited a-IGZO contains high concentration of *M-H* and *O-H* bonds [45]. These *M-H* bonds are formed by H^- stabilization at V_O site by substitution during the synthesis of the IGZO films. Post-annealing temperature dependence showed that this substituted and formed *M-H* bonds are thermally stable even up to 800 °C [45]. Thus, the effect of defect passivation by H anion near the CBM, which has a direct effect on carrier transport, was explained. Finally, these results agreed with Körner's earlier theoretical calculations that *M-H* bonds result in increased near VBM states, and the schematic diagram of the subgap states with *M-H* position around 0.4 eV above the VBM was proposed, as shown in Figure 1.10 [45]. Our research group has recently reported the experimental evidence of the promising IGZO deposition method in the H_2 containing atmosphere ($Ar+O_2+H_2$) by DC magnetron sputtering. The electron-take off dependence performed by HAXPES revealed the V_O reduction in both bulk and near-surface regions for H doped a-IGZO films. Thus, this IGZO synthesis method can be considered as an effective method of V_O reduction in as-deposited a-IGZO film resulting in improved device stability [76].

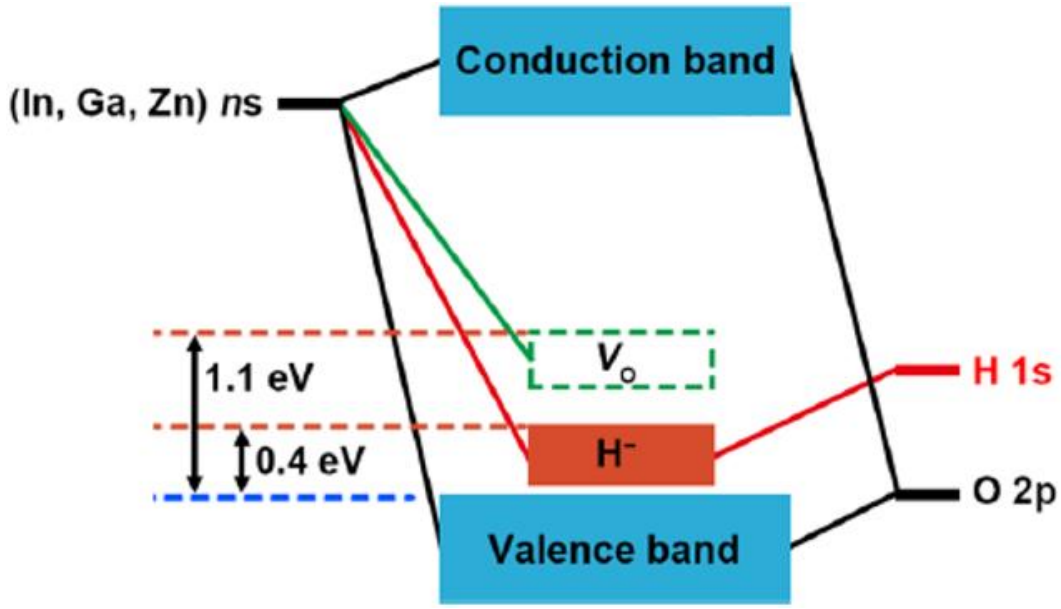

Figure 1.10 Schematic diagram of the a-IGZO subgap states calculated by DFT with respect to the H^- anion [45].

The summarized schematic of the H effects in OS are depicted in Figure 1.11, namely (a) reduction reaction via hydrogenation and O-H bonds formation; (b) defect de-passivation in H excess condition and conversion to H_2 molecular state; (c) defect passivation effect due to substitution at V_O site by H^-, and *M-H* bonds formation [77].

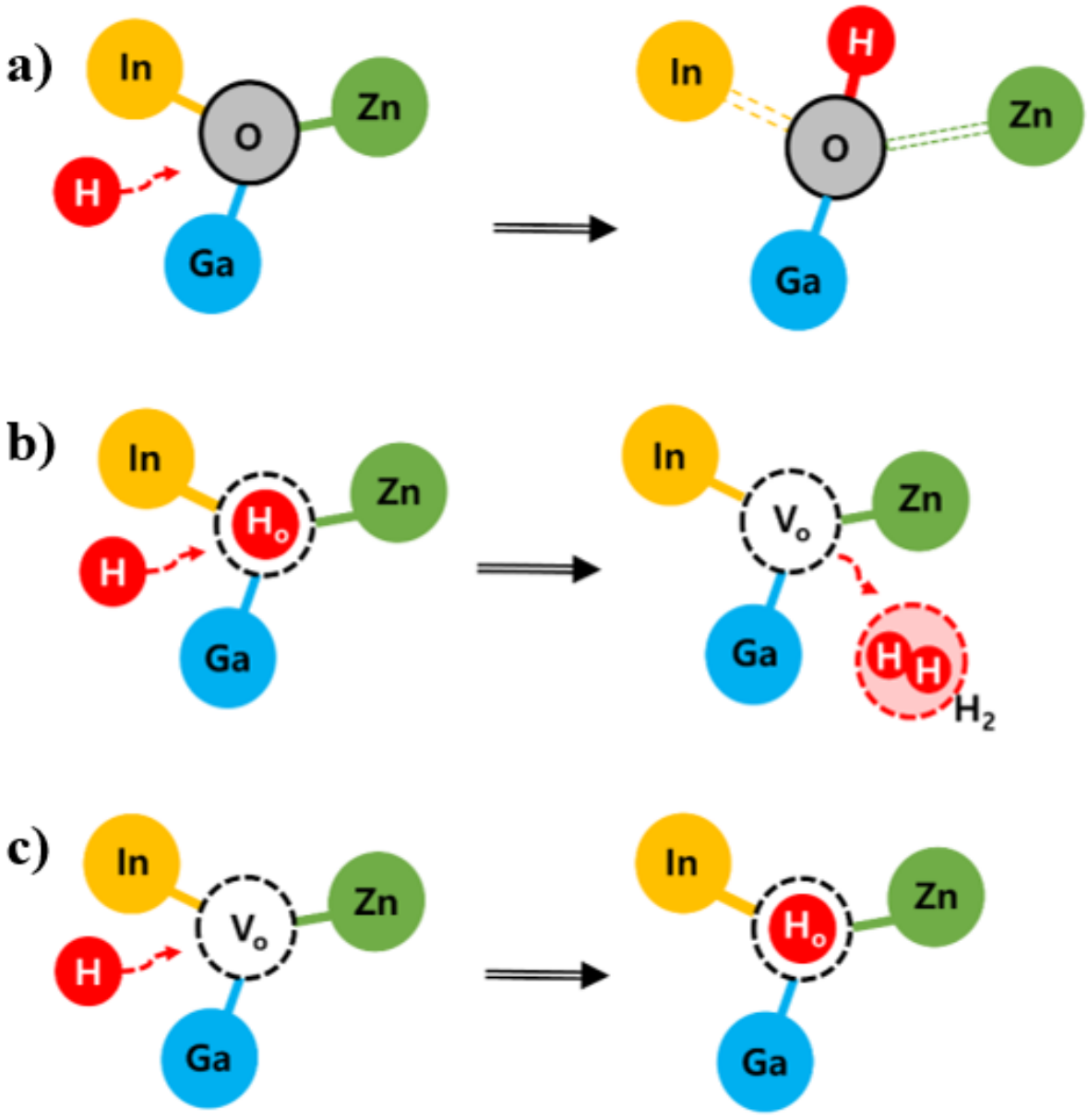

Figure 1.11. Schematic structure of the a-IGZO and the H effects. (a) *O-H* bonds formation; (b) de-passivation with molecular H_2; (c) V_O substitution by H^- with *M-H* bonds formation [77].

1.5. Thin-film transistors (TFT)

1.5.1. Device structure

TFT is a three-electrode semiconductor field effect transistor (FET) in which the current changes under the action of a perpendicular current electric field produced by the input signal. The movement of charge carriers through the channel from the source (S) to the drain (D) is controlled by a gate. TFTs are built by layering the thin films of an active semiconductor (main conductive channel layer), dielectric layer (separates the gate electrode from the active channel layer) and metallic contacts (source and drain), which are in direct contact with the channel, on a glass substrate. The positioning of these three basic elements in relation to each other determines both the performance and the manufacturing and integration process. There are two well-known device configurations: coplanar and staggered. In a staggered setup, the S and D electrodes are separated from the dielectric and located on opposite sides, whereas in a coplanar setup all S and D are on the same side of the dielectric layer. In addition, the position of the third electrode (gate) also determines the TFT configuration denoted as top-gate or bottom-gate (inverted). Figure 1.12 illustrates mentioned above four possible TFTs' configurations: (a) staggered bottom-gate; (b) coplanar bottom-gate; (c) staggered top-ate and (d) coplanar top-gate.

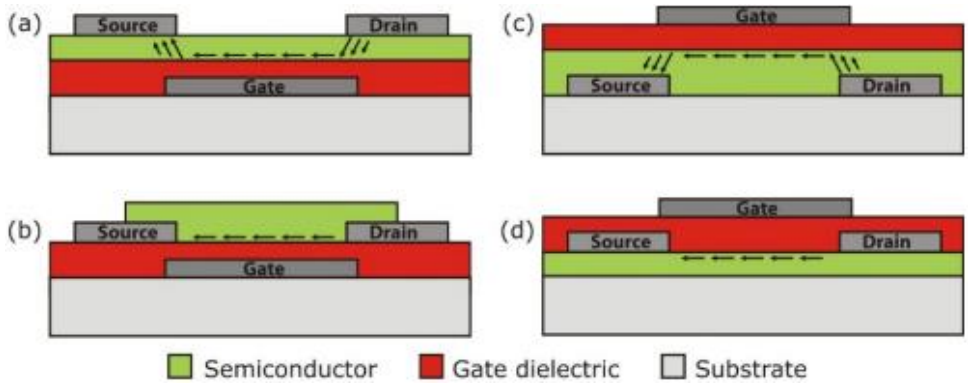

Figure 1.12 Schematic cross-view of general thin-film transistors [78].

Each configuration has its own advantages and disadvantages. For example, traditionally the simplest and fastest method of manufacturing the TFT is the staggered bottom-gate, as it involves a minimum number of technological operations. It makes this configuration the most optimal for research purposes in terms of development and testing capabilities, the use of different

semiconductor materials as a conductive channel, and the choice of material for the drain and source contacts. For example, using a commercially made silicon substrate with a 100 nm thick top layer of thermally oxidized silicon (SiO_2) allows to get a half-ready TFT, since the Si substrate can be used as a gate electrode. All that remains to be done is to form a semiconductor conductive channel and form the S and D contacts to it. The transistor is then ready for basic performance measurements. In contrast, some applications may require in the actual manufacturing process, the number of different process steps is much higher. This makes the process more complex and demanding to protect the main TFT channel from subsequent processing impact. It makes top-gate TFT configuration preferable. However, it implies the additional parameter control of the semiconductor layer due to the aggressive processes and environment such as wet and plasma etching, photolithography, chemical vapour deposition etc., in which their processing takes place. This may lead to an altered TFT performance.

1.5.2. Basic device operation

At the moment, the dominant position of OS are materials with n-type conductivity, because, as mentioned above, defect states near VBM have a direct impact on transport of holes. In addition, the number of materials with p-type conductivity is relatively small compared with n-type. Therefore, the basic principles of TFT operation with n type of conductivity will be described below. Figure 1.13 represents the structure and the energy band diagram of the n-channel TFT at different bias conditions, while Figure 1.13(b) shows the ideal situation when the work functions of the semiconductor and gate material are the same and it does not lead to additional bending on the semiconductor side. In the TFT operation the two modes of accumulation mode and depletion mode are usually considered. The accumulation mode occurs when the positive bias is applied at the gate electrode ($V_{GS} > 0$) as shown in figure 1.13(c). It leads to the voltage drop across the insulator and semiconductor causing the bands bending downward on the semiconductor side. Thus, this promotes the accumulation of electrons at the dielectric and semiconductor interface, forming a conducting channel. Then applying positive voltage on the drain electrode ($V_{DS}>0$),

electrons are injected from the source into the conductive channel and current flows through the channel between them. By changing the gate voltage (V_{GS}), it is possible to effectively control the conductivity of the TFT channel, thereby bending the semiconductor band diagram. Thus it is possible to control the current flowing in the channel (I_{DS}). When a negative voltage is applied to the gate ($V_{GS} < 0$), the curvature of the semiconductor's band structure is reversed, causing electrons to be depleted at the dielectric-semiconductor interface. Further increase in the V_{GS} leads to a further increase in the channel depletion region, extending deep into the thickness of the semiconductor. In this mode the conductive channel is not formed, I_{DS} current does not flow and TFT is in the off state.

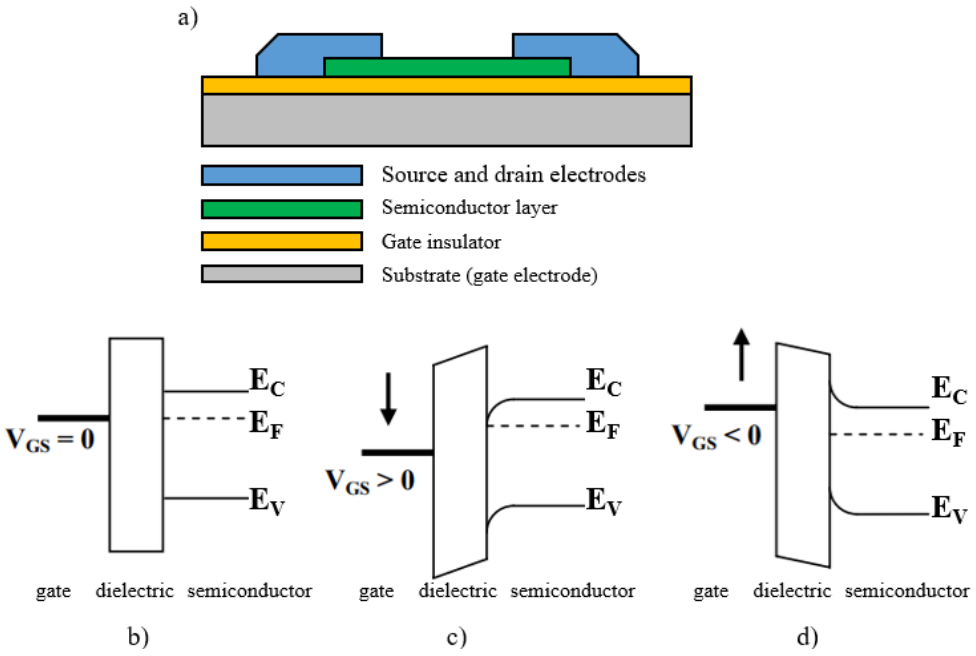

Figure 1.13: (a) Typical staggered bottom-gate n-type TFT structure; (b) energy band diagram at equilibrium; (c) positive bias; (d) negative bias.

As mentioned above, in the ideal case the work functions of the semiconductor and the S/D electrodes are equal, the energy band diagram without any V_{GS} applied is flat or known as "flat-band condition". However, in reality their work functions are varied depending on material choice resulting in initial bend. Therefore, the minimum applied gate-to-source voltage to form a conducting channel between the S and D electrodes is necessary. This voltage is defined as threshold

voltage (V_{th}). The TFT operation in the "on state" (accumulation mode) is divided into two regimes depending on the value of the applied V_{DS} at specific V_{GS}. When V_{DS} is relatively small, in this mode I_{DS} shows a linear increase with a corresponding change in V_{DS}. The magnitude of the slope is defined by the applied V_{GS}. This is called the "linear" or triode regime and TFT can be used as a resistor, the resistance of which is controlled by V_{GS}. The I_{DS} in this regime is defined by the following equation:

$$I_{DS} = \frac{W\mu_{lin}C_i}{L}\left[(V_{GS} - V_{th})V_{DS} - \frac{1}{2}V_{DS}^2\right], \quad \text{for } V_{DS} < V_{GS} - V_{th} \qquad 1.2$$

where C_i is the gate capacitance per unit area, μ_{lin} is the field-effect mobility, L and W are geometrical dimensions of the device channel length and width, respectively.

When a much higher V_{DS} is applied, the TFT begins to operate in the *"saturation"* regime, which is characterized by almost no further I_{DS} amplification regardless of the V_{DS}. This is due to the fact that with increasing V_{DS}, the channel overlap region near the drain expands and the channel resistance increases. This is also known as the pinch-off condition. In saturation regime the I_{DS} of the TFT is defined by the following equation:

$$I_{DS} = \frac{W}{2L}\mu_{sat}C_i(V_{GS} - V_{th})^2, \qquad \text{for } V_{DS} \gg V_{GS} - V_{th} \qquad 1.3$$

where μ_{sat} is the saturation mobility. Figure 1.14 depicts the output characteristics (I_{DS} in respect to V_{DS}) of the TFT with n-type conductivity.

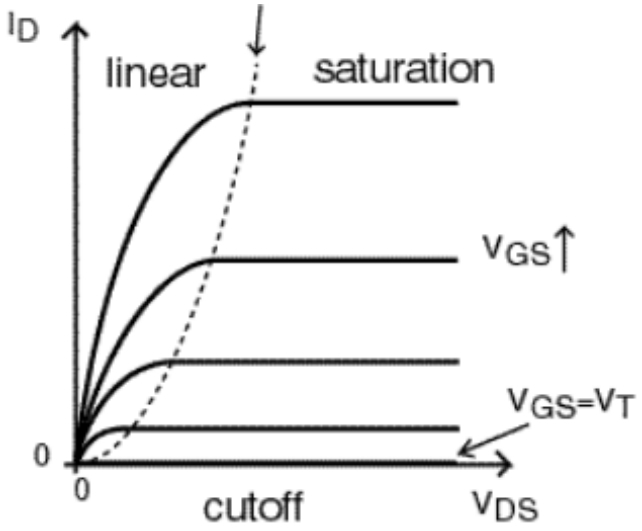

Figure 1.14 Typical output characteristics of the n-type TFT.

References

1. Kuo, Y. Thin film transistor technology-Past, present, and future. *Electrochem. Soc. Interface* **2013**, *22*, 55–61, doi:10.1149/2.F06131if.
2. Kang, M.K.; Kim, S.J.; Kim, H.J. Fabrication of high performance thin-film transistors via pressure-induced nucleation. *Sci. Rep.* **2014**, *4*, 1–6, doi:10.1038/srep06858.
3. Matsueda, Y. No Title. In Proceedings of the Required Characteristics of TFTs for Next generation Flat Panel Display Backpanels; THe Proceedings of the 6th International Thin-Film Transistor Conference, 2010; pp. 314–317.
4. Matsuo, T.; Mori, S.; Ban, A.; Imaya, A. Advantages of IGZO oxide semiconductor. *Dig. Tech. Pap. - SID Int. Symp.* **2014**, *45*, 83–86, doi:10.1002/j.2168-0159.2014.tb00023.x.
5. Kamiya, T.; Nomura, K.; Hosono, H. Present status of amorphous In-Ga-Zn-O thin-film transistors. *Sci. Technol. Adv. Mater.* **2010**, *11*, doi:10.1088/1468-6996/11/4/044305.
6. Kamiya, T.; Hosono, H. Material characteristics and applications of transparent amorphous oxide semiconductors. *NPG Asia Mater.* **2010**, *2*, 15–22, doi:10.1038/asiamat.2010.5.
7. Klasens, H.A.; Koelmans Reference, H.; Weimer, P.K. Solid-State Electronics Pergamon Press. *Radio Engrs* **1964**, *50*, 702–704.
8. Jacobs J. E., Boesen G.F., ZnO Field-Effect Transistor, Proceedings of the IEEE, **1968**, 2094–2095.
9. Le Comber, P.G.; Spear, W.E. Electronic transport in amorphous silicon films. *Phys. Rev. Lett.* **1970**, *25*, 509–511, doi:10.1103/PhysRevLett.25.509.
10. Spear, W.E.; Le Comber, P.G. Substitutional doping of amorphous silicon. *Solid State Commun.* **1993**, *88*, 1015–1018, doi:10.1016/0038-1098(93)90286-V.
11. Le Comber, P.G.; Spear, W.E.; Ghaith, A. Amorphous-silicon field-effect device and possible application. *Electron. Lett.* **1979**, *15*, 179–181, doi:10.1049/el:19790126.
12. Prins, M.W.J.; Grosse-Holz, K.O.; Müller, G.; Cillessen, J.F.M.; Giesbers, J.B.; Weening, R.P.; Wolf, R.M. A ferroelectric transparent thin-film transistor. *Appl. Phys. Lett.* **1996**, *68*, 3650–3652, doi:10.1063/1.115759.
13. Masuda, S.; Kitamura, K.; Okumura, Y.; Miyatake, S.; Tabata, H.; Kawai, T. Transparent thin film transistors using ZnO as an active channel layer and their electrical properties. *J. Appl. Phys.* **2003**, *93*, 1624–1630, doi:10.1063/1.1534627.
14. Hoffman, R.L.; Norris, B.J.; Wager, J.F. ZnO-based transparent thin-film transistors. *Appl. Phys. Lett.* **2003**, *82*, 733–735, doi:10.1063/1.1542677.
15. Carcia, P.F.; McLean, R.S.; Reilly, M.H.; Nunes, G. Transparent ZnO thin-film transistor fabricated by rf magnetron sputtering. *Appl. Phys. Lett.* **2003**, *82*, 1117–1119, doi:10.1063/1.1553997.

16. Fortunato, E.M.C.; Barquinha, P.M.C.; Pimentel, A.C.M.B.G.; Gonçalves, A.M.F.; Marques, A.J.S.; Martins, R.F.P.; Pereira, L.M.N. Wide-bandgap high-mobility ZnO thin-film transistors produced at room temperature. *Appl. Phys. Lett.* **2004**, *85*, 2541–2543, doi:10.1063/1.1790587.

17. Hossain, F.M.; Nishii, J.; Takagi, S.; Ohtomo, A.; Fukumura, T.; Fujioka, H.; Ohno, H.; Koinuma, H.; Kawasaki, M. Modeling and simulation of polycrystalline ZnO thin-film transistors. *J. Appl. Phys.* **2003**, *94*, 7768–7777, doi:10.1063/1.1628834.

18. Nishii, J.; Hossain, F.M.; Takagi, S.; Aita, T.; Saikusa, K.; Ohmaki, Y.; Ohkubo, I.; Kishimoto, S.; Ohtomo, A.; Fukumura, T.; et al. High mobility thin film transistors with transparent ZnO channels. *Japanese J. Appl. Physics, Part 2 Lett.* **2003**, *42*, 7–10, doi:10.1143/jjap.42.l347.

19. Furuta M., Characterization of sputter deposited ZnO thin film and its application to thin-film transistors, IDW '06 Proceedings of the 13th international, 2006

20. Hirao, T.; Furuta, M.; Furuta, H.; Matsuda, T.; Hiramatsu, T.; Hokari, H.; Yoshida, M. 4.1: Distinguished Paper: High Mobility Top-Gate Zinc Oxide Thin-Film Transistors (ZnO-TFTs) for Active-Matrix Liquid Crystal Displays. *SID Symp. Dig. Tech. Pap.* **2006**, *37*, 18, doi:10.1889/1.2433418.

21. Park, S.-H.K.; Hwang, C.-S.; Lee, J.-I.; Chung, S.M.; Yang, Y.S.; Do, L.-M.; Chu, H.Y. 4.3: Transparent ZnO Thin Film Transistor Array for the Application of Transparent AM-OLED Display. *SID Symp. Dig. Tech. Pap.* **2006**, *37*, 25, doi:10.1889/1.2433472.

22. Li, C.; Furuta, M.; Matsuda, T.; Hiramatsu, T.; Furuta, H.; Hirao, T. RF Power and Thermal Annealing Effect on the Properties of Zinc Oxide Films Prepared by Radio Frequency Magnetron Sputtering. *Res. Lett. Mater. Sci.* **2007**, *2007*, 1–5, doi:10.1155/2007/26459.

23. Gao, W.; Li, Z. ZnO thin films produced by magnetron sputtering. *Ceram. Int.* **2004**, *30*, 1155–1159, doi:10.1016/j.ceramint.2003.12.197.

24. Rosa, A.M.; Da Silva, E.P.; Amorim, E.; Chaves, M.; Catto, A.C.; Lisboa-Filho, P.N.; Bortoleto, J.R.R. Growth evolution of ZnO thin films deposited by RF magnetron sputtering. *J. Phys. Conf. Ser.* **2012**, *370*, doi:10.1088/1742-6596/370/1/012020.

25. Hideo Hosono, Masahiro Yasakawa, H.K. Novel oxide amorphous semiconductors : transparent conducting amorphous oxides Possible Candidate for HMCs. *J. Non. Cryst. Solids* **1996**, *203*, 334–344.

26. K. Nomura; H. Ohta; A. Takagi; T. Kamiya; M. Hirano; Hosono, H. Room-temperature fabrication of transparent flexible thin-film transistors using amorphous oxide semiconductors. *Nature* **2004**, *432*, 488.

27. Li, S.S.; Thurder, W.R. The dopant density and temperature dependence of electron mobility and resistivity in n-type silicon. *Solid. State. Electron.* **1977**, *20*, 609–616, doi:10.1016/0038-1101(77)90100-9.

28. Ma, J.; Sinha, S. Thermoelectric properties of highly doped n-type polysilicon inverse opals. *J. Appl. Phys.* **2012**, *112*, doi:10.1063/1.4758382.

29. Park, J.S.; Maeng, W.J.; Kim, H.S.; Park, J.S. Review of recent developments in amorphous oxide semiconductor thin-film transistor devices. *Thin Solid Films* **2012**, *520*, 1679–1693, doi:10.1016/j.tsf.2011.07.018.

30. Hays, D.C.; Gila, B.P.; Pearton, S.J.; Ren, F. Energy band offsets of dielectrics on InGaZnO4. *Appl. Phys. Rev.* **2017**, *4*, doi:10.1063/1.4980153.

31. Drabold, D.A.; Abtew, T.A. Defects in Amorphous Semiconductors: Amorphous Silicon. *Top. Appl. Phys.* **2006**, *104*, 245–268, doi:10.1007/11690320_11.

32. Nomura, K.; Ohta, H.; Ueda, K.; Kamiya, T.; Hirano, M.; Hosono, H. Thin-film transistor fabricated in single-crystalline transparent oxide semiconductor. *Science (80-.).* **2003**, *300*, 1269–1272, doi:10.1126/science.1083212.

33. Takagi, A.; Nomura, K.; Ohta, H.; Yanagi, H.; Kamiya, T.; Hirano, M.; Hosono, H. Carrier transport and electronic structure in amorphous oxide semiconductor, a-InGaZnO4. *Thin Solid Films* **2005**, *486*, 38–41, doi:10.1016/j.tsf.2004.11.223.

34. Nomura, K.; Kamiya, T.; Ohta, H.; Ueda, K.; Hirano, M.; Hosono, H. Carrier transport in transparent oxide semiconductor with intrinsic structural randomness probed using single-crystalline InGaO3(ZnO) 5 films. *Appl. Phys. Lett.* **2004**, *85*, 1993–1995, doi:10.1063/1.1788897.

35. Jacoboni, C.; Canali, C.; Ottaviani, G.; Alberigi Quaranta, A. A review of some charge transport properties of silicon. *Solid State Electron.* **1977**, *20*, 77–89, doi:10.1016/0038-1101(77)90054-5.

36. Kamiya, T.; Nomura, K.; Hosono, H. Origin of definite Hall voltage and positive slope in mobility-donor density relation in disordered oxide semiconductors. *Appl. Phys. Lett.* **2010**, *96*, 1–4, doi:10.1063/1.3364131.

37. Hosono, H. Ionic amorphous oxide semiconductors: Material design, carrier transport, and device application. *J. Non. Cryst. Solids* **2006**, *352*, 851–858, doi:10.1016/j.jnoncrysol.2006.01.073.

38. Kimura, M.; Nakanishi, T.; Nomura, K.; Kamiya, T.; Hosono, H. Trap densities in amorphous- InGaZn O4 thin-film transistors. *Appl. Phys. Lett.* **2008**, *92*, 1–4, doi:10.1063/1.2904704.

39. Kamiya, T.; Nomura, K.; Hosono, H. Origins of High Mobility and Low Operation Voltage of Amorphous Oxide TFTs: Electronic Structure, Electron Transport, Defects and Doping*. *J. Disp. Technol.* **2009**, *5*, 468–483, doi:10.1109/jdt.2009.2034559.

40. Nomura, K.; Kamiya, T.; Yanagi, H.; Ikenaga, E.; Yang, K.; Kobayashi, K.; Hirano, M.; Hosono, H. Subgap states in transparent amorphous oxide semiconductor, In-Ga-Zn-O, observed by bulk sensitive x-ray photoelectron spectroscopy. *Appl. Phys. Lett.* **2008**, *92*, doi:10.1063/1.2927306.

41. Nomura, K.; Kamiya, T.; Ikenaga, E.; Yanagi, H.; Kobayashi, K.; Hosono, H. Depth analysis of subgap electronic states in amorphous oxide semiconductor, a-In-Ga-Zn-O, studied by hard x-ray photoelectron spectroscopy. *J. Appl. Phys.* **2011**, *109*, doi:10.1063/1.3560769.

42. Tang, H.; Ide, K.; Hiramatsu, H.; Ueda, S.; Ohashi, N.; Kumomi, H.; Hosono, H.; Kamiya, T. Effects of thermal annealing on elimination of deep defects in amorphous In–Ga–Zn–O thin-film transistors. *Thin Solid Films* **2016**, *614*, 73–78, doi:10.1016/j.tsf.2016.03.005.

43. Körner, W.; Urban, D.F.; Elsässer, C. Origin of subgap states in amorphous In-Ga-Zn-O. *J. Appl. Phys.* **2013**, *114*, doi:10.1063/1.4826895.

44. Ide, K.; Kikuchi, Y.; Nomura, K.; Kimura, M.; Kamiya, T.; Hosono, H. Effects of excess oxygen on operation characteristics of amorphous In-Ga-Zn-O thin-film transistors. *Appl. Phys. Lett.* **2011**, *99*, 1–4, doi:10.1063/1.3633100.

45. Bang, J.; Matsuishi, S.; Hosono, H. Hydrogen anion and subgap states in amorphous In-Ga-Zn-O thin films for TFT applications. *Appl. Phys. Lett.* **2017**, *110*, doi:10.1063/1.4985627.

46. Ide, K.; Nomura, K.; Hosono, H.; Kamiya, T. Electronic Defects in Amorphous Oxide Semiconductors: A Review. *Phys. Status Solidi Appl. Mater. Sci.* **2019**, *216*, 1–28, doi:10.1002/pssa.201800372.

47. Kamiya, T.; Hosono, H. (Invited) Roles of Hydrogen in Amorphous Oxide Semiconductor. *ECS Trans.* **2013**, *54*, 103–113, doi:10.1149/05401.0103ecst.

48. Hanyu, Y.; Abe, K.; Domen, K.; Nomura, K.; Hiramatsu, H.; Kumomi, H.; Hosono, H.; Kamiya, T. Effects of high-temperature annealing on operation characteristics of a-In-Ga-Zn-O TFTs. *IEEE/OSA J. Disp. Technol.* **2014**, *10*, 979–983, doi:10.1109/JDT.2014.2352860.

49. Hino, A.; Takanashi, Y.; Tao, H.; Morita, S.; Ochi, M.; Goto, H.; Hayashi, K.; Kugimiya, T. Effects of thermal annealing on variations of electron traps in the channel region of amorphous In-Ga-Zn-O thin film transistor. *J. Vac. Sci. Technol. B, Nanotechnol. Microelectron. Mater. Process. Meas. Phenom.* **2014**, *32*, 031210, doi:10.1116/1.4876155.

50. CHITTICK RC; ALEXANDER JH; STERLING HF Preparation and Properties of Amorphous Silicon. *Electrochem Soc-J* **1969**, *116*, 77–81, doi:10.1149/1.2411779.

51. Paul, W.; Anderson, D.A. Properties of amorphous hydrogenated silicon, with special emphasis on preparation by sputtering. *Sol. Energy Mater.* **1981**, *5*, 229–316, doi:10.1016/0165-1633(81)90001-0.

52. Lim, P.K.; Tam, W.K.; Yeung, L.F.; Lam, F.M. Effect of hydrogen on dangling bond in a-Si thin film. *J. Phys. Conf. Ser.* **2007**, *61*, 708–712, doi:10.1088/1742-6596/61/1/142.

53. Scheller, L.P.; Weizman, M.; Simon, P.; Fehr, M.; Nickel, N.H. Hydrogen passivation of polycrystalline silicon thin films. *J. Appl. Phys.* **2012**, *112*, 4–7, doi:10.1063/1.4752268.

54. Pankove, J.I. Photoluminescence recovery in rehydrogenated amorphous silicon. *Appl. Phys. Lett.* **1978**, *32*, 812–813, doi:10.1063/1.89925.

55. Robertson, J. a-Si:H. **1985**, *31*, 3817–3821.

56. Gerke, S.; Becker, H.W.; Rogalla, D.; Hahn, G.; Job, R.; Terheiden, B. Morphology and Hydrogen in Passivating Amorphous Silicon Layers. *Energy Procedia* **2015**, *77*, 791–798, doi:10.1016/j.egypro.2015.07.112.

57. Moreno, M.; Ambrosio, R.; ArturoTorres; Torres, A.; Rosales, P.; Itzmoyotl, A.; Domínguez, M. Amorphous, Polymorphous, and Microcrystalline Silicon Thin Films Deposited by Plasma at Low Temperatures. *Cryst. Non-crystalline Solids* **2016**, doi:10.5772/63522.

58. Thomas, D.G.; Lander, J.J. Hydrogen as a donor in zinc oxide. *J. Chem. Phys.* **1956**, *25*, 1136–1142, doi:10.1063/1.1743165.

59. Hutson, A.R. Hall effect studies of doped zinc Oxide single crystals. *Phys. Rev.* **1957**, *108*, 222–230, doi:10.1103/PhysRev.108.222.

60. Heiland, G.; Mollwo, E.; Stöckmann, F. Electronic Processes in Zinc Oxide. *Solid State Phys. - Adv. Res. Appl.* **1959**, *8*, 191–323, doi:10.1016/S0081-1947(08)60481-6.

61. Van De Walle, C.G. Hydrogen as a cause of doping in zinc oxide. *Phys. Rev. Lett.* **2000**, *85*, 1012–1015, doi:10.1103/PhysRevLett.85.1012.

62. Shi, G.A.; Stavola, M.; Pearton, S.J.; Thieme, M.; Lavrov, E. V.; Weber, J. Hydrogen local modes and shallow donors in ZnO. *Phys. Rev. B - Condens. Matter Mater. Phys.* **2005**, *72*, 1–8, doi:10.1103/PhysRevB.72.195211.

63. Jokela, S.J.; McCluskey, M.D. Structure and stability of O-H donors in ZnO from high-pressure and infrared spectroscopy. *Phys. Rev. B - Condens. Matter Mater. Phys.* **2005**, *72*, 1–4, doi:10.1103/PhysRevB.72.113201.

64. Wardle, M.G.; Goss, J.P.; Briddon, P.R. First-principles study of the diffusion of hydrogen in ZnO. *Phys. Rev. Lett.* **2006**, *96*, 1–4, doi:10.1103/PhysRevLett.96.205504.

65. Nahm, H.H.; Park, C.H.; Kim, Y.S. Bistability of hydrogen in ZnO: Origin of doping limit and persistent photoconductivity. *Sci. Rep.* **2014**, *4*, 1–5, doi:10.1038/srep04124.

66. Du Ahn, B.; Shin, H.S.; Kim, H.J.; Park, J.S.; Jeong, J.K. Comparison of the effects of Ar and H2 plasmas on the performance of homojunctioned amorphous indium gallium zinc oxide thin film transistors. *Appl. Phys. Lett.* **2008**, *93*, doi:10.1063/1.3028340.

67. Sato, A.; Abe, K.; Hayashi, R.; Kumomi, H.; Nomura, K.; Kamiya, T.; Hirano, M.; Hosono, H. Amorphous In-Ga-Zn-O coplanar homojunction thin-film transistor. *Appl. Phys. Lett.* **2009**, *94*, 18–21, doi:10.1063/1.3112566.

68. Shao, L.; Nomura, K.; Kamiya, T.; Hosono, H. Operation characteristics of thin-film transistors using very thin amorphous In-Ga-Zn-O channels. *Electrochem. Solid-State Lett.* **2011**, *14*, doi:10.1149/1.3555070.

69. Kamiya, T.; Nomura, K.; Hosono, H. Subgap states, doping and defect formation energies in amorphous oxide semiconductor a-InGaZnO 4 studied by density functional theory. *Phys. Status Solidi Appl. Mater. Sci.* **2010**, *207*, 1698–1703, doi:10.1002/pssa.200983772.

70. Miyase, T.; Watanabe, K.; Sakaguchi, I.; Ohashi, N.; Domen, K.; Nomura, K.; Hiramatsu, H.; Kumomi, H.; Hosono, H.; Kamiya, T. Roles of Hydrogen in Amorphous Oxide Semiconductor In-Ga-Zn-O: Comparison of Conventional and Ultra-High-Vacuum Sputtering. *ECS J. Solid State Sci. Technol.* **2014**, *3*, Q3085–Q3090, doi:10.1149/2.015409jss.

71. Toda, T.; Wang, D.; Jiang, J.; Hung, M.P.; Furuta, M. Quantitative analysis of the effect of hydrogen diffusion from silicon oxide etch-stopper layer into amorphous In-Ga-Zn-O on thin-film transistor. *IEEE Trans. Electron Devices* **2014**, *61*, 3762–3767, doi:10.1109/TED.2014.2359739.

72. Nomura, K.; Kamiya, T.; Hosono, H. Effects of Diffusion of Hydrogen and Oxygen on Electrical Properties of Amorphous Oxide Semiconductor, In-Ga-Zn-O. *ECS J. Solid State Sci. Technol.* **2013**, *2*, P5–P8, doi:10.1149/2.011301jss.

73. Hanyu, Y.; Abe, K.; Domen, K.; Nomura, K.; Hiramatsu, H.; Kumomi, H.; Hosono, H.; Kamiya, T. Effects of high-temperature annealing on operation characteristics of a-In-Ga-Zn-O TFTs. *IEEE/OSA J. Disp. Technol.* **2014**, *10*, 979–983, doi:10.1109/JDT.2014.2352860.

74. Hanyu, Y.; Domen, K.; Nomura, K.; Hiramatsu, H.; Kumomi, H.; Hosono, H.; Kamiya, T. Hydrogen passivation of electron trap in amorphous In-Ga-Zn-O thin-film transistors. *Appl. Phys. Lett.* **2013**, *103*, 2011–2014, doi:10.1063/1.4832076.

75. Nomura, K.; Kamiya, T.; Ohta, H.; Hirano, M.; Hosono, H. Defect passivation and homogenization of amorphous oxide thin-film transistor by wet O2 annealing. *Appl. Phys. Lett.* **2008**, *93*, 1–4, doi:10.1063/1.3020714.

76. Magari, Y.; Aman, S.G.M.; Koretomo, D.; Masuda, K.; Shimpo, K.; Makino, H.; Kimura, M.; Furuta, M. Record-High-Performance Hydrogenated In-Ga-Zn-O Flexible Schottky Diodes. *ACS Appl. Mater. Interfaces* **2020**, doi:10.1021/acsami.0c12638.

77. Noh, H.Y.; Kim, J.; Kim, J.; Lee, M.; Lee, H. Role of Hydrogen in Active Layer of Oxide- Semiconductor-Based Thin Film Transistors. **2019**, doi:10.3390/cryst9020075.

78. Vidor, F.F.; Meyers, T.; Hilleringmann, U. Flexible electronics: Integration processes for organic and inorganic semiconductor-based thin-film transistors. *Electron.* **2015**, *4*, 480–506, doi:10.3390/electronics4030480.

Chapter 2

Development and analysis of the SnO_x material for p-type channel TFT application

This chapter describes the research of OS with p-type conductivity based on tin oxide (SnO_x) for TFT application. Most of the OS materials are those with n-type conductivity. However, p-type materials development is important because achieving high performance p-type oxide TFTs will promote a new era for electronics in rigid and flexible substrates. In addition, it will allow the production of complementary metal-oxide-semiconductor (CMOS) logic devices and make possible use of highly compact circuits with low power consumption.

Optimization and development of a reference synthesis process for obtaining the films with p-type conductivity is presented. Both the comprehensive analysis of thin-film properties and the fabrication of TFTs confirming the nature of p-type conductivity were performed. Optimal process window was developed, which is very narrow and limited to control due to the rapid and easy oxidation of Sn in oxygen-excess condition and the instability of SnO at 250 °C.

In order to optimize and improve the characteristics of both the thin-films and TFT, we focused on the H doping to SnO_x films. The effects of different H ratios on the change of optical, structural, electrical properties, chemical composition, and TFT performance were investigated. Both the positive and negative effects of H doped SnO_x films were found. Thus, it was found that H doping resulted in the change of the initial $Sn/SnO/SnO_2$ phase composition. Initial metal content in the film decreased by 3% suggesting additional formation of tin vacancies (V_{Sn}) and V_{Sn}–H complexes, resulting in increased concentration of holes. In addition, the SnO_x films deposition in H containing atmosphere leads to oxygen vacancy (V_O) termination by H. This substitution results in formation of $Sn–H^+$ bonds, which leads to slight increase in Hall mobility of holes after annealing because of reduction of carrier traps. Thus, the H doping can be used as one of the ways to improve the characteristics of p-type TFT.

2.1. Introduction

Oxide semiconductors (OS) have been attracting attention in the last fifteen years due to their promising electrical and optical properties for various different applications including thin film transistors (TFTs), complementary metal–oxide–semiconductor (CMOS) logic devices, and transparent electronics [1,2]. However, most of the OS materials used in these applications are those with n-type conductivity, for instance InGaZnO, ZnO, InGaO, InZnO, GaZnO. Figure 2.1 represents the research activity trend for various oxide material development over the two decades. As can be seen, most of the OS materials possess n-type conductivity, while p-type strongly lagged behind for over a decade, and research interest is only about 1% [3].

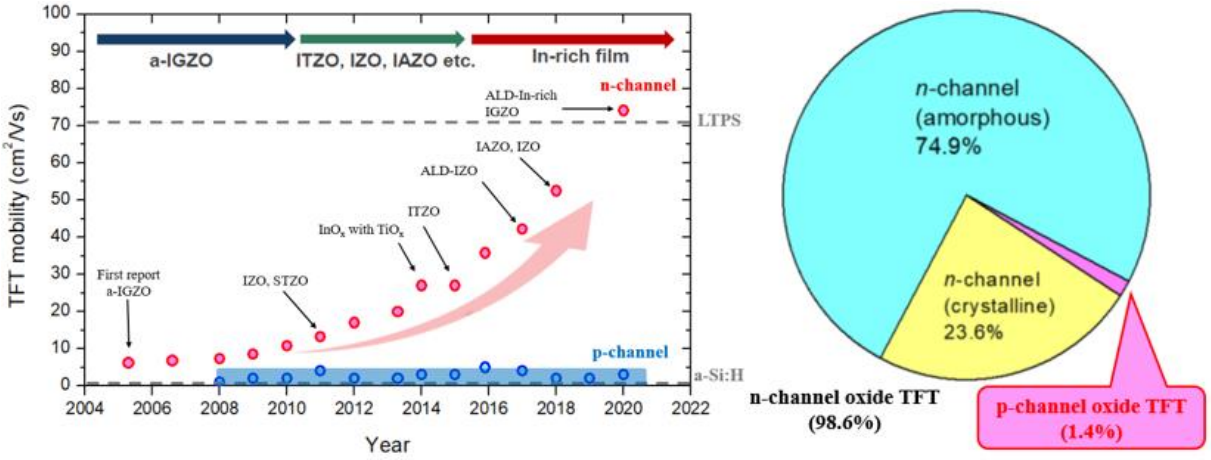

Figure 2.1 Progress of TFT mobility development for oxide based TFTs [3].

However, p-type materials development is important because achieving high performance p-type oxide TFTs will promote a new era for electronics in rigid and flexible substrates, away from silicon. Moreover, it will allow the production of CMOS and make possible use of highly compact circuits with low power consumption. Nevertheless, the manufacturing of devices based on p-type conductivity materials is still a challenging task due to several reasons. First, the valence band maximum (VBM) consists of O *2p* orbitals with strong directivity and transport of holes in p-type material can be easily degraded by bond angle distortion, while for n-type the electron transport is controlled by large spatial overlap of symmetrical *ns* metal orbitals. Second, the high subgap density of states near VBM, which influences on transport due to the trapping the holes.

2.2. Review of oxide semiconductors with p-type conductivity

Nevertheless, there are a few promising transparent materials with p-type conductivity, such as Cu_2O, SnO, NiO, which possess suitable optical and electrical properties that are comparable with n-type material capabilities. Figure 2.2 shows the total number of recent publications on the study of various materials with p-type conductivity [3]. Thus, the cuprous oxide (Cu_2O) is a p-type conductivity semiconductor with a band gap of 2.2 eV. It demonstrates the high mobility of holes of 60 cm^2/Vs for polycrystalline films [4], 90 cm^2/Vs for epitaxial grown films [5], and about 100 cm^2/Vs in monocrystalline form [6]. Despite very high Hall mobility, the main disadvantages of Cu_2O include its low concentration of holes (10^{15} - 10^{16} cm^{-3}) and difficulty in controlling it due to the easier oxidation at low temperatures. Moreover, real device performance, such as μ_{FE}, usually does not typically exceed 1 cm^2/Vs, which in combination with the high density of interface defects at the channel/insulator interface, limits the use of Cu_2O p-type channel-based TFTs [5,7–11]. Finally, the high quality Cu_2O films can be obtained at a high temperature process, making it impossible to apply them to flexible electronics.

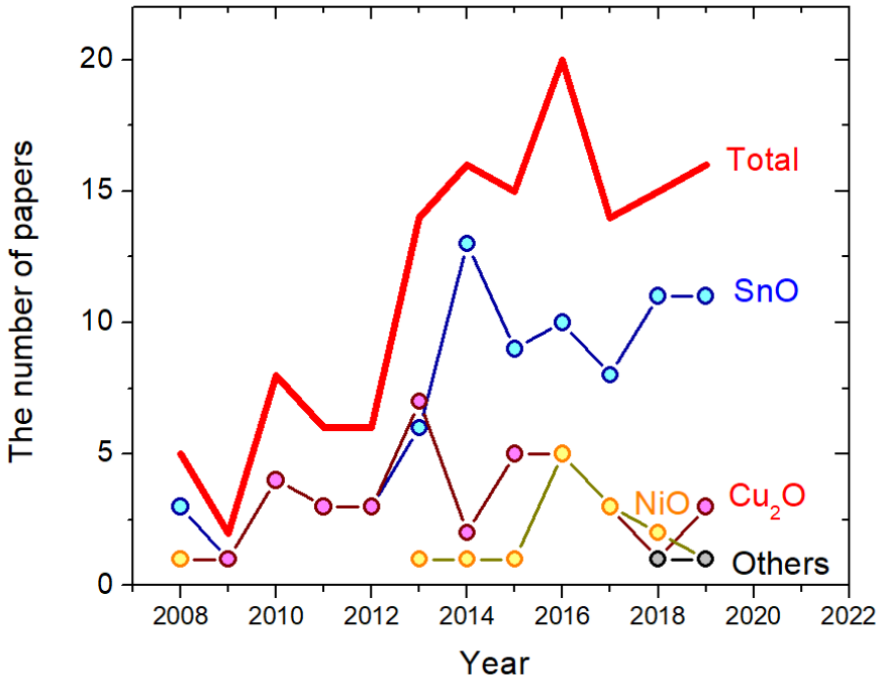

Figure 2.2 Number of publications in the field of OS materials with p-type conductivity [3].

In NiO the p-type conductivity is attributed to the spontaneously formed metal vacancies (V_{Ni}) and it is stable. However, their acceptor level is formed not relatively close to the VBM to ionize them, which limits the density of holes. On the other hand, this limit can be easily overcome by successful doping due to the unstable nature of the oxygen vacancies (V_O) which are known as "hole killers" [12]. Nevertheless, only few reports showed relatively suitable mobility about 5 cm^2/Vs, while most of them reported μ_{FE} values comparable to Cu_2O TFT of 1-2 cm^2/Vs [13,14].

2.3. SnO_x with p-type conductivity

In contrast, tin oxide is one of the most promising oxide semiconductor material because it has relatively high band gap 2.5 – 3.0 eV, acceptable high mobility with typical values of 2 - 5 cm^2/Vs and potentially higher, low-temperature process suitability about 200 – 300 °C. Moreover, its unique VBM and CBM structure which indicated the possibility to operate as n-type device if enough electron concentration exists in the film. This unique structure allows to produce the CMOS device with unipolar channel layout. Table 2.1 shows the typical electrical properties of the p-type SnO in comparison with other oxide material candidates.

Table 2.1 Comparative electrical film properties of p-type oxide semiconductor materials.

Material	Concentration of holes (cm^{-3})	Hall mobility (cm^2/Vs)	Optical band gap (eV)
Cu_2O	$\sim 10^{15}$	5 – 100	2.1 – 2.6
NiO	$10^{15} – 10^{17}$	20 – 40	3.6 – 4.0
SnO	$10^{16} – 10^{18}$	1 – 10	2.5 – 2.9

SnO_x exists in two well-known forms monoxide (SnO) and dioxide (SnO_2), as shown in Figure 2.3. SnO_2 is a more stable form with intrinsic n-type conductivity, and is actively used for multiple applications such as gas sensors, lithium-ion batteries, and transparent conducting oxides [15–17]. Monoxide SnO has $(n-1)d^{10}ns^2$ configuration with pseudoclosed ns^2 orbitals, which form VBM. The relatively high mobility of SnO is attributed to spherically spread *5s* orbitals of Sn^{2+} ($3d^{10}4s^2$) and their hybridization with O *2p* orbitals resulting in dispersed VBM [18,19]. There are two factors contributing to the ambipolar property of SnO. First is valence / conduction band structure. VBM is formed due to the co-contribution of Sn *5s* orbitals, while the CBM mainly

originates from Sn *5p* orbitals making it possible to conduct both holes and electrons without doping. Second is energy band configuration [20]. Figure 2.4 shows the band structure and energy band configuration of SnO [21].

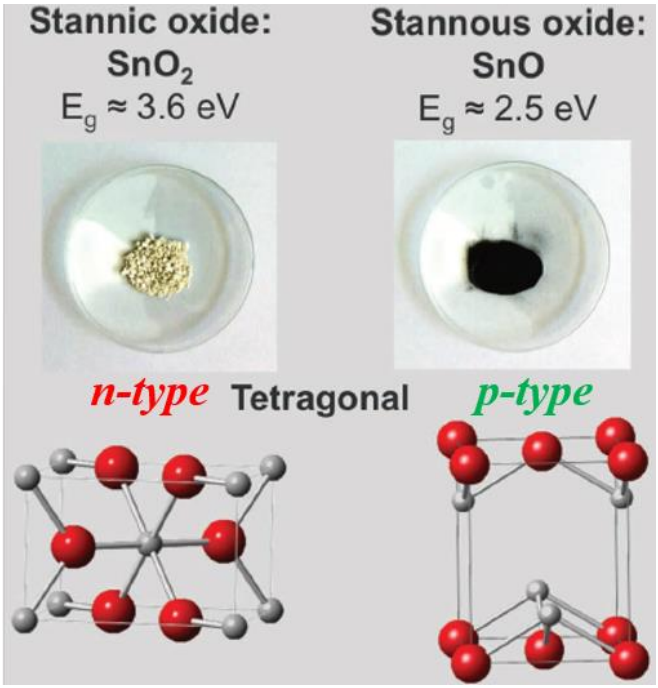

Figure 2.3 Unit cell structures of the SnO_x: monoxide (SnO) and dioxide (SnO_2) [21].

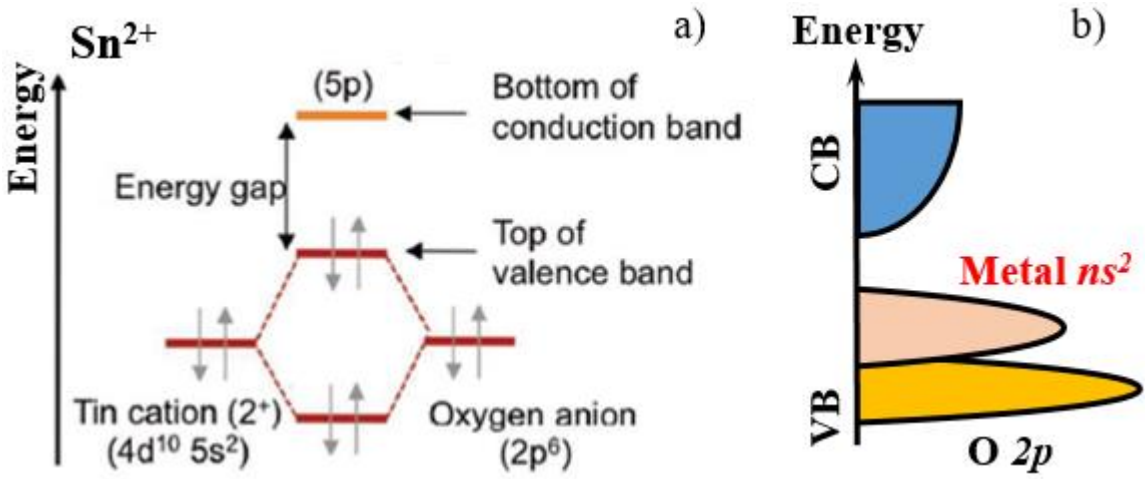

Figure 2.4 (a) Band structures and SnO [21]; (b) and energy band diagram [3].

The first principle calculations study revealed that the origin of p-type conductivity in SnO_x is mainly attributed to the tin vacancies (V_{Sn}) and interstitial oxygen (O_i) because of their low formation energy. These defects are fully ionized (V_{Sn}^{2-} *and* O_i^{2-}, respectively) and produce band deformation near VBM [20]. It leads to the formation of acceptor-like states which are charged negatively and located very close to VB tails. That is, the formation of an energy band level

localized close to the top of VBM which, for temperatures above the absolute zero, are partly filled by holes coming from the valence band, according to one of the quasi- chemical stoichiometric reactions [22]:

$$SnO \leftrightarrow Sn^{2+} + 2V_{Sn}^{-} + \frac{1}{2}O_2(1h/V_{Sn}) \tag{2.1a}$$

$$SnO \leftrightarrow Sn^{2+} + V_{Sn}^{2-} + \frac{1}{2}O_2(1h/V_{Sn}); \tag{2.1b}$$

$$SnO \leftrightarrow Sn^{2+} + V_{Sn}^{-} + O_{Sn}^{-} + \frac{1}{2}O_2 + V_O^{+}\left(\frac{2h}{V_{Sn}} + anti\ structured\ charged\ O\ defect, O_{Sn}\right) \tag{2.1c}$$

$$SnO \leftrightarrow Sn^{2+} + V_{Sn}^{-} + O_{Sn}^{-}(2h/V_{Sn} + O_{Sn}) \tag{2.1d}$$

The formation energy of the defect in SnO_x and defect concentration are shown in Figure 2.5 [20].

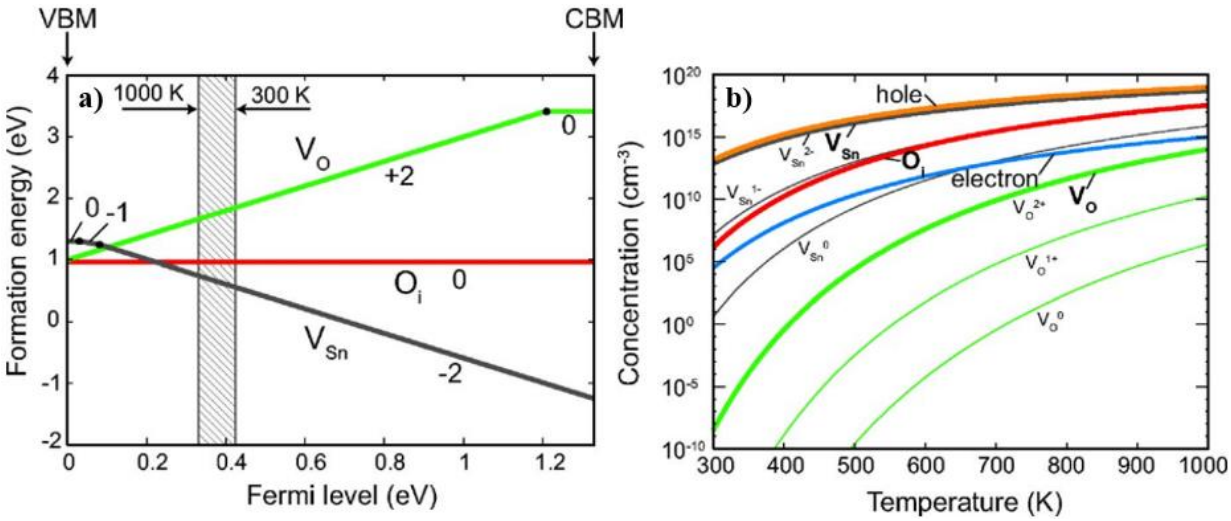

Figure 2.5 (a) Defect formation energies as a function of the Fermi level, (b) Defect concentrations as a function of temperature [20].

2.4. Development of SnO_x film with p-type conductivity

2.4.1. Thin film processing

In this work, 100 nm-thick SnO_x films were deposited on 4-inch glass substrate by DC magnetron sputtering in Ar/O_2 gas mixture with a total gas flow of 30 sccm using a 4-inch metal Sn target with purity 99.99%. All depositions were performed at room temperature. The O_2 gas ratio was defined as $R[O_2]=(O_2/Ar+O_2)$. Figure 2.6 shows the schematic DC magnetron sputtering process in vacuum. Equipment and process parameters are shown in Table 2.2. Next, all films

were subject to post-deposition annealing (PDA) treatment. PDA plays an important role in the electrical, optical and structural properties of the thin film and devices. PDA promotes crystallization of initially amorphous films and the ratio of the V_O / V_{Sn} in the film can be controlled. In this work all films were mainly annealed using Rapid Thermal Annealing (RTA) technique in N_2 atmosphere for 1 h by MILA-3000 RTA furnace unless other is specified.

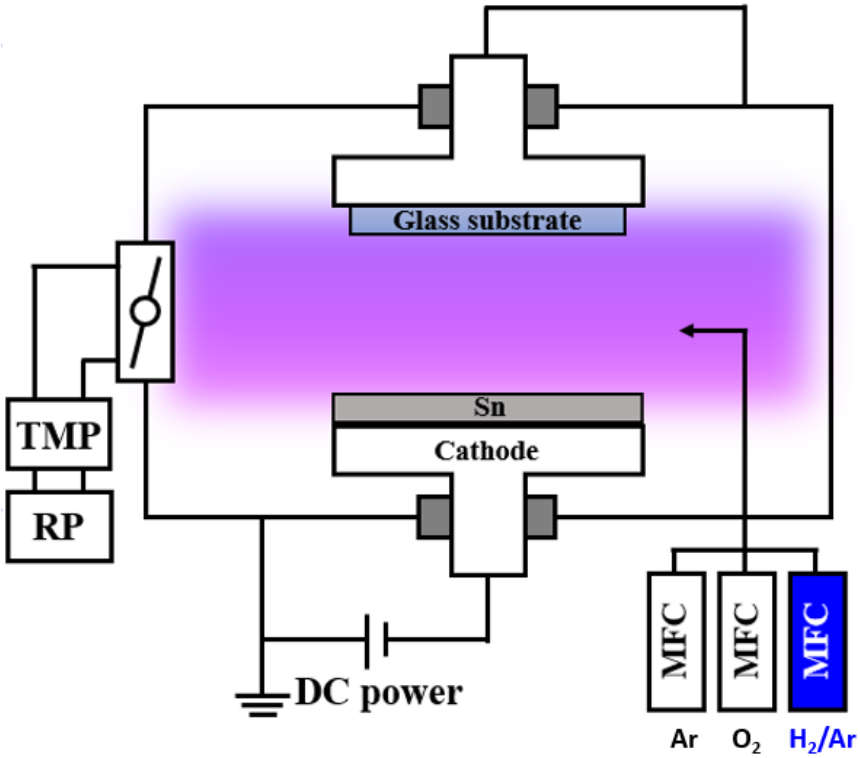

Figure 2.6 DC magnetron sputtering system for SnO_x film deposition in vacuum.

Table 2.2 Deposition parameters of the SnO_x thin films.

Target	100 mm Sn (99.99%)
Substrate	100 mm glass
Film thickness (nm)	100
Load lock pressure (Pa)	$< 1\times10^{-5}$
Base pressure (Pa)	5×10^{-5}
Deposition pressure (Pa)	0.4 - 2.0
DC power (W)	20
Total gas flow (Ar + O_2) (sccm)	30
Deposition temperature (°C)	
Oxygen ratio $R[O_2] = O_2 / (Ar + O_2)$	4 - 20
Substrate to target distance	82 mm

2.4.2. Effect of oxygen ratio on the properties of the SnO_x films

2.4.2.1. XRD structural analysis

Figure 2.7 shows the XRD pattern of the SnO_x filmed deposited at various $R[O_2]$ and after annealing at 200 °C, 250 °C, and 300 °C for 1h in the N_2 atmosphere. As can be seen in Figure 2.7a, the annealing at 200 °C is not enough to fully crystallize the films to the SnO with p-type conductivity deposited at $R[O_2]$ from 4% to 8%, while for $R[O_2]$ = 10% the film showed amorphous nature. All films demonstrated the highest peak intensity at 30.7° and with the slightly less intensity at 29.9° that correspond to the coexistence of several phases with the dominance of β-Sn metal one along (200) direction according to the XRD card (Tin #03-065-5224). These results suggest that the SnO_x is at an intermediate transition state since the metal phase is dominant and not completely oxidized. By increasing the annealing temperature to 250 °C the phase distribution changed drastically, as shown in Figure 2.7b. The highest intensity peak showed at 29.9° that relates to a preferred orientation along the (101) direction. Additionally, small intensity peaks were also observed at 30.7° and 31.7°. These peaks are related to the residual traces of metal, namely β-Sn along the (200) and (101) directions, respectively. Furthermore, an extra peak was detected at 18.4° only for deposited film at $R[O_2]$ = 8%. This peak refers to (001) orientation with a less effective mass of holes, and that can positively contribute to their higher mobility [23]. It is worthy to note that film deposited at $R[O_2]$ = 10% finally crystallized, but was still amorphous for $R[O_2]$ = 12%. The subsequent increase of the annealing temperature to 300 °C led to the disappearance of the residual metal traces, as can be seen in Figure 2.7c. This fact can be attributed to complete oxidation of metallic tin. The intensities of major p-type SnO related peaks at 29.8°, 33.3°, 37.3°, 47.8°, 50.9° and 57.4° also decreased. It should be noted that films deposited at $R[O_2]$ from 12% to 20% remained amorphous even at 300 °C (due to this fact the XRD patterns of the films deposited from 14% to 20% are not presented). The amorphous phase of these samples can be explained by the typical crystallization temperature of SnO_2 starting from 350 °C and higher [24,25].

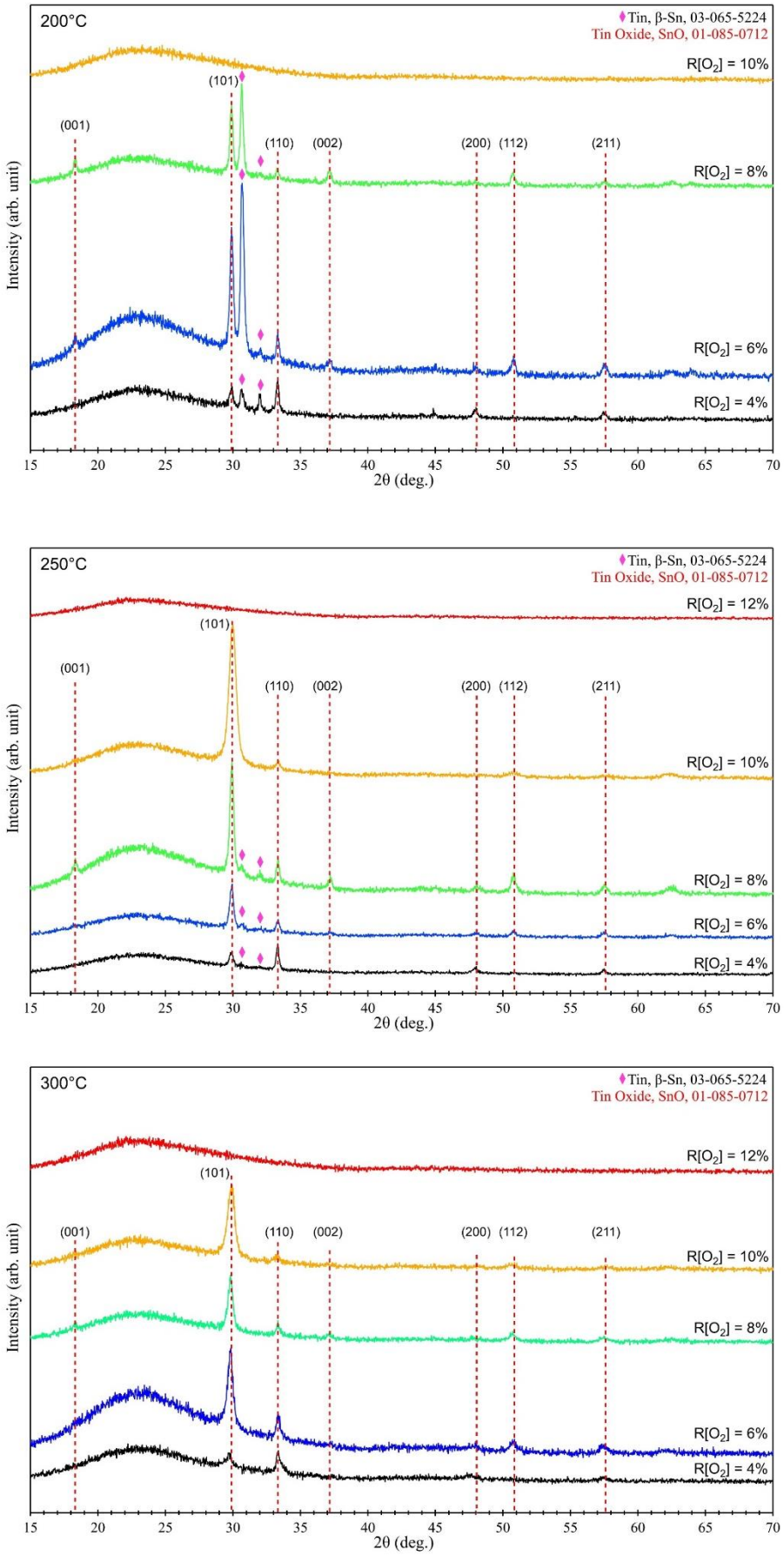

Figure 2.7 XRD patterns of SnO_x films deposited at different oxygen ratios and annealed in the N_2 atmosphere for 1 h at different temperatures: (a) 200 °C; (b) 250 °C; (c) 300 °C.

As was previously explained, SnO_x can exist in two forms SnO and SnO_2. SnO has a fundamental instability issue at the relatively high temperature of 250 °C and higher. This oxidation leads to the undesired formation of SnO_2 phase in the film, which is a more stable form having n-type conductivity. Geurtz proposed the following reaction upon the thermal treatment in 1984, which known as "Local disproportionate redistribution of internal oxygen" [26]:

$$x \cdot SnO \xrightarrow{270°C} (x-1) \cdot Sn + SnO_2 \tag{2.2}$$

On the other hand, the major disadvantage of using SnO is that Sn^{2+} can easily oxidize becoming Sn^{4+} in an oxygen-excess condition. Thus, the Sn valence state control is important, while at higher temperature the intermediate oxides formed. It should be noticed, that their formation strongly depends on synthesis condition, sputtering equipment and post-processing condition, because according to our XRD patterns no peaks of intermediate oxides were detected or the annealing temperature was not high enough for their formation. The intermediate oxides at high temperature can be formed through the several possible following reactions [27]:

$$2SnO \leftrightarrow SnO_2 + Sn \tag{2.2a}$$

$$3SnO \leftrightarrow Sn_2O_3 + Sn \tag{2.2b}$$

$$2\ Sn_2O_3 \leftrightarrow 3SnO_2 + Sn \tag{2.2c}$$

These results well agree with the previous reports, which showed a similar tendency both in the heating temperature influence and in the various R[O_2], as shown in Figure 2.8 [28].

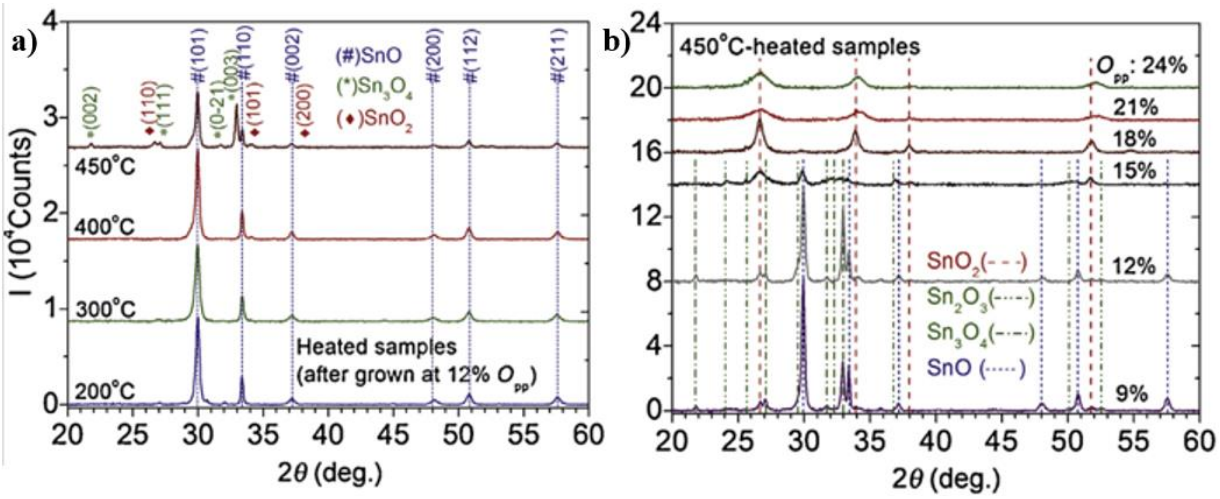

Figure 2.8 XRD pattern of SnO_x films: (a) annealing temperature influence at fixed O partial pressure; (b) O partial pressure influence at fixed annealing temperature [28].

2.4.2.2. Electrical and optical properties characterization

Optical properties are highly desired film characteristics since several important parameters can be extracted through the calculation after the measurement, such as optical bandgap (E_g) and absorption coefficient (α), and that from which the subgap defects can be evaluated qualitatively. Optical characterization technique was used to measure the optical transmittance (%T) and reflectance (%R) of the thin films by UV-NIR spectrophotometer (Hitachi Corp., U-4100) over a range of wavelengths (λ) between 200 nm and 2500 nm (Ultraviolet, visible and infrared). Then, absorption coefficient α can be determined from %T and %R spectra according to Lambert-Beer's law by the following equation:

$$\alpha = -\frac{1}{d}\ln\left(\frac{T}{1-R}\right), \tag{2.3}$$

where *d* is film thickness, *T* and *R* are transmittance and reflectance values obtained from measurement, respectively. Then, E_g energies can be estimated by Tauc method [29]. The α around the absorption edge can be expressed as a function of photon energy (*hν*) by following equation:

$$(\alpha h\nu)^n = A\left(h\nu - E_g\right), \tag{2.4}$$

where *h* is Planck constant, ν is frequency, A is a constant that depends on photon's energy, Eg optical band gap, n is transition type. Transition type can be 1/2 for direct allowed transitions, 3/2 for direct forbidden transitions, 2 for indirect allowed transitions, and 3 for indirect forbidden transitions. Plotting a graph of $(\alpha h\nu)^n$ as a function of (hν), the extrapolating the linear part of the curve to (hν) axis, the Eg value can be obtained. Figure 2.9a depicts Tauc's plot of the SnO_x films deposited at 1.0 Pa at various R[O_2] and annealed at 250 °C for 1 h in the N_2 atmosphere. Band gap energies as a function of R[O_2] are shown at Figure 2.9b and summarized in Table 2.3. Thus, the E_g values for a group of samples deposited at R[O_2] from 4% to 10% was in range from 2.86 eV to 2.93 eV, respectively. These values correspond to the SnO monoxide with p-type conductivity, with a typical value of 2.7 – 2.8 eV [30,31]. Further increase of R[O_2] to 12% led to a sharp increase of the band gap to 3.43 eV and for R[O_2] = 20% reached 3.98 eV. Thus, the clear transition point was observed at R[O_2] =10%. These results suggest the transition of SnO to SnO_2

with n-type conductivity[21]. Figure 2.10 shows the SnO_x film's appearance deposited at $R[O_2]$ of 8%, 10% and 12%. The higher the $R[O_2]$ the higher the transparency of the film.

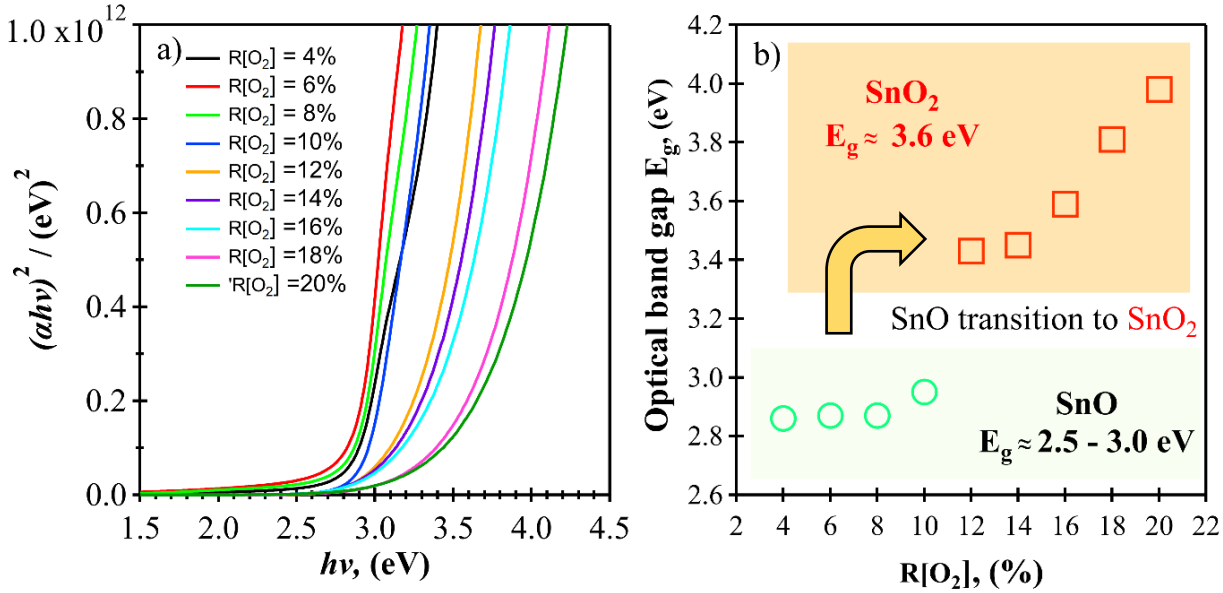

Figure 2.9 (a) Tauc's plot showing the experimental band gap of SnO_x films deposited at deposition pressure of 1.0 Pa and at different $R[O_2]$; (b) Band gap energies as a function of $R[O_2]$ obtained from Tauc's plot.

Table 2.3 Band gap energies of SnO_x films estimated from the Tauc's plot.

$R[O_2]$ (%)	4 – 10	12 – 20
E_g (eV)	2.86 – 2.95	3.43 – 3.98

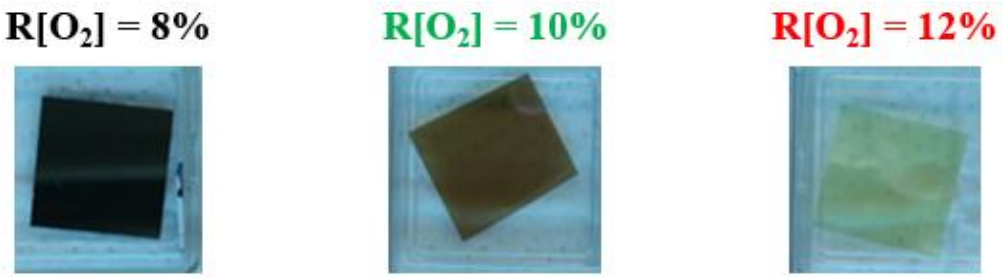

Figure 2.10 Appearance of the as-deposited SnO_x films deposited at different $R[O_2]$.

Next, the electrical properties were investigated. Figure 2.11 shows the summarized effect of the deposition process parameters on concentration of holes and Hall mobility. The films deposited at $R[O_2]$ from 4% to 10% and annealed at 200 °C showed contradictory and unstable results, demonstrating both positive and negative Hall coefficient (not presented). These results agree well with the XRD peaks and coexistence of several phases with the dominance of the metallic β-Sn one, which contributes to n-type conductivity in p-type SnO_x film. Additionally, it

was not possible to measure the samples deposited at R[O_2] = 12% and higher due to their extremely high resistivity and the limitation of Hall measurement instrument (10^5 Ω·cm). The stable and reliable Hall measurement results were obtained at the annealing temperature of 250 °C. All samples showed the positive Hall coefficient proving the p-type conductivity with concentration of holes (p) about 10^{17} – 10^{18} cm^{-3}, as can be seen in Figure 2.11b. An increase in R[O_2] from 4% to 8% led to an increase in the mobility of holes for all films after annealing at 250 °C and 300 °C. The highest mobility of holes of 1.65 cm^2/Vs with p = 5.1×10^{17} cm^{-3} was obtained at R[O_2] = 8% and annealing at 250 °C. Further increase in R[O_2] to 10% decreased the Hall mobility by half to 0.78 cm^2/Vs and 0.66 cm^2/Vs for 250 °C and 300 °C annealing temperature, as shown in Figure 2.11a. This mobility decrease can be explained by several reasons: (i) lack of SnO crystal plane alone (001) direction with less effective mass of holes, and (ii) undesired SnO_2 phase formation at higher R[O_2] and higher annealing temperature, as was explained in previous section. On the other hand, higher annealing temperature led to the disappearance of β-Sn metal residual traces along (200) and (101) direction. These results agree with the previous reports. It was reported that presence of the metal tin traces can positively affect the p-type conductivity behaviour in SnO_x films [23,32].

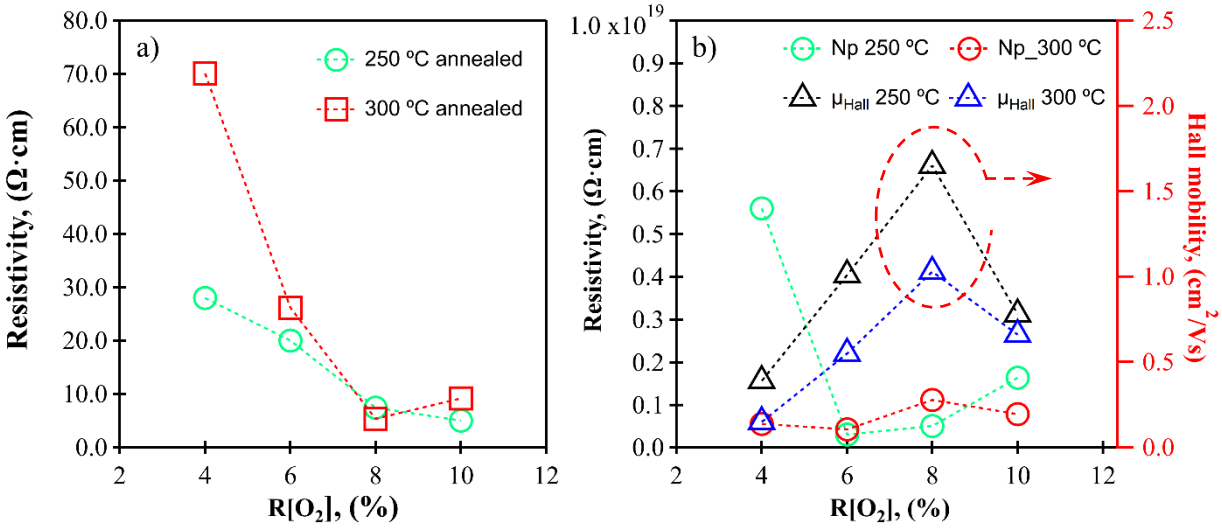

Figure 2.11 SnO_x films electrical properties as a function of R[O_2] after annealing.

2.4.3. Deposition pressure effect

To evaluate the deposition pressure effect on the SnO_x properties the 100-nm thick films was deposited at fixed $R[O_2]$ =8% and subsequent annealing at 250 °C. These film processing conditions were chosen as the best in terms of mobility and carrier concentration as was investigated and found in previous section. As can be seen in Figure 2.12, increase in deposition pressure (P_{Dep}) from 0.4 Pa to 2.0 Pa led to crystal structure change of the deposited films. Amorphous nature of the films deposited at 1.5 Pa and 2.0 Pa was observed after annealing. The preferential orientation was different for 0.4 Pa and 1.0 Pa with direction along (110) and (101), respectively. In order to support XRD data the sample deposited at 1.0 Pa was subject to Electron Backscatter Diffraction (EBSD) analysis. The EBSD image is shown in Figure 2.13. These results demonstrate the polycrystalline nature of the film with different crystallite orientation. Moreover, the film contains both small and large crystallites. E_g values extracted from the Tauc's plot were 2.84 eV and 2.88 eV for the 0.4 Pa and 1.0 Pa deposition pressure, respectively. Thermal annealing at 250 °C made no effect on optical properties and E_g values that remained on the same level of 3.65 eV and 4.02 eV for the P_{Dep} of 1.5 Pa and 2.0 Pa, respectively, as shown in Figure 2.14. Solid lines showed the Tauc's plot for the as-deposited films, while the dash-lines after annealing at 250 °C for 1h. Electrical properties showed increased Hall mobility of holes from 0.55 cm^2/Vs to 1.45 cm^2/Vs when P_{Dep} increased from 0.4 Pa to 1.0 Pa, respectively. While the concentration of holes was in the same range of $6.27\times10^{17} – 8.61\times10^{17}$ cm^{-3}. Similar to the previous section results when the films were deposited at $R[O_2]$ of 12% and higher, the resistivity of the films deposited at 1.5 Pa and 2.0 Pa significantly increased and reached the maximum of our Hall measurement instrument. Estimated optical E_g energies and electrical properties are summarized in Table 2.4 and Table 2.5, respectively. Thus, these results suggest that the deposition of SnO_x films at increasing P_{Dep} has a similar effect as the deposition at increased $R[O_2]$. It leads to additional oxidation and transition to SnO_2 with n-type conductivity deteriorating the p-type properties.

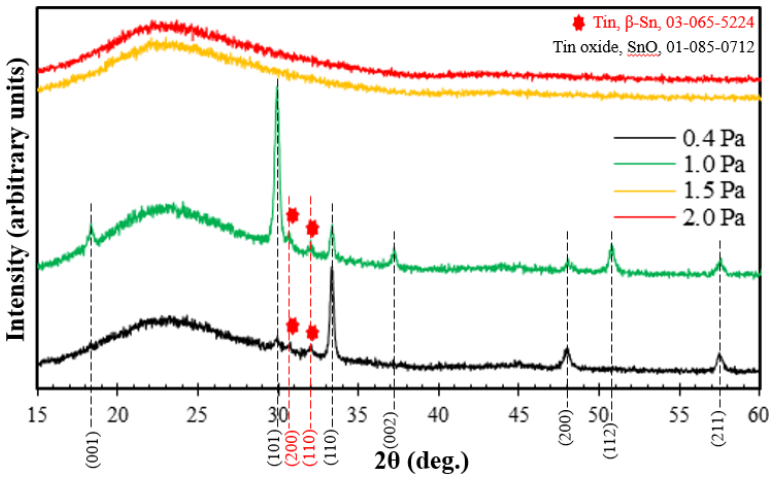

Figure 2.12 XRD patterns of SnO_x films deposited at different base pressures.

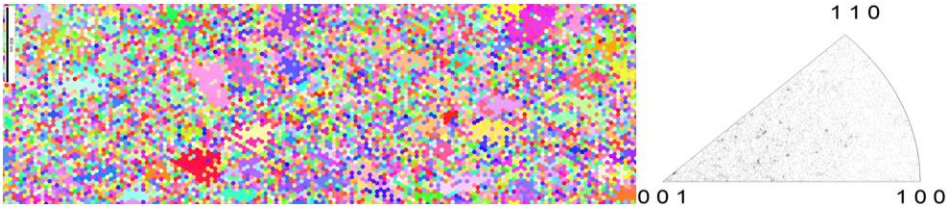

Figure 2.13 Polycrystalline structure image of of SnO_x deposited at R[O2] =8% and annealed at 250 °C for 1h in N_2 atmosphere obtained by Electron backscatter diffraction,

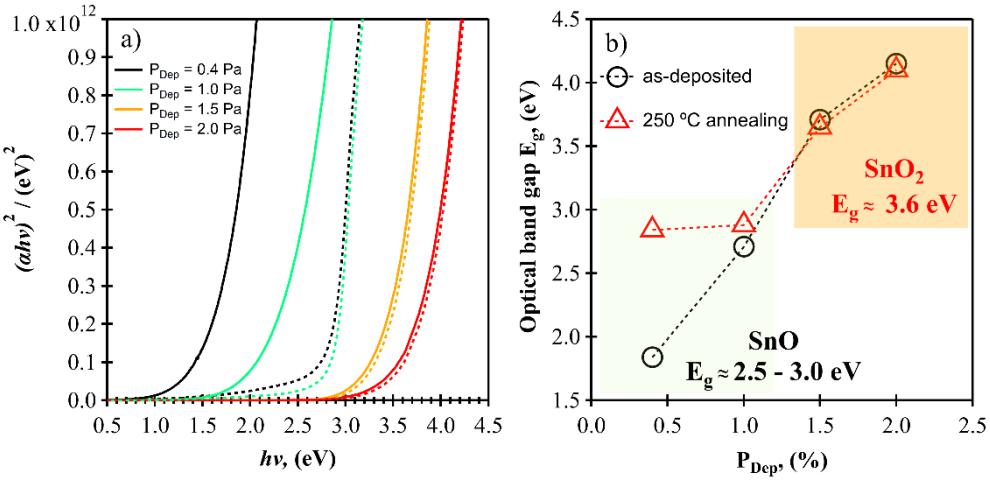

Figure 2.14 Optical results of the as-deposited and annealed SnO_x films: (a) Tauc's plot and; (b) E_g as a function of deposition pressure.

Table 2.4 E_g values of annealed SnO_x films deposited different P_{Dep}

P_{Dep} (Pa)	0.4	1.0	1.5	2.0
E_g (eV)	2.84	2.88	3.65	4.02

Table 2.5 Electrical properties of SnO_x films after annealing deposited at different P_{Dep}

	Resistivity (Ω·cm)	Holes concentration (cm^{-3})	Mobility of holes (cm^2/Vs)
0.4 Pa	28.16	6.27×10^{17}	0.55
1.0 Pa	6.17	8.61×10^{17}	1.45

2.5. Hydrogen doping of SnO_x films

2.5.1. Introduction

The major disadvantage of using SnO is Sn^{2+} oxidation to Sn^{4+} with the formation of SnO_2 with n-type conductivity. These conditions impose restrictions on the possibility of synthesizing high-quality SnO_x films both during the sputtering with a very narrow window process window (oxygen ration, deposition pressure) and annealing for film crystallization (temperature, annealing atmosphere).

With regard to the above limitations, the utilization of the new approaches to synthesizing SnO plays a key role in improving the SnO film properties. Garzon-Fontecha et. al showed that SnO film deposition in a nitrogen-containing atmosphere can lead to the substitution of O and Sn atoms by N ones. This substitution leads to changes in the optical and electrical properties, namely decrease in transmittance and increase in the carrier concentration of holes, respectively [31]. According to Nomura et. al, the p-channel SnO performance can be improved by annealing in the hydrogen atmosphere and its diffusion into the film, thereby reducing the defects [33]. Hsu et. al investigate p-type SnO film properties deposited in H deposition atmosphere, and different phase distribution variation [34]. Hydrogen is well known impurity and can be found in all sputtering equipment. It has a complicated role in oxide semiconductors. For example, in ZnO and IGZO, H acts as a shallow donor. Nevertheless, the hydrogen effects on defect formation and phase distribution in p-type SnO have not been explained in detail. Therefore, understanding the relationship between electrical properties and film crystallization, especially at a less-than-critical annealing temperature (about 250 °C – 270 °C, where SnO is still stable), is an important factor for further p-type SnO development and utilization in TFT technology. Our group has reported the H effect in a-IGZO. For instance, it was shown that H can suppress the electron concentration after annealing, as shown in Figure 2.15a [35]. Thus, this electron reduction of H effect can have a positive contirbution to suppression of electrons, which are minority charge carriers in p-type SnO_x film. In addition, the formation of V_O which act as a “holes killer” can be also reduced by H. We reported that the deposition of IGZO with H_2 adding reduces the number of V_O in both the

near-surface and bulk regions due to preferential hydrogen binding to metal forming the metal-hydrogen (*M-H*) bonds at V_O sites, as shown in Figure 2.15b [36].

Thus, we investigated the hydrogen effects on structural, optical, composition and electrical properties. It was found that adding a moderate amount of hydrogen to gas mixture during the SnO_x film synthesis led to the shift of crystallization point. Additionally, the initial content of metal, monoxide and dioxide phases has changed, which resulted in increased concentration of holes and average transmittance in visible range. 100-nm-thick SnO_x films were deposited on 4-inch glass substrate in $Ar/O_2/H_2$ gas mixture with the total gas flow 30 sccm at room temperature. The O_2 and H_2 gas ratios were defined as $R[O_2] = O_2/(Ar+O_2+H_2)$ and $R[H_2] = H_2/(Ar+O_2+H_2)$, respectively. The $R[O_2]$ was fixed at 8% for both hydrogen-free and hydrogen-containing films, while $R[H_2]$ was varied from 0% to 8%. All samples for further discussion are denoted as follows: hydrogen-free SnO (0-8); hydrogen-contained SnO:H (2-8), SnO:H (5-8), SnO:H (8-8) deposited at $R[H_2]$ of 2%, 5% and 8%, respectively. Deposition process parameters are shown in Table 2.6

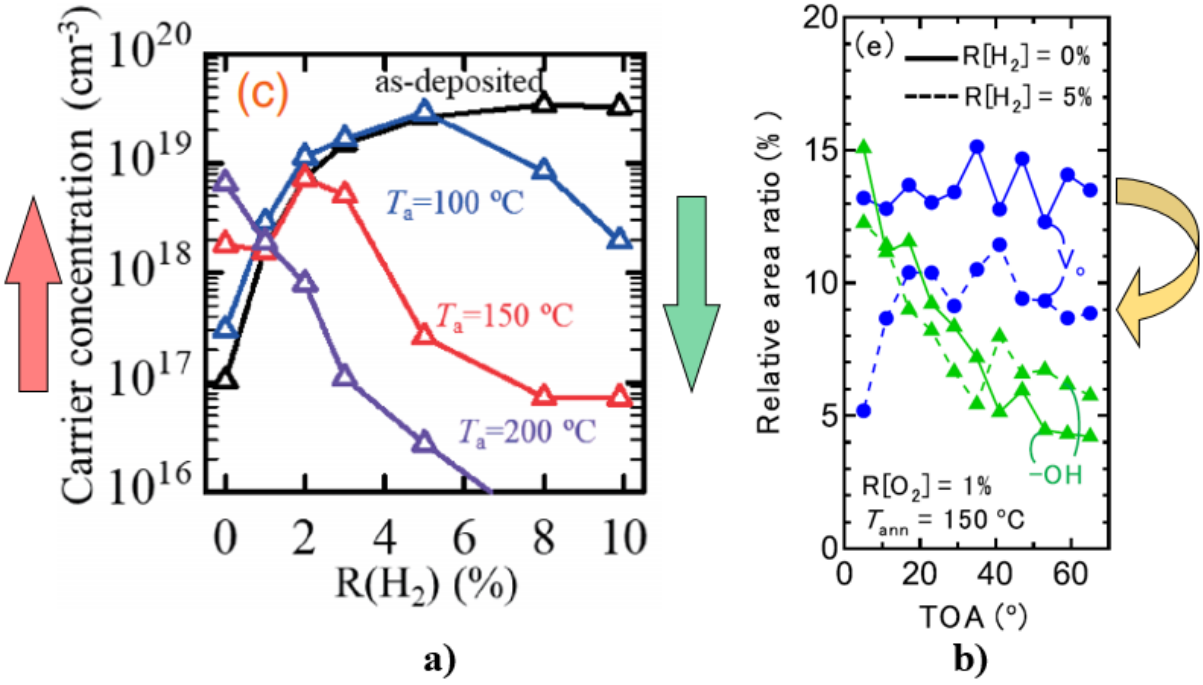

Figure 2.15 Hydrogen effects in a-IGZO: (a) carrier density reduction at low temperature [35]; (b) V_O reduction in the bulk and surface region revealed by HAXPES [36].

Table 2.6 Deposition parameters of the SnO_x thin films.

Target	100 mm Sn (99.99%)
Substrate	100 mm glass
Film thickness (nm)	100
Load lock pressure (Pa)	$< 1\times10^{-5}$
Base pressure (Pa)	5×10^{-5}
Deposition pressure (Pa)	1.0
DC power (W)	20
Total gas flow (H_2 + Ar + O_2) (sccm)	30
Deposition temperature (°C)	RT
$R[O_2] = O_2 / (Ar + O_2)$	8
$R[H_2] = H_2 / (Ar + O_2 + H_2)$	0 - 8
Substrate to target distance	82 mm

2.5.2. Optical properties of H doped SnO_x films.

Figure 2.16 shows the hydrogen doped SnO_x film's appearance after the deposition and after annealing at different temperatures. Thus, the H incorporation into the SnO_x film led to at least optical changes. The band gap energies (E_g) of SnO_x films were estimated from Tauc's plot and were plotted as a function of $R[H_2]$, as shown in Figure 2.17(a) and b, respectively.

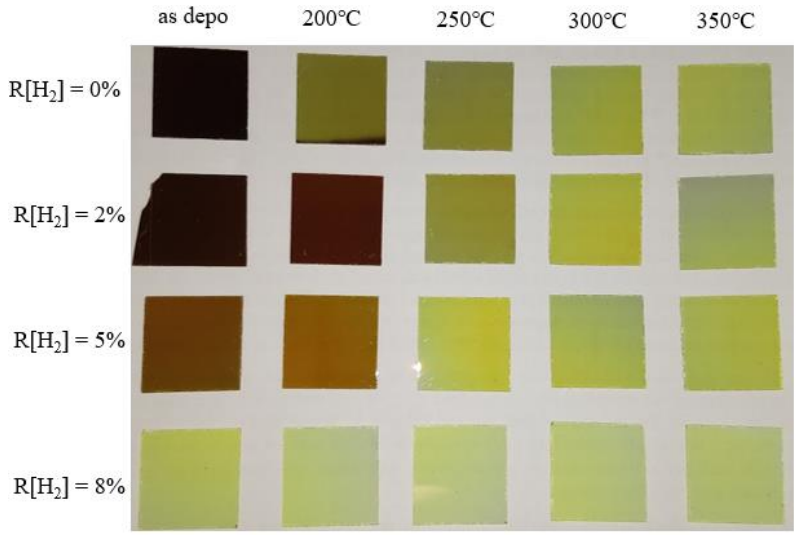

Figure 2.16 Samples appearance of Hydrogen doped SnO_x films deposited at different $R[H_2]$ after annealing in the N_2 atmosphere for 1 h.

As can be seen from Figure 2.17(b), an increase in the hydrogen ratio in the gas mixture during sputtering leads to an increase in the band gap of as-deposited samples. Figure 2.17(c) shows change in the E_g after annealing at different temperatures for 1h. The annealing had no

effect on the SnO:H (8-8) sample and the E_g was 3.41 eV within the whole annealing temperature range, while the E_g of SnO:H (2-8) and SnO:H (5-8) increased to 2.88 eV and 2.91 eV, respectively, after annealing at 250 °C. These E_g values are comparable to the value obtained from the SnO (0-8) film (2.87 eV), which is consistent with previous reports and corresponds to SnO with p-type conductivity [30,32,37]. On the other hand, the E_g change from 2.31 eV to 3.40 eV of the as-deposited films indicated the structural transition from SnO to SnO_2 phase having n-type conductivity with a typical E_g of 3.5 eV.

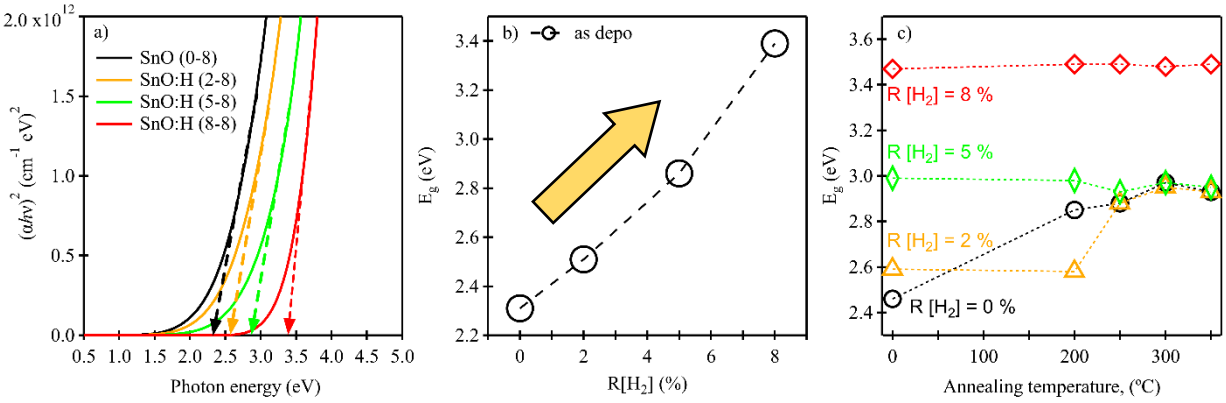

Figure 2.17 (a) Tauc's plot of as-deposited samples deposited at different R[H_2]; (b) Estimated band gap of SnO_x films as a function of R[H_2] before annealing; (c) E_g as a function of annealing temperature.

Figure 2.18 shows the transmittance spectra of the H doped SnO_x films, and the absorption coefficient which was calculated from the obtained data of transmittance and reflectance. As can be seen in Figure 2.18(a), the transmittance of SnO_x film increased in the entire visible spectra as H ratio increased during the film depositing. In addition, α was decreased within the band gap upon hydrogen incorporation, suggesting effective termination of the subgap defects which were originally formed during the deposition, as shown in Figure 2.18(b). After annealing at 250 °C, the trend continued, namely, deposition at a higher R[H_2] increased transmittance in the entire visible range and also reduced the α, as shown in Figure 2.18(c). In addition, the film deposited at a R[H_2] of 5% showed an additional decrease in α, while for films deposited at 0% and 2% remained almost unchanged, as can be seen in Figure 2.18(d). Thus, these results suggest that H incorporation into the SnO_x films during the deposition can improve film optical properties. The

average transmittance of the SnO_x films after annealing at 250 °C for 1h in N_2 atmosphere within visible range from 380 nm to 750 nm wavelength is summarized in Table 2.7. It can be seen that average transmittance of the SnO:H (5-8) sample increased by 17% compared to hydrogen-free SnO (0-8), while the α decreased by one order. It should be noticed that the overall optical data results suggest additional oxidation for H doped SnO_x films, which might affect and deteriorate both the film electrical properties and TFT either.

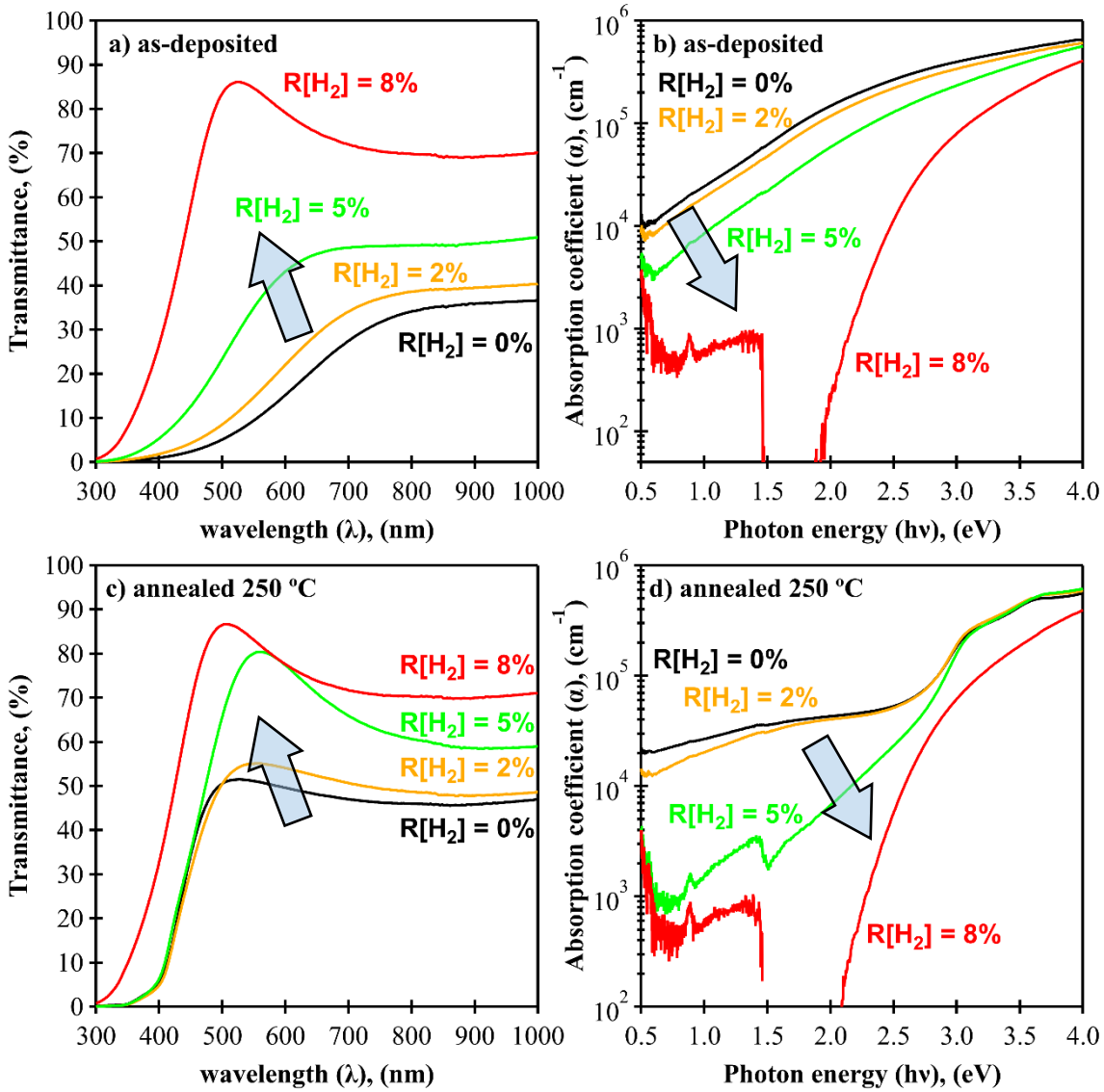

Figure 2.18 Optical properties of the H doped SnO_x films: (a) and (b) Transmittance and absorption coefficient of as-deposited films; (c) and (d) Transmittance and absorption coefficient of annealed film at 250 °C.

Table 2.7 Average transmittance of H doped SnO_x films in visible range (380 nm-750 nm)

$R[H_2]$ (%)	0	2	5	8
%T (250 °C)	41.77	43.66	58.57	71.13

2.5.3. XRD structural analysis and H effect on crystallization.

Figure 2.19 shows the XRD patterns of the H doped and hydrogen-free SnO_x films after annealing. The SnO (0-8) sample crystallized and polycrystalline nature after annealing at 200 °C, as shown in Figure 2.19(a). The highest peak of intensity was observed at 29.9°, which relates to a preferred orientation along the (101) direction. Small intensity peaks were also observed at 30.7° and 31.7°, which are related to the residual traces of β-Sn along the (200) and (101) directions, respectively [32,38,39]. In addition, an extra peak was detected at 18.4° and refers to (001) orientation, which can positively contribute to the higher mobility of holes due to their less effective mass [23]. The subsequent increase in annealing temperature led to a slight decrease in major p-type SnO peaks of the SnO (0-8) sample, while the residual traces of β-Sn practically disappeared and are barely noticeable on the diagram, as shown in Figure 2.19(b).

Surprisingly, the addition of H led to a shift in the initial crystallization point by 50 °C and the amorphous nature of the films was retained after annealing at 200 °C, Figure 2.19(a). SnO:H (2-8) and SnO:H (5-8) samples crystallized after subsequent annealing at 250 °C and showed polycrystalline structure with similar peaks as the SnO (0-8) sample. However, the SnO:H (8-8) sample remained amorphous even after annealing at 300 °C, Figure 2.19(c). This amorphous phase suggests the prevailing form of SnO_2 in the film with a typical crystallization temperature of 400 °C and above [24,25,40]. In addition, these XRD results of the SnO:H (8-8) film are in good agreement with the E_g values, shown in Figure 2.17(b). Full width at half maximum (FWHM) analysis of the main crystallization peak (101) revealed that H incorporation into the SnO_x film results in FWHM increase. Thus, the FWHM of the SnO:H (5-8) doubled to 0.47 compared with hydrogen-free SnO (0-8) sample of 0.25. Thus, the grain size decreased from 32.8 nm to 17.4 nm for SnO (0-8) and SnO:H (5-8) samples, respectively, and that which may influence on TFT performance due to grains boundary effect. Crystallization point shift can be explained by additional oxidation and SnO_2 phase development since the similar trend was observed for higher $R[O_2]$ without H adding, as was shown in the previous section.

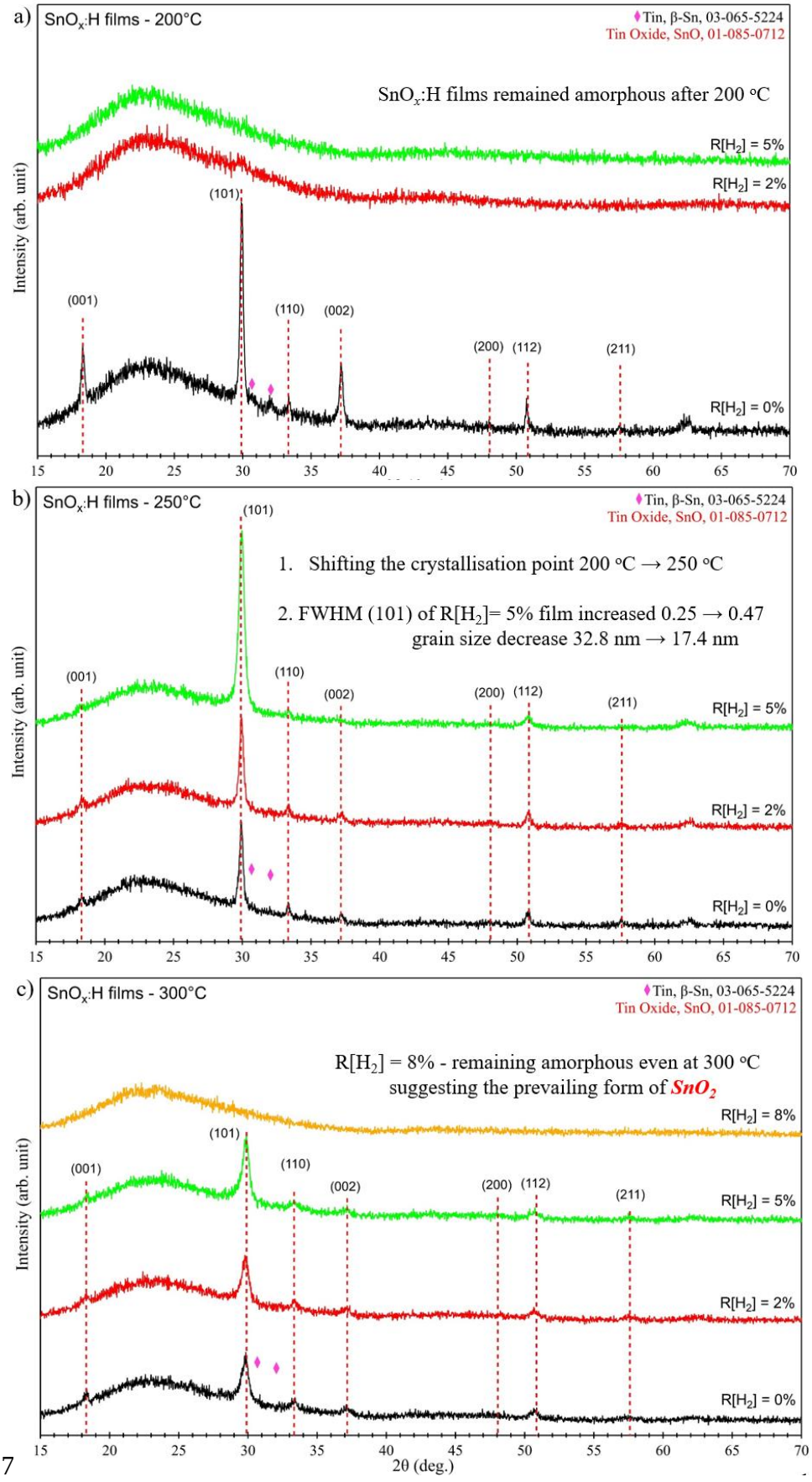

Figure 2.19 XRD patterns of the annealed SnO_x:H films deposited at $R[H_2]$ = 2% and 5% and at constant $R[O_2]$ = 8% after annealing at: (a) 200 °C; (b) 250 °C; (c) 300 °C.

2.5.4. Carrier concentration and mobility of holes

Figure 2.20 shows the resistivity of the films deposited at various R[H_2] with a constant R[O_2] of 8%. In order to confirm the p-type conductivity, a set of four samples with 7 mm × 7 mm dimension was prepared for Hall measurements for each film. Further, all samples were analyzed for the sign of the Hall coefficient. If all four samples showed a positive sign of Hall coefficient, then the film was attributed to p-type conductivity. However, some samples within the same measurement set showed different signs of the Hall coefficient. At that time, such data related to "ambipolar" behaviour with contradictory and unstable results.

The resistivity of as-deposited SnO (0-8) film was 18.1 Ω·cm, while both the positive and negative Hall sign were observed due to the influence of the metal content in the film. The film showed p-type conductivity with a resistivity of 3.0 Ω·cm and hole concentration of 2.5×10^{18} cm^{-3} after annealing at a temperature of 200 °C. Further annealing at 250 °C increased the resistivity to 10.7 Ω·cm and decreased the hole concentration to 5.89×10^{17} cm^{-3}, although the p-type conductivity was still preserved with a mobility of 1.17 cm^2/Vs.

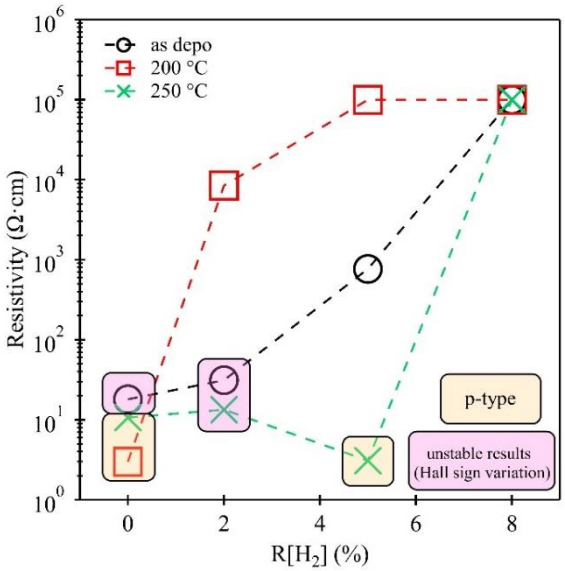

Figure 2.20 Resistivity of as-deposited and annealed SnO_x films deposited at various R[H_2] and R[O_2] = 8%.

On the other hand, when the film was deposited with H_2 gas, the SnO:H (0-8) sample showed interesting behaviour, which deserves further detailed analysis. At the beginning, the resistivity increased and reached the limit of our measurement instrument after annealing at 200 °C,

but a further increase in temperature to 250 °C led to a sharp drop in resistivity to 3.15 Ω·cm. This value is one third compared to the resistivity of the SnO (0-8) sample. The mobility of holes slightly increased from 1.17 cm^2/Vs to 1.45 cm^2/Vs for the SnO:H (5-8) sample. Moreover, the concentration of holes was 2.3 times higher than the hydrogen-free sample being 1.38×10^{18} cm^{-3} for SnO:H (5-8) and 5.89×10^{17} cm^{-3} for SnO (0-8), respectively. However, annealing did not change the resistivity of the SnO:H (8-8) sample, while SnO:H (2-8) showed contradictory and unstable results and demonstrated both positive and negative Hall sign even after annealing at 250 °C. These unstable results can be attributed to the low mobility of the films, the analysis of which is traditionally difficult for DC magnetic field measuring systems. Figures 2.21(a) and (b) show the resistivity and mobility of holes as a function of annealing temperature for SnO_x films deposited at different R[H_2], respectively. Hydrogen-containing SnO_x films showed abnormal change in resistivity, as shown in Figure 2.21(a). Thus, the higher the H ratio, the higher the resistivity of the as-deposited film. The resistivity of hydrogen-containing films increased after annealing at 200 °C and these films remained amorphous. On the contrary, the hydrogen-free SnO (0-8) film crystallized and it resulted in decreased resistivity after 200 °C annealing. However, further increase in annealing temperature to 250 °C led to a sharp drop of resistivity for H dope SnO_x films due to their final crystallization.

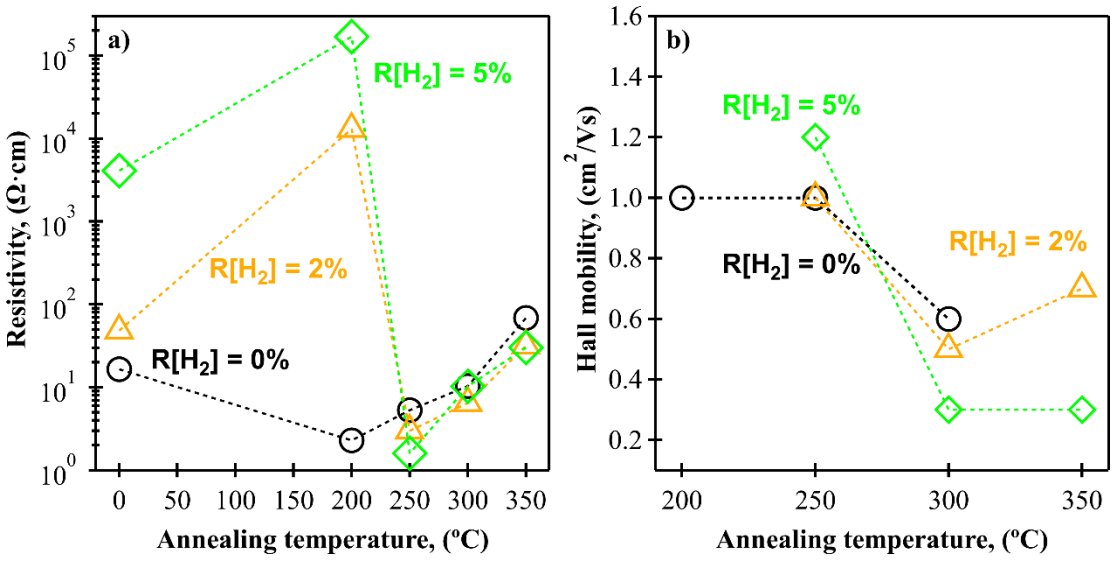

Figure 2.21 Electrical properties of the SnO_x films deposited at different R[H_2] as a function of annealing temperature: (a) film resistivity; (b) Hall mobility of holes.

2.5.5. Chemical bonding states analysis of H doped SnO_x films by HAXPES

The chemical bonding states of SnO_x films were evaluated by HAXPES in order to characterize their oxidation states and chemical composition. Figures 2.22(a)-(d) show Sn $3d_{5/2}$ spectra obtained from both the SnO (0-8) and SnO:H (5-8) samples before and after annealing at 250 °C. A noticeable difference is a shoulder in the region of lower binding energy was found between the as-deposited SnO (0-8) and SnO:H (5-8) samples, as shown in Figure 2.22(a), while an almost identical shape in the peaks was observed after annealing, Figure 2.22(c). The obtained Sn $3d_{5/2}$ spectra after deconvolution are shown in Figures 2.22(b) and (d). According to the best fitting, the corresponding binding energies were assigned to 484.0 eV, 485.3 eV and 485.8 eV as the Sn^0, Sn^{2+} and Sn^{4+} components, respectively [41–43]. Table 2.8 is a summary of the relative area ratio of the Sn, SnO and SnO_2 peaks. The initial content of SnO did not change in the SnO:H (5-8) sample compared with SnO (0-8) and was 55% for both as-deposited samples. In contrast, the content of Sn and SnO_2 decreased and increased by 4%, respectively. Thus, these results indicate that the introduction of hydrogen led to the additional oxidation of Sn and change in the initial state of SnO_2 in the film. Taking into account the increase in the E_g, as shown in Figure 2.17, and the shift in the crystallization point upon the addition of hydrogen in Figure 2.19, HAXPES results also indicate an additional development of the SnO_2 phase. Deposition of the SnO_x films at higher oxygen ratios has a similar effect, leading to a transition from a polycrystalline to an amorphous structure and SnO_2 formation [28]. Luo et. al reported that due to the difference between Sn^{4+}–O and Sn^{2+}–O bonds, such as distinct coordination number, bond angle and bond length, the presence of additional Sn^{4+} in the SnO_x matrix boosted structural disorder, resulting in an increase in the crystallization point [44].

Table 2.8 Relative area ratio of the Sn, SnO and SnO_2 in the SnO_x films deposited at an R[H_2] of 0% and 5% before and after annealing at 250 °C.

Annealing	Sample	Sn (%)	SnO (%)	SnO_2 (%)
as-depo	SnO	11.43	55.20	33.37
as-depo	SnO:H (5-8)	8.47	55.33	36.20
250 °C	SnO	0	76.76	23.24
250 °C	SnO:H (5-8)	0	72.95	27.05

Thus, additional development of SnO_2 phase in the H doped SnO_x film results in the shift of the crystallization point, as was observed by XRD analysis and shown in Figure 2.19. Analysis of the annealed samples showed no clear difference in the obtained Sn $3d_{5/2}$ peaks, Figure 2.22(c). The ratio of SnO:SnO_2 content in the film increased from (5:2) to (7:3) after annealing, suggesting Sn metal phase oxidation primarily to SnO. However, the SnO2 content increased by 4% in the SnO:H (5-8) sample compared with SnO (0-8).

Figures 2.22(e) and (f) show the O 1s spectra of SnO_x films. The difference in the obtained peaks is insignificantly small for the as-deposited samples, while the peaks after annealing are almost similar. The two clear distinguishable peaks after deconvolution were assigned to 529.2 eV and 529.7 eV, corresponding to SnO and SnO_2, respectively. The additional small peak at 530.7 eV was assigned to –OH groups. Comparison of O 1s spectra showed a similar tendency in the content difference of SnO and SnO_2 for the SnO:H (5-8) sample. The relative area ratio of the Sn, SnO and SnO_2 peaks after O 1s spectra deconvolution is summarized in Table 2.9. This is in good agreement with Sn $3d_{5/2}$ spectra and indicates the additional formation of SnO_2 phase after the addition of hydrogen to the gas mixture. However, comparison of –OH showed the opposite results. The observed difference is not significantly high enough to clearly claim the –OH effect due to the controversial nature of this peak, which corresponds to both chemisorbed oxygen [45] and hydroxyl groups [41]. We speculate that this difference is due to the influence of the film surface, which affects the signal of the bulk structure due to the Sn oxidation and the presence of SnO_2 on the surface [46].

Table 2.9 Relative area ratio of the Sn, SnO and SnO_2 in the SnO_x films deposited at an R[H_2] of 0% and 5% before and after annealing at 250 °C.

Annealing	Sample	SnO (%)	SnO_2 (%)	–OH (%)
as-depo	SnO	58.84	26.40	14.75
as-depo	SnO:H (5-8)	58.10	30.82	11.07
250 °C	SnO	62.57	24.69	12.74
250 °C	SnO:H (5-8)	60.88	26.54	12.57

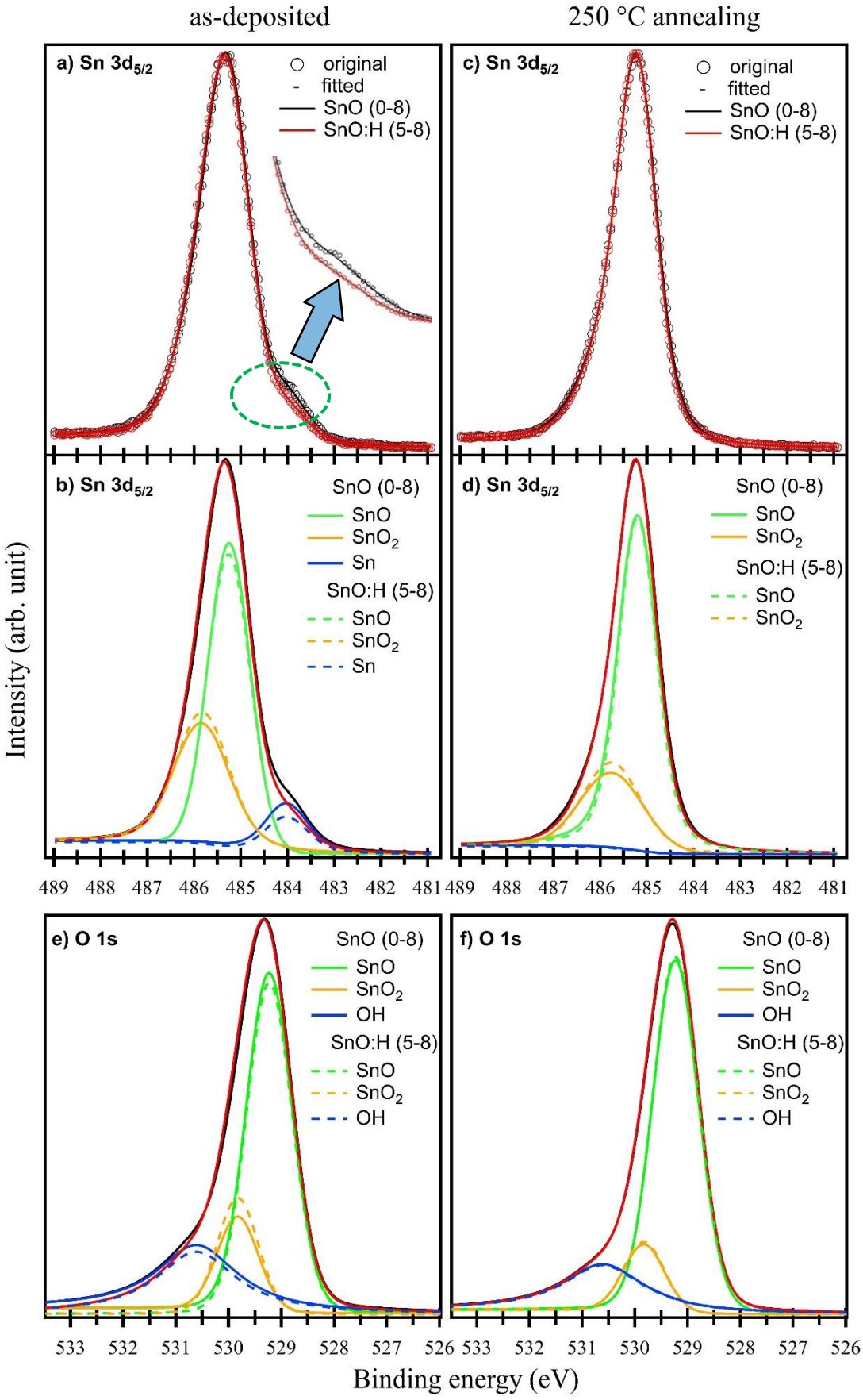

Figure 2.22 HAXPES analysis of SnO_x films: (a)–(b) Sn $3d_{5/2}$ core spectra of as-deposited samples; (c)–(d) Sn $3d_{5/2}$ core spectra after annealing at 250 °C; (e)–(f) O 1s core spectra of as-deposited samples and after annealing at 250 °C, respectively.

2.5.6. Thermal desorption spectroscopy analysis

In order to investigate such a sharp change in resistivity, optical band gap and structure transition, we performed a Thermal desorption spectroscopy (TDS). Figure 2.23 shows the TDS of the 100-nm-thick SnO_x film deposited on silicon substrate at different R[H_2]. The TDS chamber was pumped out to a base pressure of 5×10^{-8} Pa prior to analysis. Next, samples were heated at a constant heating rate of 30 °C per min. All spectra were normalized to sample weight for proper hydrogen comparison. There are two distinct peaks of desorption of both OH (m/z = 18) and O_2 (m/z = 32) at 200 °C. As can be seen, the higher the R[H_2] the greater the desorption of the hydrogen related groups (OH) in temperature range from 200 °C to 250 °C. This temperature range is the crystallization range of the films, as well as the transition point where the SnO can oxidize, leading to undesired additional formation of SnO_2 phase in the film. These results clearly indicate that H presences in the film as OH bonds. In addition, as shown in Figure 2.17 and 2.18 the E_g increased as R[H_2] increased and for the SnO:H (8-8) sample was typical for SnO_2. Therefore, TDS analysis suggests that transition from SnO to SnO_2 and the additional development of SnO_2 in the film upon H incorporation, as was revealed by HAXPES analysis, might be due to the formation of excess internal oxygen, and that which originates due to the increased amount of O–H groups or H_2O in the film, leading to oxidation to Sn^{4+}. While the higher temperature is required to break bonds of the *Sn-OH* complex.

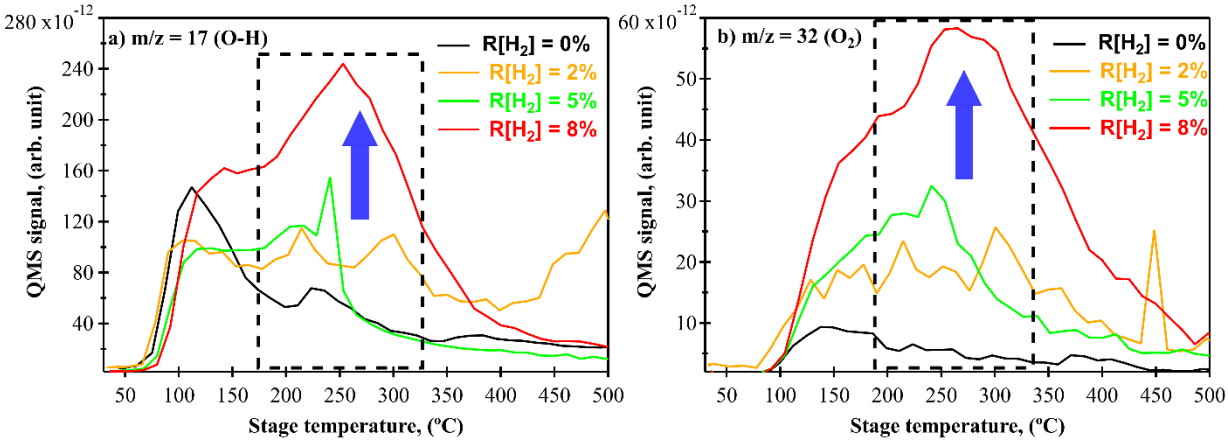

Figure 2.23 Thermal desorption spectra measured for H doped SnO_x films deposited on silicon substrate: (a) m/z = 17 (O–H); (b) m/z = 32 (O_2).

2.5.7. Role of native defects and hydrogen effect

There have been several studies to date that have reported the positive effect of residual traces of β-Sn on mobility [23,47]. However, according to XRD patterns the presence of residual Sn traces is practically absent for the SnO:H (5-8) sample. Therefore, the lack of Sn traces in combination with the decreased SnO and increased SnO_2 content in the film after annealing cannot fully explain the increased concentration of holes and mobility. It is known from first principle calculations that the main source of p-type conductivity in SnOx film is tin vacancies (V_{Sn}) due to their low formation energy [20]. According to HAXPES results the H adding suppressed the initial metal content in the as-deposited film by 3 % (Table 2.7). This result suggests the additional formation of V_{Sn}, which contributes to electrical properties. On the other hand, Varley et al. implemented a density functional theory in order to investigate the defect formation and H impurities effect in SnO [48]. Thus, the introduction of H impurities leads to the preferential formation of tin vacancy-hydrogen complexes (V_{Sn}-H) due to their lower formation energy compared to isolated V_{Sn}, as shown in Figure 2.24(a). Furthermore, the binding energy of this complexes is quite high of 1.92 eV, which prevents dissociation at high temperature (> 250 °C) and as a result limits the internal redistribution of O with the formation of SnO_2 phase [48]. Thus, the increased concentration of holes in the H doped SnO:H (5-8) sample might be associated with the increased number of V_{Sn} due to the suppressed initial metal content in the film after the addition of H. While an increased amount of H in the film results in the preferential formation of subsequent V_{Sn}-H complexes with acceptor nature due to their low formation energy.

On the other hand, it is well known that V_O are one types of defects in OS with donor-type conductivity, which act as a carrier trap and “hole killers”. We previously reported that H incorporation into the a-IGZO film can reduce the number of V_O in both the near-surface and bulk regions due to preferential H binding to metal, forming the metal-hydrogen bonds (*M-H*) [36]. Lee at al. confirmed the formation of the *Sn-H* bonds by termination of the V_O due to the lower formation energy of the H-V_O complex defect, as shown in Figure 2.24(b)-(c). Thus, p-type SnO film annealing in H containing atmosphere reduced the hole traps and resulted in the improvement

of TFT characteristics [49]. Therefore, despite the increased SnO_2 content, and content of which deteriorates the electrical properties of the p-type conductivity film, the mobility of holes slightly increased due to the V_O elimination effect upon H addition.

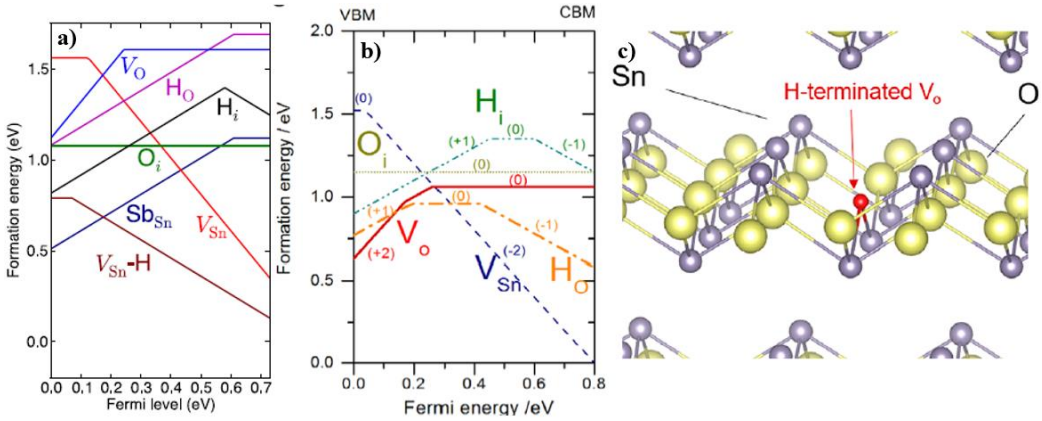

Figure 2.24 (a) and (b) Native defects formation energies in SnO as a function of Fermi level; (c) Oxygen vacancy termination by H and formation of V_O-H complex [48].

2.5.8. SnO_x based TFT fabrication and performance

In order to confirm the p-type conductivity of the SnO_x films the staggered bottom-gate TFTs were fabricated by using a shadow metal mask process. Fabrication process steps and TFT cross layout are shown in Figure 2.25. First, the effect of oxygen ratio on TFT performance was evaluated as a reference based p-type based SnO_x process. SnO_x TFT channel was deposited at $R[O_2]$ of 6%, 8% and 10% since the optimal electrical properties of the films deposited at this condition were observed by Hall measurement. TFT transfer characteristics at V_{DS} = 0.1 V of I_{DS} change at different V_{GS} are shown in Figure 2.26(a)-(b) in linear and log scale, respectively. Thus, I_{DS} increased as SnO_x deposited at higher $R[O_2]$. In addition the field effect mobility also increased and was 1.46 cm^2/ Vs and 2.66 cm^2/Vs for the SnO_x deposited at $R[O_2]$ of 6% and 8%, respectively. These results agree well with the electrical properties of the films after Hall measurements and show a similar trend, where the best performance was found for SnO_x film deposited at 8% oxygen ratio with mobility of holes of 1.65 cm^2/Vs. In contrast, TFT fabricated at $R[O_2]$ of 10% did not show switching properties suggesting p-type conductivity deteriorate due to addition SnO_2 phase development as was previously discussed.

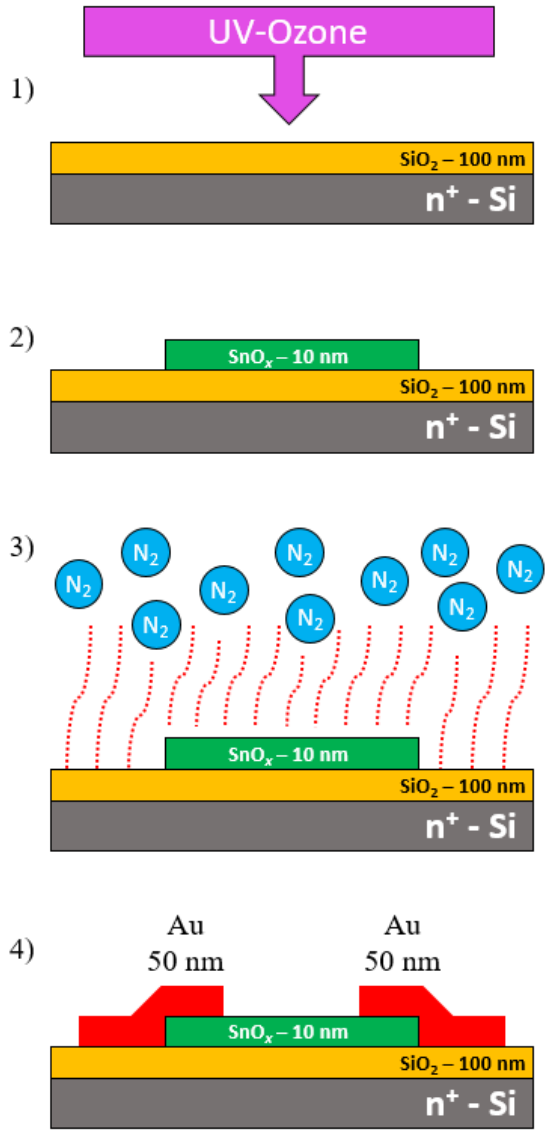

1) Substrate cleaning by DI-water
+
UV-Ozone (O_3) cleaning

2) TFT channel layer formation
DC magnetron sputtering 10 nm thick SnO_x TFT channel deposition using shadow metal mask

3) Crystallization and defect removal
Rapid Thermal Annealing of SnOx in N2 atmosphere for 1 h

4) Source and Drain contacts formation
Thermal evaporation
of 50 nm thick Au in vacuum

Figure 2.25 TFT fabrication process steps with p-type conductivity based on SnO_x films.

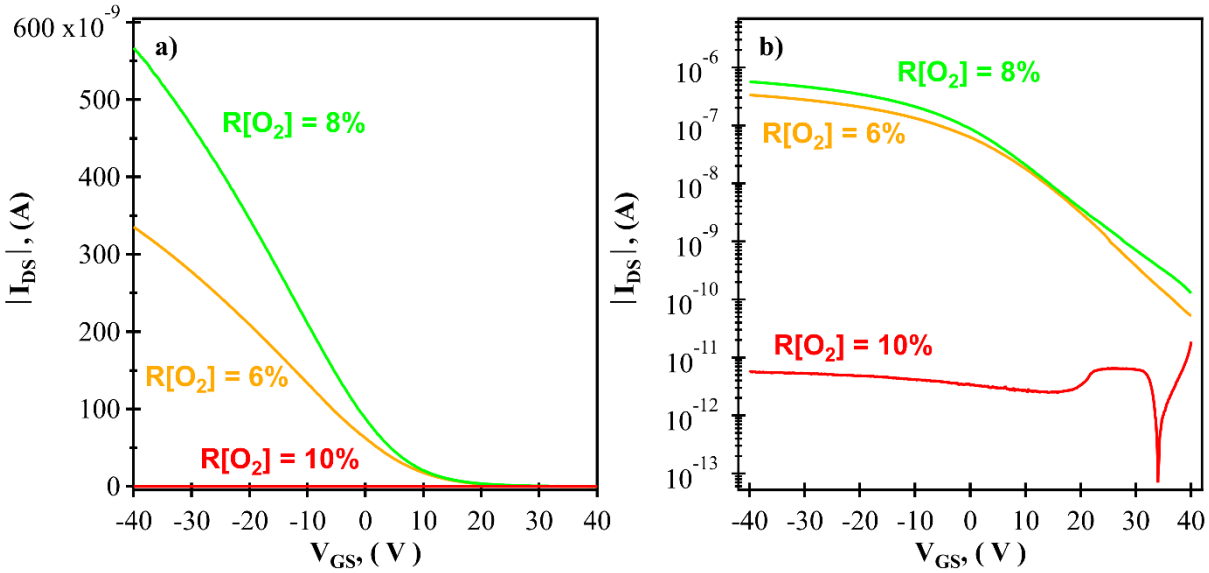

Figure 2.26 Transfer characteristics of SnO_x based TFT (I_{DS} vs V_{GS}) at V_{DS} = 0.1 V and fabricated at different R[O_2]: (a) I_{DS} in linear scale; (b) I_{DS} in log scale.

Next, TFTs with the same structure were fabricated but with H doped SnO_x semiconductor channel. The transfer properties of these TFTs are shown in Figure 2.27. As can be seen, the introduction of hydrogen into the SnO_x film changed the transfer characteristics of the TFT. Thus, the I_{DS} of the TFT deposited at $R[O_2]$ of 6% with the addition of hydrogen of 5% during the sputtering (denoted as TFT 6-5) increased, Figure 2.27(a). In addition, these characteristics, such as I_{on}/I_{off} ratio and subthreshold swing (*S.S.*), were slightly improved than those of a TFT fabricated at higher $R[O_2]$ of 8% but without the addition of hydrogen (TFT 8-0). The field effect mobility of TFT 6-5 was improved and was 2.59 cm^2/Vs compared to TFT 6-0 with 1.46 cm^2/Vs. In contrast, the TFT fabricated at $R[O_2]$ of 8% and with $R[H_2]$ of 5% (TFT 8-5) did not show switching properties and showed similar behaviour as TFT fabricated at $R[O_2]$ of 10% without H adding (TFT 10-0). Thus, it can be argued that the addition of hydrogen to the SnO_x film leads to a shift in the transfer characteristics of the TFT and an improvement in the I_{on}/I_{off} ratio and *S.S.* In addition, these results also indicate and confirm that the addition of hydrogen results in additional oxidation of the Sn and development of the SnO_2 phase. This leads to a deterioration of the TFT performance. In other words, the addition of hydrogen leads to a shift in the performance of the TFT *"as if they were fabricated without hydrogen, but with a higher oxygen ratio"*. These results well agree with the analysis of thin films performed and explained in previous sections.

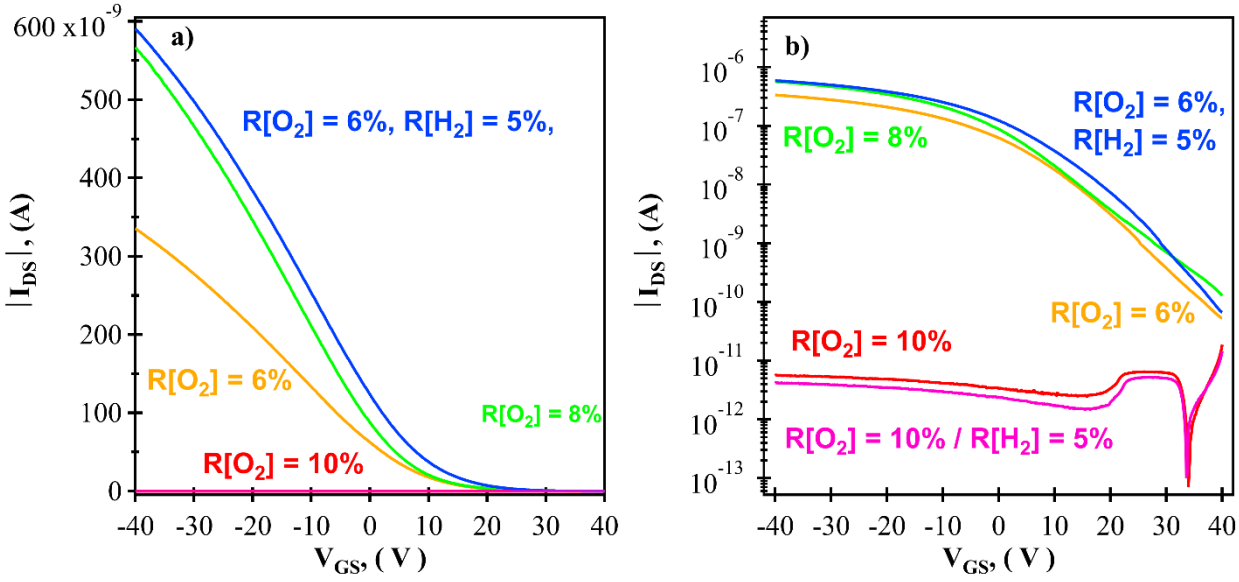

Figure 2.27 Transfer characteristics of H doped SnO_x based TFT at V_{DS} = 0.1 V.

2.6. Conclusion

1. Tin oxide thin films can include up to three different components such as Sn metal, monoxide SnO, and dioxide SnO_2. Each has different electrical, optical, and structural properties. Sn and SnO_2 have n-type conductivity, while only one SnO corresponds and contributes to p-type conductivity of the films. Controlling these components ratio composition in the film strongly affects the resulting film properties and TFT device characteristics. This composition both during film synthesis, by optimizing deposition parameters including the deposition pressure, oxygen content, and base pressure, and during post-treatment, such as annealing atmosphere and temperature, requires careful optimization to obtain quality films with p-type conductivity. In addition, since a sputtered target is metal, therefore the deposition has reactive nature, which is sensitive to O content in the plasma and residual vacuum atmosphere, and that it should be precisely controlled.
2. Deposition process of the SnO_x films has a very narrow process window in order to obtain p-type conductivity behaviour. Thus, SnO_x films deposited at oxygen ratio of 4% and below have metallic appearance, high reflectance, high optical absorption, low transmittance, and very low resistivity due to the dominance of the metal Sn phase in the film. At an oxygen ratio above 10% transition to SnO_2 already takes place due to the strong Sn^{2+} oxidation to Sn^{4+} in oxygen-excess condition. Therefore, the p-type conductivity films can be obtained in oxygen ratio within the range from 4% to 10%. Table 2.9 shows the summarized conditions.

Table 2.10 Narrow deposition process window for SnO_x films with p-type conductivity.

$R[O_2]$, (%)	≤ 4	$4 < X \leq 10$	> 10
Prevailing phase in the film	Metal (Sn)	Monoxide (SnO)	Transition to dioxide (SnO_2)

Deposition pressure, (Pa)	0.4 – 1.0	> 1.0
Prevailing phase in the film	Sn / SnO	SnO_2

3. Density of holes in the SnO_x films is relatively high about ~10^{18} cm^{-3} and their controllability is difficult and limited due to change of oxidation to higher state from Sn^{2+} to Sn^{4+} by deposition at higher R[O_2]. This feature differs from typical n-type conductivity oxide semiconductors materials such as a-IGZO, where the electron density can be successfully controlled by deposition in an oxygen-rich or oxygen-poor environment, thereby eliminating or creating oxygen vacancies in the film structure, respectively.
4. Thermal instability of SnO_x limits the maximum thermal treatment due to internal oxygen redistribution and oxidation to Sn^{4+} resulting in reconfiguration of the crystal structure of SnO_x film and a deterioration in electrical properties. The optimal post-deposition annealing temperature was found from 200 °C to 250 °C, which provides both crystallization of the films to a polycrystalline structure as well as suitable optical and electrical properties.
5. The optimal deposition parameters were found being: R[O_2] = 8%, P_{Dep} = 1.0 Pa with the subsequent post-deposition annealing in N_2 atmosphere for 1 h, with the highest Hall mobility of Hall 1.65 cm^2/Vs and density of holes 5×10^{17} cm^{-3}.
6. Hydrogen doping of SnO_x film resulted in changes of the initial Sn/SnO/SnO_2 phase composition. SnO_x deposition in the H atmosphere suppressed the metal content in the film suggesting additional formation of the tin vacancies, which are the main source of p-type conductivity.
7. Thermal desorption spectroscopy analysis revealed that H adding increased desorption of the H related groups such as OH/H_2O in temperature range from 200 °C to 250 °C. These groups might act as an additional internal oxygen source resulting in oxidation of Sn and undesired SnO_2 phase development. HAXPES analysis confirmed the increased SnO_2 phase in hydrogen-containing SnO_x film by 3% after annealing compared to hydrogen-free SnO.
8. Increased number of V_{Sn} in combination with H addition leads to formation of the $V_{Sn} - H$ complexes with shallow-acceptor nature. These complexes make it possible to compensate for the electrical properties deterioration due to SnO_2 phase development resulting in increased density of holes.

9. In addition, the SnO_x films deposition in the H containing atmosphere leads to V_O termination by H stabilization on V_O site. This substitution results in formation of $Sn - H^+$ bonds, which leads to slight increase in Hall mobility of holes after annealing because of reduction of carrier traps, despite the additional undesirable formation of SnO_2 content in the film. Schematic H mechanism in H doped SnO_x films can be presented as follows:

$$\boldsymbol{SnO_x + H_2\ adding \Rightarrow \begin{cases} \searrow\ Sn \longrightarrow \nearrow\ V_{Sn} \Rightarrow V_{Sn} - H \\ \nearrow\ Sn - OH/H_2O \Rightarrow \nearrow\ SnO_2 \\ Sn - V_O \rightarrow \searrow\ V_O \Rightarrow Sn - H_i^+ \end{cases}}$$

10. The H addition can offer improvements in the properties of p-type SnO_x films, such as transmittance and sub-gap defects reduction, while improvements in basic electrical properties are minor at limited R[H_2] and comparable to those hydrogen-free films. In contrast, the main effect found is the opposite of expectations, leading to additional oxidation and the development of a SnO_2 phase. While the Sn valence control is fundamental to improving the p-type properties.
11. SnO_x-based TFT were fabricated. The transfer characteristics of the TFTs demonstrated and confirmed the p-type conduction of the SnO_x films. In addition, their characteristics showed a similar dependence as the electrical properties of the SnO_x films based on Hall effect measurements. Thus, TFTs based on SnO_x deposited at an oxygen ratio of 6% and 8% showed typical switching performance with the μ_{FE} of 1.46 cm^2/Vs and 2.66 cm^2/Vs, respectively. In contrast, the TFT based on SnO_x deposited at an oxygen ratio of 10% showed no transfer characteristics, which well agrees with the electrical properties of the thin film analysis deposited at the same oxygen ratio of 10% with a μ_{Hall} of 0.3 cm^2/Vs. This confirms the deterioration of the TFT performance due to Sn oxidation in oxygen-excess condition. TFTs fabricated on H doped SnO_x channel showed slight improvements in terms of I_{on}/I_{off} ratio and *S.S.* It can be argued that the addition of H to the SnO_x film leads to a shift in the transfer characteristics. In other words, the incorporation of H into the SnO_x films leads to a shift in the

performance of the TFT *"as if they were fabricated without hydrogen, but with a higher oxygen ratio"*. Nevertheless, carefully optimized synthesis of SnO_x films combined with the addition of a moderate amount of H and annealing at a temperature near or below the stable state of SnO might improve the characteristics of p-type conductivity TFT.

Chapter contribution

Based on this chapter the manuscript titled ***«Investigation of the effect of adding a moderate amount of hydrogen on the properties of tin oxide films deposited by DC magnetron sputtering»***, **Rostislav Velichko**, Yusaku Magari, Hisao Makino, and Mamoru Furuta, Japanese Journal of Applied Physics, 60, 055503 (2021), *https://doi.org/10.35848/1347-4065/abf49d* , was published.

References

1. Kamiya, T.; Hosono, H. Material characteristics and applications of transparent amorphous oxide semiconductors. *NPG Asia Mater.* **2010**, *2*, 15–22, doi:10.1038/asiamat.2010.5.
2. Ide, K.; Nomura, K.; Hosono, H.; Kamiya, T. Electronic Defects in Amorphous Oxide Semiconductors: A Review. *Phys. Status Solidi Appl. Mater. Sci.* **2019**, *216*, 1–28, doi:10.1002/pssa.201800372.
3. K.Nomura, "Fundamental and Recent Progress in p-Channel Oxide-TFT Development (Tutorial)", IMID 2020 International meeting on information display , Invited talk, **2020**, Korea, August 25-28.
4. Khan, S.R.; Kanwal, S.; Bergum, K.; Riise, H.N.; Spectra, A.; Analysis, F. Thin-Film Deposition of Cu_2O by Reactive Radio- Frequency Magnetron Sputtering. **2000**, 37-40.
5. Matsuzaki, K.; Nomura, K.; Yanagi, H.; Kamiya, T.; Hirano, M.; Hosono, H. Epitaxial growth of high mobility Cu2 O thin films and application to p -channel thin film transistor. *Appl. Phys. Lett.* **2008**, *93*, 2–5, doi:10.1063/1.3026539.
6. Fortin, E.; Weichman, F.L. Hall effect and electrical conductivity of Cu_2O monocrystals. *Can. J. Phys.* **1966**, *44*, 1551–1561, doi:10.1139/p66-128.
7. Yao, Z.Q.; Liu, S.L.; Zhang, L.; He, B.; Kumar, A.; Jiang, X.; Zhang, W.J.; Shao, G. Room temperature fabrication of p-channel Cu_2O thin-film transistors on flexible polyethylene terephthalate substrates. *Appl. Phys. Lett.* **2012**, *101*, 1–5, doi:10.1063/1.4739524.
8. Fortunato, E.; Figueiredo, V.; Barquinha, P.; Elamurugu, E.; Barros, R.; Goṇalves, G.; Park, S.H.K.; Hwang, C.S.; Martins, R. Thin-film transistors based on p-type Cu_2O thin films produced at room temperature. *Appl. Phys. Lett.* **2010**, *96*, 2008–2011, doi:10.1063/1.3428434.
9. Dindar, A.; Kim, J.B.; Fuentes-Hernandez, C.; Kippelen, B. Metal-oxide complementary inverters with a vertical geometry fabricated on flexible substrates. *Appl. Phys. Lett.* **2011**, *99*, 1–4, doi:10.1063/1.3656974.
10. Kim, S.Y.; Ahn, C.H.; Lee, J.H.; Kwon, Y.H.; Hwang, S.; Lee, J.Y.; Cho, H.K. P-channel oxide thin film transistors using solution-processed copper oxide. *ACS Appl. Mater. Interfaces* **2013**, *5*, 2417–2421, doi:10.1021/am302251s.
11. Nomura, K.; Kamiya, T.; Hosono, H. Recent progress in oxide based p-channel TFT and complementary inverter, IMID Digest, **2012**, *2*, 8–10.
12. Lany, S.; Osorio-Guillén, J.; Zunger, A. Origins of the doping asymmetry in oxides: Hole doping in NiO versus electron doping in ZnO. *Phys. Rev. B - Condens. Matter Mater. Phys.* **2007**, *75*, 1–4, doi:10.1103/PhysRevB.75.241203.

13. Shimotani, H.; Suzuki, H.; Ueno, K.; Kawasaki, M.; Iwasa, Y. P -type field-effect transistor of NiO with electric double-layer gating. *Appl. Phys. Lett.* **2008**, *92*, doi:10.1063/1.2939006.

14. Xu, W.; Zhang, J.; Li, Y.; Zhang, L.; Chen, L.; Zhu, D.; Cao, P.; Liu, W.; Han, S.; Liu, X.; et al. p-Type transparent amorphous oxide thin-film transistors using low-temperature solution-processed nickel oxide. *J. Alloys Compd.* **2019**, *806*, 40–51, doi:10.1016/j.jallcom.2019.07.108.

15. Mishra, M.K.; Singh, N.; Pandey, V.; Haque, F.Z. Synthesis of SnO_2 Nanoparticles and Its Application in Sensing Ammonia Gas Through Photoluminescence. *J. Adv. Phys.* **2016**, *5*, 8–12, doi:10.1166/jap.2016.1228.

16. Zhao, Q.; Ma, L.; Zhang, Q.; Wang, C.; Xu, X. SnO2-Based Nanomaterials: Synthesis and Application in Lithium-Ion Batteries and Supercapacitors. *J. Nanomater.* **2015**, *2015*, doi:10.1155/2015/850147.

17. Handbook of Transparent Conductors. *Handb. Transparent Conduct.* **2011**, doi:10.1007/978-1-4419-1638-9.

18. Watson, G.W. Origin of the electron distribution in SnO. *J. Chem. Phys.* **2001**, *114*, 758–763, doi:10.1063/1.1331102.

19. Walsh, A.; Watson, G.W. Electronic structures of rocksalt, litharge, and herzenbergite SnO by density functional theory. *Phys. Rev. B - Condens. Matter Mater. Phys.* **2004**, *70*, 1–7, doi:10.1103/PhysRevB.70.235114.

20. Togo, A.; Oba, F.; Tanaka, I.; Tatsumi, K. First-principles calculations of native defects in tin monoxide. *Phys. Rev. B - Condens. Matter Mater. Phys.* **2006**, *74*, 1–8, doi:10.1103/PhysRevB.74.195128.

21. Fortunato, E.; Barquinha, P.; Martins, R. Oxide semiconductor thin-film transistors: A review of recent advances. *Adv. Mater.* **2012**, *24*, 2945–2986, doi:10.1002/adma.201103228.

22. Barquinha, P.; Martins, R.; Pereira, L.; Fortunato, E. *Transparent Oxide Electronics: From Materials to Devices*; 2012; ISBN 9780470683736.

23. Caraveo-Frescas, J.A.; Nayak, P.K.; Al-Jawhari, H.A.; Granato, D.B.; Schwingenschlögl, U.; Alshareef, H.N. Record mobility in transparent p-type tin monoxide films and devices by phase engineering. *ACS Nano* **2013**, *7*, 5160–5167, doi:10.1021/nn400852r.

24. Srinivasan, V.S.S.; Patra, M.K.; Choudhary, V.S.; Mathew, M.; Pandya, A. Phase-change annealing effects on electrical and optical properties of tin oxide thin films. *J. Optoelectron. Adv. Mater.* **2010**, *12*, 1485–1489.

25. Wang, C.M.; Huang, C.C.; Kuo, J.C.; Sahu, D.R.; Huang, J.L. Effect of annealing temperature and oxygen flow in the properties of ion beam sputtered SnO_{2-x} thin films. *Materials (Basel).* **2015**, *8*, 5289–5297, doi:10.3390/ma8085243.

26. Geurts, J.; Rau, S.; Richter, W.; Schmitte, F.J. SnO films and their oxidation to SnO_2: Raman scattering, IR reflectivity and X-ray diffraction studies. *Thin Solid Films* **1984**, *121*, 217–225, doi:10.1016/0040-6090(84)90303-1.

27. Campo, C.M.; Rodríguez, J.E.; Ramírez, A.E. Thermal behaviour of romarchite phase SnO in different atmospheres: a hypothesis about the phase transformation. *Heliyon* **2016**, *2*, 1–13, doi:10.1016/j.heliyon.2016.e00112.

28. Guillén, C.; Herrero, J. P-type SnO thin films prepared by reactive sputtering at high deposition rates. *J. Mater. Sci. Technol.* **2019**, *35*, 1706–1711, doi:10.1016/j.jmst.2019.03.034.

29. Tauc, J. Optical properties and electronic structure of amorphous Ge and Si. *Mater. Res. Bull.* **1968**, *3*, 37–46, doi:10.1016/0025-5408(68)90023-8.

30. Sivaramasubramaniam, R.; Muhamad, M.R.; Radhakrishna, S. Optical Properties of Annealed Tin(II) Oxide in Different Ambients. *Phys. status solidi* **1993**, *136*, 215–222, doi:doi:10.1002/pssa.2211360126.

31. Garzon-Fontecha, A.; De La Cruz, W.; Quevedo, M. Electrical, optical, and structural characterization of p-type N-doped SnO thin films prepared by thermal oxidation of sputtered SnN_x thin films. *Surf. Interface Anal.* **2017**, *49*, 1225–1231, doi:10.1002/sia.6313.

32. Fortunato, E.; Barros, R.; Barquinha, P.; Figueiredo, V.; Park, S.H.K.; Hwang, C.S.; Martins, R. Transparent p-type SnO_x thin film transistors produced by reactive rf magnetron sputtering followed by low temperature annealing. *Appl. Phys. Lett.* **2010**, *97*, 1–4, doi:10.1063/1.3469939.

33. Nomura, K. 39.2: Invited Paper : Recent Progress of Oxide-Semiconductor-Based P -channel TFTs . *SID Symp. Dig. Tech. Pap.* **2015**, *46*, 591–594, doi:10.1002/sdtp.10167.

34. Hsu, P.C.; Tsai, S.P.; Chang, C.H.; Hsu, C.J.; Chen, W.C.; Hsieh, H.H.; Wu, C.C. Preparation of p-type SnO thin films and transistors by sputtering with robust Sn/SnO2 mixed target in hydrogen-containing atmosphere. *Thin Solid Films* **2015**, *585*, 50–56, doi:10.1016/j.tsf.2015.04.034.

35. Aman, S.G.M.; Magari, Y.; Shimpo, K.; Hirota, Y.; Makino, H.; Koretomo, D.; Furuta, M. Low-temperature (150 °C) activation of Ar+O2+H2-sputtered In–Ga–Zn–O for thin-film transistors.

36. Magari, Y.; Aman, S.G.M.; Koretomo, D.; Masuda, K.; Shimpo, K.; Makino, H.; Kimura, M.; Furuta, M. Record-High-Performance Hydrogenated In-Ga-Zn-O Flexible Schottky Diodes. *ACS Appl. Mater. Interfaces* **2020**, doi:10.1021/acsami.0c12638.

37. Ogo, Y.; Hiramatsu, H.; Nomura, K.; Yanagi, H.; Kamiya, T.; Hirano, M.; Hosono, H. P -channel thin-film transistor using p -type oxide semiconductor, SnO. *Appl. Phys. Lett.* **2008**, *93*, 1–4, doi:10.1063/1.2964197.

38. Choi, W.K.; Sung, H.; Kim, K.H.; Cho, J.S.; Choi, S.C.; Jung, H.J.; Koh, S.K.; Lee, C.M.; Jeong, K. Oxidation process from SnO to SnO2. *J. Mater. Sci. Lett.* **1997**, *16*, 1551–1554, doi:10.1023/A:1018547813759.

39. Toyama, T.; Seo, Y.; Konishi, T.; Okamoto, H.; Tsutsumi, Y. Physical properties of p-type tin monoxide films deposited at low temperature by radio frequency magnetron sputtering. *Appl. Phys. Express* **2011**, *4*, doi:10.1143/APEX.4.071101.

40. Jang, D.M.; Jung, H.; Hoa, N.D.; Kim, D.; Hong, S.K.; Kim, H. Tin oxide-carbon nanotube composite for NO_X sensing. *J. Nanosci. Nanotechnol.* **2012**, *12*, 1425–1428, doi:10.1166/jnn.2012.4656.

41. Akgul, F.A.; Gumus, C.; Er, A.O.; Farha, A.H.; Akgul, G.; Ufuktepe, Y.; Liu, Z. Structural and electronic properties of SnO_2. *J. Alloys Compd.* **2013**, *579*, 50–56, doi:10.1016/j.jallcom.2013.05.057.

42. Ni, Q.; Kirk, D.W.; Thorpe, S.J. Characterization of the Mixed Oxide Layer Structure of the Ti/SnO 2 -Sb 2 O 5 Anode by Photoelectron Spectroscopy and Impedance Spectroscopy . *J. Electrochem. Soc.* **2015**, *162*, H40–H46, doi:10.1149/2.0681501jes.

43. Kwoka, M.; Krzywiecki, M. Impact of air exposure and annealing on the chemical and electronic properties of the surface of SnO_2 nanolayers deposited by rheotaxial growth and vacuum oxidation. *Beilstein J. Nanotechnol.* **2017**, *8*, 514–521, doi:10.3762/bjnano.8.55.

44. Luo, H.; Liang, L.Y.; Cao, H.T.; Liu, Z.M.; Zhuge, F. Structural, chemical, optical, and electrical evolution of SnO_x films deposited by reactive rf magnetron sputtering. *ACS Appl. Mater. Interfaces* **2012**, *4*, 5673–5677, doi:10.1021/am301601s.

45. Kwoka, M.; Ottaviano, L.; Passacantando, M.; Santucci, S.; Czempik, G.; Szuber, J. XPS study of the surface chemistry of L-CVD SnO_2 thin films after oxidation. *Thin Solid Films* **2005**, *490*, 36–42, doi:10.1016/j.tsf.2005.04.014.

46. Pan, X.Q.; Fu, L. Oxidation and phase transitions of epitaxial tin oxide thin films on (1012) sapphire. *J. Appl. Phys.* **2001**, *89*, 6048–6055, doi:10.1063/1.1368865.

47. Shih, C.W.; Chin, A.; Lu, C.F.; Su, W.F. Remarkably High Hole Mobility Metal-Oxide Thin-Film Transistors. *Sci. Rep.* **2018**, *8*, 1–6, doi:10.1038/s41598-017-17066-x.

48. Varley, J.B.; Schleife, A.; Janotti, A.; Van De Walle, C.G. Ambipolar doping in SnO. *Appl. Phys. Lett.* **2013**, *103*, doi:10.1063/1.4819068.

49. Lee, A.W.; Le, D.; Matsuzaki, K.; Nomura, K. Hydrogen-Defect Termination in SnO for p-Channel TFTs. *ACS Appl. Electron. Mater.* **2020**, *2*, 1162–1168, doi:10.1021/acsaelm.0c00149.

Chapter 3

Low-temperature activation mechanism in Hydrogen-doped In-Ga-Zn-O films for flexible device applications

Synthesis of a–IGZO films is always accompanied by the formation of various defects. These defects should be properly mitigated during post-processing in order to achieve quality films and high performance devices. The most common treatment method for a–IGZO is post-deposition annealing at 300 °C. However, this thermal treatment at such temperature is not suitable for flexible devices or wearable electronics, whose processing temperature is limited due to polymer substrate utilization. Low–temperature activation process is a key approach for OS materials utilization in flexible devices and wearable electronics. We reported that H adding during the IGZO deposition reduces the activation temperature to 150 °C, demonstrating a strong potential of this method. However, the mechanism upon H adding causing low–temperature activation has not been investigated and clarified in detail.

In this chapter, we focused on the mechanism of the H adding during the IGZO films synthesis resulting in the carrier density control and defects passivation after low–temperature activation. Thus, it was found the higher the H content the greater the O diffusion and the larger the shift of the diffusion starting point toward a lower temperature. Diffusion starting point shifted from 190 °C to 90 °C toward higher H content due to the induced structural change facilitating the O diffusion. HAXPES analysis revealed the near Fermi level defects reduction for H doped IGZO films after the 150 °C annealing. These states were comparable with the hydrogen free IGZO states after 300 °C annealing. These results demonstrate the strong potential of H utilization during the synthesis process of the IGZO making it possible for utilization for low–temperature process applications such as flexible devices and transparent electronics.

3.1. Introduction

The material design concept of amorphous oxide semiconductors (AOS) with large electron mobility was proposed more than two decades ago [1]. Later, this concept was successfully implemented, demonstrating the strong potential of using AOS with mobility 10 cm^2/Vs as an alternative to hydrogenated amorphous silicon (a:Si-H) mobility of which does not exceed 1 cm^2/Vs [2]. This caused an active boost for the subsequent research and development of AOS such as InGaZnO (IGZO), InGaO (IGO), GaZnO (GZO), InZnO (IZO), InSnZnO (ITZO), ZnSnO (ZTO) and others for various application [3–5]. They possess the key advantages, which include high electron mobility (> 10 cm^2/Vs) and high transparency, suitability for low temperature processes making it possible to use for flexible and transparent electronics, industrial friendly scalability due to high uniformity and large area deposition at room temperature [6–8]. The pioneer representative of AOS is IGZO, and extensive research has been carried out to investigate electrical properties, generation of defects [9], and methods for improving synthesis and optimization. In addition, IGZO is the first successfully commercialized oxide semiconductor for thin-film transistors (TFTs) at the industrial level [10].

Nevertheless, the synthesis of IGZO is always accompanied by the formation of various defects. For instance, the typical defects in AOS are interstitial and weakly bonded oxygen, and well-known oxygen vacancies (V_O) with donor-type conductivity, and which act as a carrier trap resulting in negative bias illumination stress (NBIS) [11–13]. Defects formation is caused both by the process parameters (base pressure, oxygen content, deposition pressure, and others) and by the synthesis method itself. One of the most common synthesis techniques is a sputtering deposition in a vacuum, containing high energy plasma species such as O ions or reflected Ar ions, after interacting with the target material. These defects affect not only the film properties, but also the TFT performance. Therefore, they should be properly mitigated during post-processing in order to achieve quality films and, as a result, high performance devices. The most common treatment method for a-IGZO is thermal annealing at 300 °C [14]. However, thermal treatment at such temperatures is not suitable for flexible devices or wearable electronic applications, which have

a limited processing temperature due to the use of polymer substrate. This limitation requires the development of new approaches to achieve comparable electrical properties at a relatively low-temperature. Several methods have already been proposed (these methods are referred to as "activation process of IGZO"), such as active IGZO layer oxidation at low temperatures by O_2 wet and O_3 annealing [15,16], high-pressure O_2 and N_2 gas annealing [17], hydrogen injection and oxidation for low-temperature aqueous solution-processed IGZO TFT [18], microwave and e-beam annealing [19], capacitive coupled plasma-assistant IGZO magnetron sputtering [20], mechanochemical and thermal treatment [21]. Our research group has recently reported that adding hydrogen to the sputtering atmosphere can effectively reduce the activation temperature of IGZO films [22–24]. Table 3.1 shows the recent progress in different activation methods and the obtained TFT mobility.

Table 3.1 Low-temperature activation methods of a-IGZO and TFT mobility.

Activation method	Temperature (°C)	TFT mobility (cm^2/Vs)	References
O_2 wet annealing	150	5.0	[15]
O_3 annealing	≤ 250	11.4	[16]
High-pressure annealing in O_2	100	10.6	[17]
Hydrogen injection and oxidation	250	3.8	[18]
Microwave and e-beam annealing	Room	8.1 / 11.2	[19]
Capacitive coupled plasma-assistant magnetron sputtering	100	26.0	[20]
Mechanochemical treatment	200	12.81	[21]
Ar + O_2 + H_2 magnetron sputtering	150	13.4 – 18.9	[22–24]

Hydrogen is one of the most common impurities and can be found in all deposition apparatus. Many experimental and theoretical studies have been conducted to better understand the role of H in OS. It is known that H results in an increased carrier density (N_e) in ZnO and IGZO due to its shallow donor behaviour [25,26]. Miyase et al. reported that the typical H content in IGZO film deposited by standard vacuum equipment is 10^{20} cm^{-3}. The authors concluded favourable and unfavourable effects on TFT performance [27]. First principle calculations revealed that H upshifts the Fermi-level and therefore increases the electrical conductivity of IGZO [28].

On the other hand, the incorporation of H into the IGZO film suppresses the metal-metal (*M-M*) related defects near the conduction band minimum (CBM) by forming metal-hydrogen (*M-H*) bonds [29]. Moreover, the formation of *M-H* bonds occurs by H stabilization at the V_O site. The electron take-off angle dependence performed by hard X-ray photoelectron spectroscopy (HAX-PES) showed the V_O reduction in bulk and near-surface regions due to the H binding to the metal [30]. Thus, the addition of H can be considered as an effective method of V_O reduction in IGZO film, resulting in improved device stability [31]. According to several reports, incorporating H into the film is not only limited by IGZO synthesis process but it should also be considered within the TFT fabrication process. It was shown that H can diffuse from the passivation layer, such as SiO_x etch-stopper, or from the Al_2O_3 gate insulator layer, to the IGZO channel, and that this diffusion leads to an improvement in TFT transfer characteristic [32,33]. Nomura et al. evaluated H diffusion into a non-hydrogenated a-IGZO film. The authors reported that H can diffuse at a depth of up to 200 nm even at relatively low annealing temperatures [34]. Despite these extensive studies into the H effects, the mechanism of low-temperature activation for H doped IGZO films remains unclear.

We previously reported that H addition led to a drastic N_e decrease after the annealing at relatively low-temperature of 150 °C [22]. However, an explanation of the causes leading to low-temperature activation has not been clarified yet. In this study, we focused on elucidating the mechanism causing low-temperature activation in H doped IGZO films. *In-situ* Hall measurements performed in both air and vacuum showed the importance of the O in the annealing atmosphere to control carrier density and promote defect repair through O diffusion. Incorporation of H into the IGZO film decreased the starting temperature of O diffusion into the film with an increase of the H content in the film. The near Fermi level defects of H doped IGZO film analyzed by hard X-ray photoelectron spectroscopy decreased after annealing at 150 °C and were comparable to that of conventional IGZO film annealed at 300 °C. Finally, the X-ray reflectometry (XRR) analysis revealed a decrease in the film density after incorporation of H.

3.2. Hydrogen-containing IGZO deposition conditions

In order to investigate the H mechanism, we deposited 50-nm-thick IGZO films on a 100 mm diameter glass substrate by DC magnetron sputtering in $Ar/O_2/H_2$ gas mixture with a total gal flow of 30 sccm using ceramic $InGaZnO_4$ (atomic ratio of In:Ga:Zn = 1:1:1) target at room temperature. The O_2 and H_2 gas ratios were defined as $R[O_2] = O_2/(Ar+O_2+H_2)$ and $R[H_2] = H_2/(Ar+O_2+H_2)$, respectively. Since it is known that the typical H content in hydrogen-free films is about 10^{20} cm^{-3}, in order to minimize the influence of extraneous side effects, namely influence of water from the atmosphere and residual H content after deposition, the load lock and main chamber were pumped out to a back pressure below 1×10^{-5} Pa and 5×10^{-5} Pa prior to each deposition, respectively. In addition, before each deposition, the IGZO target surface was properly conditioned using a pre-sputtering process on a dummy wafer for 40 minutes at each $R[H_2]$, and therefore to achieve a stable and reliable deposition environment. The $R[O_2]$ was fixed at 1% for both the hydrogen-free and the hydrogen-containing IGZO films, while $R[H_2]$ was varied from 0% to 8%. The DC power, deposition pressure and distance from the target to the substrate were 80 W (power density - 0.99 W/cm^2), 1.0 Pa and 82 mm, respectively. All films were annealed in air using a hot-plate for 1 h. The annealing temperature was varied from 100 °C to 250 °C. Deposition parameters of IGZO:H films are summarized in Table 3.2.

Table 3.2 Deposition parameters of the H doped IGZO films.

Target	100 mm InGaZnO [In : Ga : Zn = 1 : 1 :1 atom %]
Substrate	100 mm glass
Film thickness (nm)	50
Deposition time (min)	3′ 15″
Load lock pressure (Pa)	$< 1\times10^{-5}$
Base pressure (Pa)	$\sim5\times10^{-5}$
Deposition pressure (Pa)	1.0 Pa
DC power (W)	80
Total gas flow ($Ar+O_2+H_2$) (sccm)	30
Deposition temperature (°C)	RT
$R[O_2] = O_2 / (Ar+O_2+H_2)$ (%)	1
$R[H_2] = H_2 / (Ar+O_2+H_2)$ (%)	0 – 8
Substrate to target distance	82 mm

3.3. Hydrogen effect on electrical properties of IGZO films

The electrical properties were measured by the AC/DC Hall Effect Measurement system using van der Pauw geometry (Toyo corp., ResiTest 8403). A set of four square 7 mm × 7 mm samples dimension was prepared and measured to obtain accurate and reliable results. Next, the average value of each independent set of the samples was calculated and used for analysis. In addition, the excitation current during Hall measurement was individually set up for every set of samples due to the different electrical properties of the film. Thus, it allowed the Hall voltage to be maintained at about 1 mV, and as a result kept the signal to noise ratio at the same level, additionally improving the measurement accuracy.

Electrical properties of the IGZO films deposited at various R[H_2] and at fixed R[O_2] of 1% were analyzed. Figure 3.1 shows the electron concentration (N_e) and Hall mobility as a function of R[H_2] of the as-deposited and annealed films at different temperatures in the air atmosphere for 1 h. It can be seen, as R[H_2] increased the N_e of as-deposited films increased significantly by three orders of magnitude from 4.3×10^{16} cm^{-3} to 3.1×10^{19} cm^{-3}. This is in agreement with previous reports due to the shallow donor nature of H in oxide semiconductors [35,36]. The transition point at 200 °C for hydrogen-free IGZO was clearly observed.

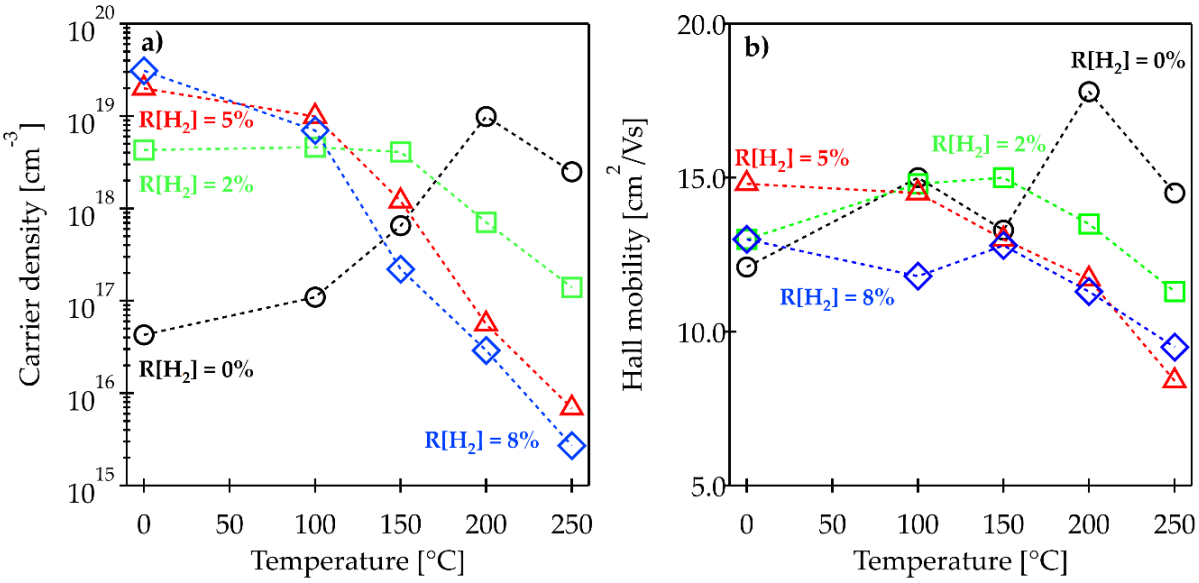

Figure 3.1 Electrical properties of IGZO films deposited at various R[H_2] and at fixed R[O_2] as a function of annealing temperature: (a) carrier density; (b) Hall effect mobility.

The N_e for this film was 2.5×10^{18} cm^{-3} after annealing at 250 °C indicating the insufficient temperature for defects termination and N_e recovery. In contrast, hydrogen-containing IGZO films showed the opposite behavior, namely the N_e drastically decreased after annealing at temperature of 250 °C being 1.4×10^{17} cm^{-3}, 6.9×10^{15} cm^{-3} and 2.7×10^{15} cm^{-3} for $R[H_2]$ = 2%, 5% and 8%, respectively. These N_e values are suitable and highly desirable for TFT application. In addition, it can be seen that the decreasing point of the N_e is specific and correlates with $R[H_2]$. This point shifted toward a lower annealing temperature for higher $R[H_2]$ being 200 °C, 150 °C, 100 °C and below 100 °C for 0%, 2%, 5% and 8% of $R[H_2]$, respectively. Thus, the causes for such change and decrease in the carrier density in the low-temperature range deserve further detailed analysis and consideration.

3.4. Conventional IGZO films

In order to investigate the cause of the observed carrier density variation upon H incorporation the *in-situ* Hall measurement was performed. The measurement program performed the following three actions. First, the sample was heated to a target temperature. Then it was allowed to stand for 5 minutes in order to stabilize the sample temperature, after which time the measurement was taken. These actions were performed on target temperatures in the range from 40 °C to 300 °C at 10 °C intervals. Schematic measurement algorithm of the *in-situ* Hall measurement program is shown in Figure 3.2. It was necessary to define the excitation current and AC/DC measurement mode at a specific temperature range due to continuous variation of the N_e during the heating in the air before the *in-situ* Hall measurements were taken. Detailed parameters of the *in-situ* Hall measurement are shown in Table 3.3. For the vacuum measurements, the chamber with the sample inside was properly evacuated with a rotary pump to a base pressure < 0.4 Pa. In addition, measurements were started after 60 minutes of waiting time to stabilize and minimize the effect of the residual atmosphere.

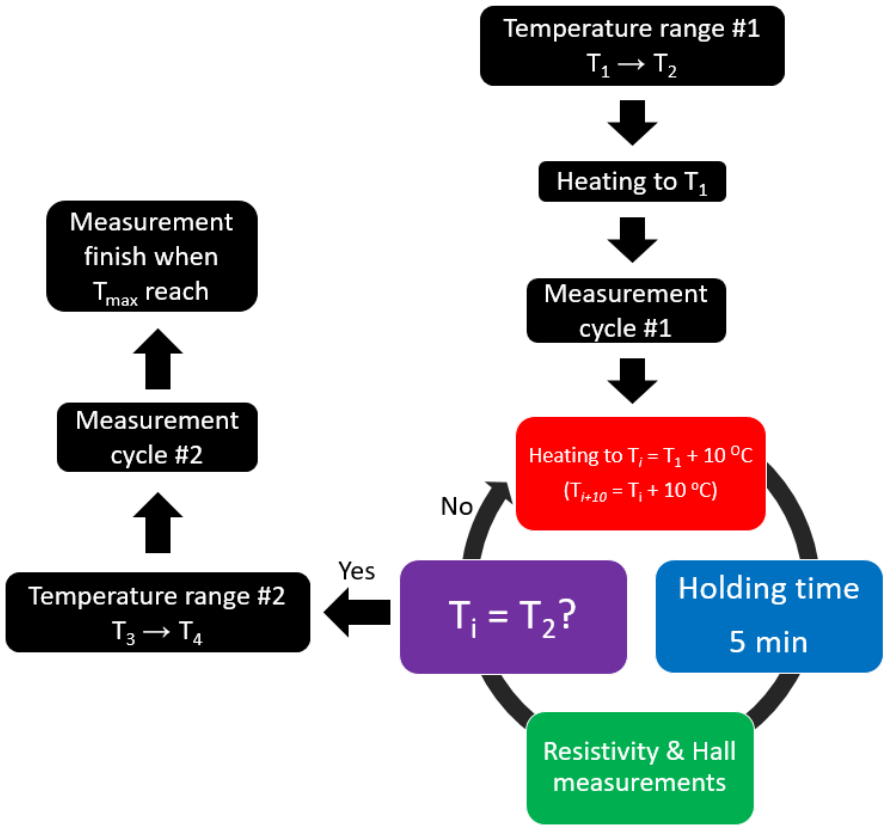

Figure 3.2 Schematic algorithm of the *in-situ* Hall measurement program.

Table 3.3. *In-situ* Hall measurement parameters used for analysis of the conventional and hydrogen-containing IGZO films performed in the air atmosphere.

R[H_2] (%)	Temperature range (°C)	Excitation current	Hall mode
0	40 – 110	100 nA	AC
	120 – 150	10 μA	
	160 – 200	50 μA	
	210 – 250	300 μA	DC
	260 – 300	50 μA	

Figure 3.3(a) shows the changes of carrier density (N_e) in conventional IGZO film, which was deposited by sputtering in Ar/O_2 gases, as a function of stage temperature measured by *in-situ* Hall measurement in vacuum and ambient air. Before stage heating, the N_e in air was slightly higher than that in vacuum due to H_2O absorption of the films surface, and the N_e did not change significantly from the initial values up to the stage temperature (T_s) of 100 °C. When T_s exceeded 100 °C, the N_e significantly increased, but exhibited almost the same values between air and vacuum annealing up to T_s of 230 °C. The N_e continuously increased for vacuum annealing, whereas N_e was found to decrease for air annealing as T_s increased more than 240 °C. The main difference

between the air and vacuum measurements was observed at the T_s of > 240 °C. Thus, the change in the N_e upon thermal processing can be separated into three main steps: (i) surface desorption of O at a low temperature range (< 100 °C) [34], (ii) defect generation due to the desorption of O related species, such as H_2O or O_2 (> 100 °C) [37], (iii) the N_e recovery due to the defect repair promotion by O diffusion and subsequent oxidation at a high-temperature range (> 240 °C), since the N_e continued to increase for vacuum annealing.

This result indicates the importance of oxygen in annealing atmosphere to effectively control the carrier density. Oxygen diffusion into the film and subsequent oxidation would be occurred at the T_s of > 240 °C. The Hall mobility varied from 2 to 18 cm^2/Vs depending on the N_e, which is consistent with previous reports and explained by the percolation conduction model of carrier transport in oxide semiconductors [7,38].

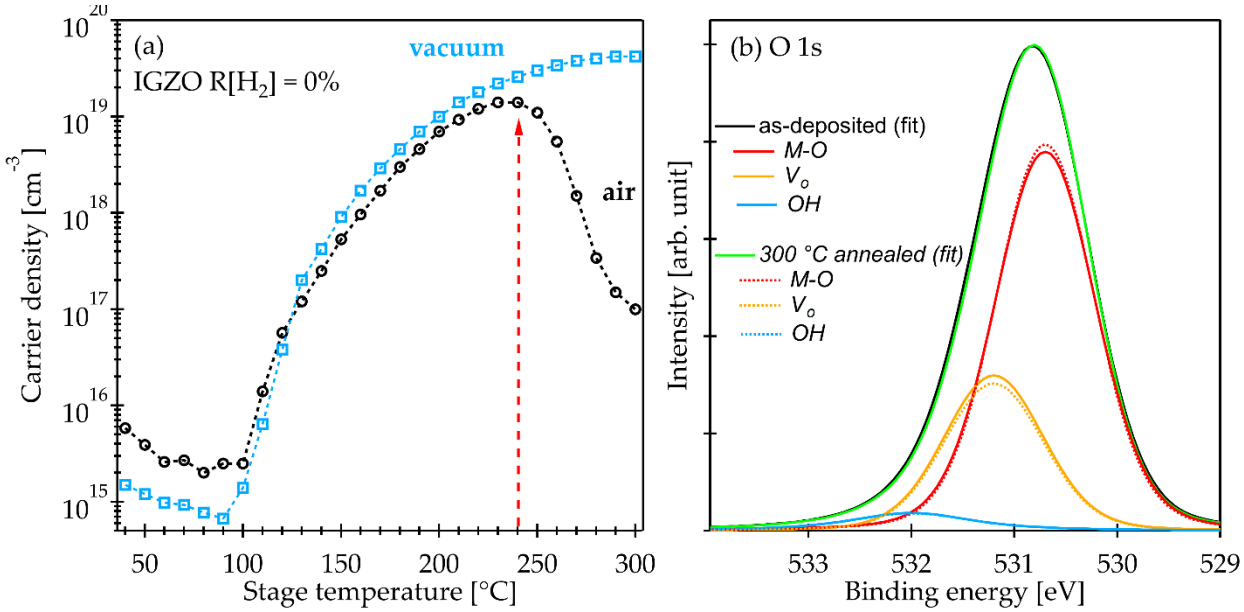

Figure 3.3. Properties of conventional IGZO film: (a) carrier density obtained during the *in-situ* Hall measurement in air and vacuum; (b) O 1s spectra before and after 1 h annealing in air.

Figure 3.3(b) shows the HAXPES O 1s core spectra of conventional IGZO film before and after air annealing at 300 °C. A slight difference in the shape of the peaks before and after annealing was found in the higher binding energy region. Three clear distinguishable Gaussian–Lorentzian curves after the O 1s spectra deconvolution were assigned to 530.7 eV, 531.2 eV, and 532.0 eV, corresponding to the metal-oxygen bonds (*M-O*), oxygen vacancies (V_O), and oxygen-

hydrogen (*OH*), respectively [21,39,40]. Table 3.4 is a summary of the relative area ratio of the obtained peaks. Relative area ratio of the V_O decreased after air annealing, while that of the *M-O* increased. Carrier density variation in an IGZO film is predominantly attributed to V_O generation and termination in the film [11,41,42]. Therefore, the N_e variation observed in Figure 3.3(a) during the *in-situ* Hall measurement suggests that the O diffusion effectively reduces the V_O.

Table 3.4 Relative area ratio of the metal-oxygen (*M-O*), oxygen vacancies (V_O), and oxygen-hydrogen (*OH*) of the conventional IGZO film before and after annealing in air for 1 h after deconvolution of O 1s spectra.

Temperature	*M-O (%)*	V_O (%)	*OH* (%)
as-deposited	67.70	27.35	4.95
T_{ann} = 300 °C	68.63	26.42	4.95

Figure 3.4 shows the valence band configuration from Fermi energy (E_F). Differences in the near-valence band maximum (near-VBM) and the near-conduction band minimum (near-CBM) (i.e. near Fermi level defects) states were clearly observed. The near-VBM states decreased with an increase of annealing temperature. On the other hand, although the near E_F defects did not change after annealing at 150 °C, these were decreased by annealing at 300 °C.

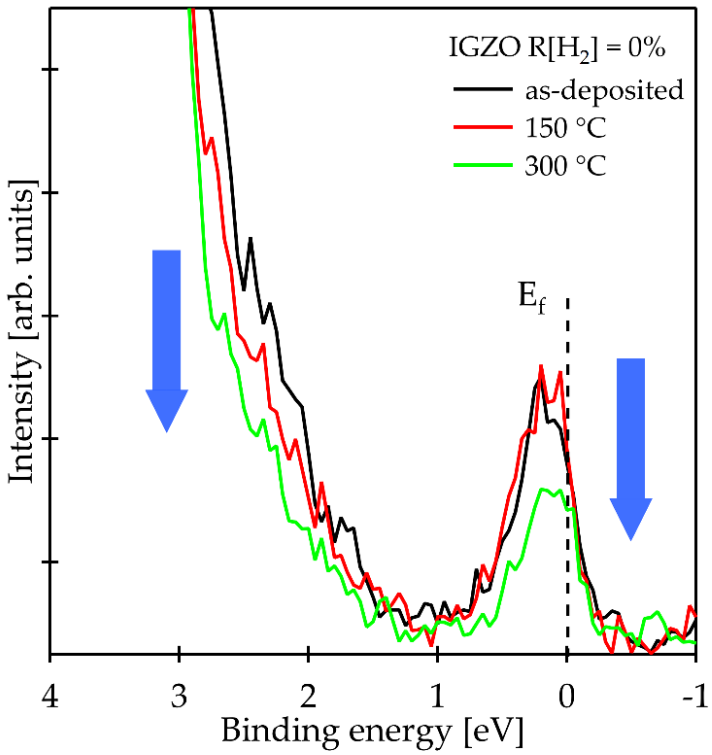

Figure 3.4. Electronic structure of IGZO films around the band gap region of as-deposited and after annealing at various temperature.

We previously reported that transfer characteristics of the TFT with conventional IGZO channel significantly improved after 300 °C annealing in air. Thus, the near E_F defects strongly influence the electrical properties of the IGZO TFTs. Furthermore, the required annealing temperature to obtain good electrical properties and reliability for the IGZO TFTs is typically 300 °C [14,43]. Based on the *in-situ* Hall measurement and HAXPES analysis results, air annealing at T_S of > 240 °C effectively promotes an active diffusion of O into the film, resulting in a marked reduction of both the V_O and near E_F defects. In other words, the O diffusion into the film during annealing plays an important role for reducing V_O and subgap states near E_F.

3.5. Hydrogen-doped IGZO films

3.5.1. Enhanced oxygen diffusion at low-temperature

Hereafter, we will focus on the properties of hydrogen-doped IGZO films (IGZO:H), which were deposited by sputtering in $Ar/O_2/H_2$ gases, to discuss the mechanism for low-temperature activation of the IGZO:H TFTs. Figure 3.5 shows the *in-situ* Hall measurement results of the N_e in the IGZO:H films deposited with $R[H_2]$ of (a) 2%, (b) 5%, and (c) 8%. The N_e of the as-deposited IGZO:H films increased with an increase of the $R[H_2]$ since hydrogen acts as a shallow donor in an IGZO film. All films showed the similar N_e values in low-temperature region between air and vacuum annealing; however, the clear difference in the N_e was observed between air and vacuum annealing when T_s increased. The critical temperature, at which the N_e in air annealing started to decrease, was found at approximately 190 °C for the film with $R[H_2]$ of 2 %, and gradually intensifies only at a higher temperature treatment. This temperature was lower than the value (240 °C) observed from conventional IGZO film as shown in Figure 3.3(a). On the other hand, the annealing temperature of 150 °C for $R\ [H_2]$ = 5% is at an intermediate state, since O diffusion is only at the initial stage and an effective decrease in the N_e can be achieved after prolonged annealing, as shown in Figure 3.6(a). While for $R[H_2]$ of 8%, the 150 °C temperature is the optimal condition in terms of a trade-off between the time and temperature due to the active O diffusion, which begins at approximately 100 °C.

As was previously discussed, the critical temperature is correlated with the predominant O diffusion process in the film. Thus, *in-situ* Hall measurement results clearly indicated that the critical temperature, at which the O diffusion starts in the film, could be reduced by hydrogen doping in the IGZO. Furthermore, the starting temperature of O diffusion into the film decreased with an increase of the hydrogen content in the film.

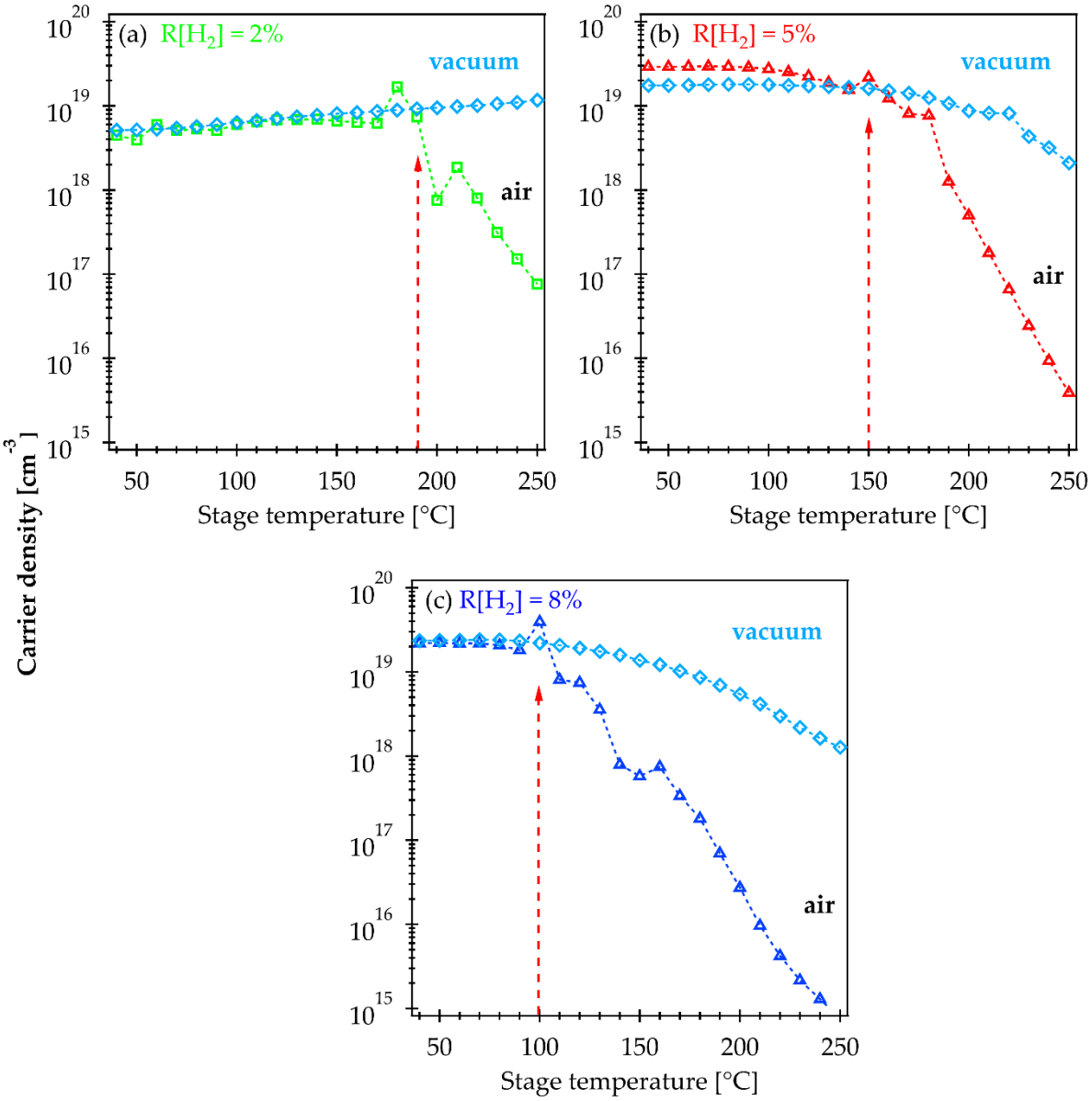

Figure 3.5 Carrier density of H doped IGZO films obtained from the *in-situ* Hall measurement performed in air and vacuum atmosphere: (a) $R[H_2]$ = 2%; (b) $R[H_2]$ = 5%; (c) $R[H_2]$ = 8%.

However, in Figure 3.5(b)-3.5(c) a slight N_e decrease by one order for measurement in vacuum was observed for the IGZO films deposited at $R[H_2]$ = 5% and 8%. This N_e reduction in

vacuum at higher temperature range can be attributed to the several possible reasons, namely desorption of weakly bonded H, defects repair through internal uncoordinated O, weak O diffusion into the film originating from the imperfection of vacuum formed by only a rotary pump, and desorption of the absorbed species on the measurement chamber interior during the heating. It additionally supports the idea of the enhanced O diffusion for IGZO:H films at low temperature because the N_e of the R[H_2] =2% film remained stable within the whole temperature range. The *in-situ* Hall measurement parameters for IGZO:H films presented in Table 3.5.

Table 3.5 *In-situ* Hall measurement parameters used for analysis of the conventional and hydrogen-doped IGZO films performed in the air atmosphere.

R[H_2] (%)	Temperature range (°C)	Excitation current	Hall mode
2	40 – 60	100 μA	DC
	70 – 100	20 μA	
	110 – 150	5 μA	
	160 – 200	1 μA	
	210 – 250	500 nA	
5	40 – 100	1 mA	DC
	110 – 180	10 μA	
	190 – 250	300 nA	AC
8	40 – 90	1 mA	DC
	100 - 130	1 μA	AC
	140 – 200	20 nA	
	210 - 250	5 nA	

Next, the annealing time influence on the N_e at a temperature of 150 °C for different R[H_2] annealed in different atmospheres since this temperature can effectively activate the IGZO:H TFTs with good electrical properties and reliability as we reported, was analyzed. Figure 3.6(a) shows the N_e change after annealing for 15 min, 30 min, 60 min, 120 min and 240 min at 150 °C in air. The minor change in the N_e about 10^{18} cm^{-3} was observed within the whole range of the annealing time for the film deposited at R[H_2] =2%. On the other hand, the N_e for the films with high H content declined sharply within the annealing less than 60 min. It can be seen that the N_e is comparable for both 5% and 8% of R[H_2], but the required annealing time to reach the 5×10^{17} cm^{-3} for R[H_2] = 8% film was 30 min, while for R[H_2] =5% it required 120 min.

Furthermore, an initial slope of the N_e decrease was much larger for the film with R[H_2] of 8 % than that with 5%, suggesting higher oxygen diffusion coefficient for the film with R[H_2] of 8 %.

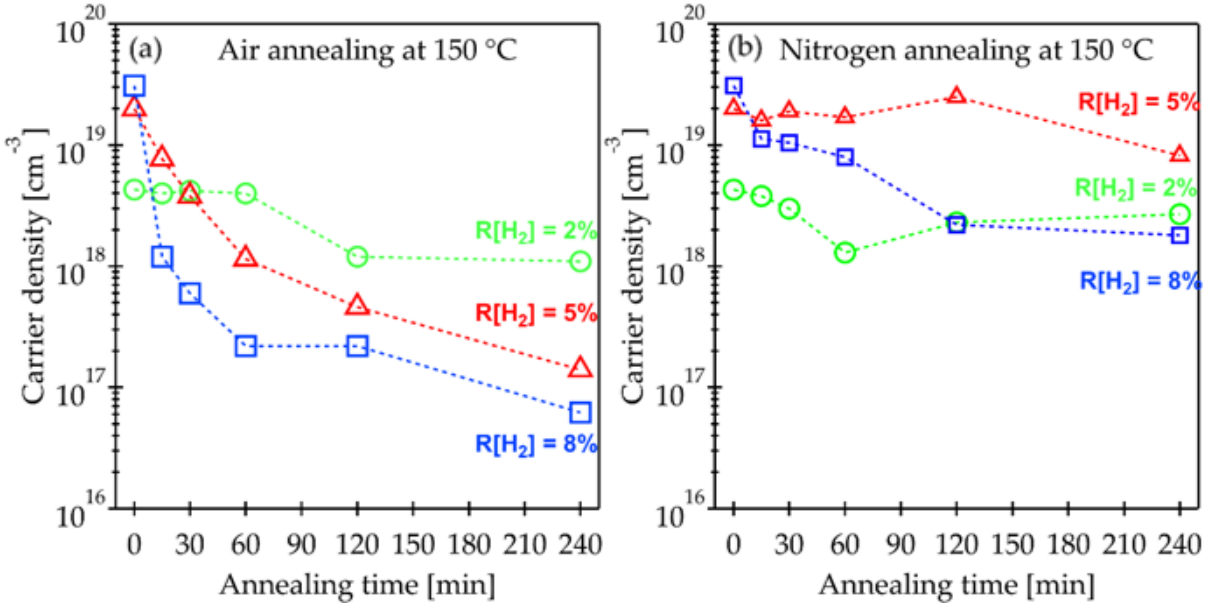

Figure 3.6 Annealing time dependence of the N_e for H containing IGZO films after annealing at 150 °C: (a) in Air; (b) in N_2 atmosphere.

In contrast, Figure 3.6(b) shows the N_e after annealing in the N_2 atmosphere. For the annealing in N_2 all films were annealed by a rapid thermal annealing furnace. The annealing chamber was continuously purged with N_2 at a constant flow of 500 mL/min for 20 minutes in order to minimize the influence of the residual atmosphere on the carrier density. After one hour annealing, the sample was cooled to room temperature with the same N_2 flow, and only then extracted for further analysis. The N_e did not significantly change in the whole annealing time range being at relatively high level $10^{18} - 10^{19}$ cm^{-3} for all R[H_2]. It should be noticed that some N_e reduction was observed for R[H_2] = 8% after 120 min and 240 min annealing in N_2.

These results indicate the importance of O presence in annealing atmosphere to effectively control the carrier density. The carrier density in IGZO is predominantly attributed to V_O generation and termination in the film [11,41,42]. Thus, such a significant difference in the carrier density of the H doped IGZO films after annealing in air suggests that the O diffusion into the film effectively reduced the V_O at low temperature. Furthermore, diffusion was enhanced for higher R[H_2] resulting in sharp N_e drop even after 15 min annealing.

3.5.2. Subgap defects reduction through O diffusion

Chemical bonding states and subgap states of the IGZO:H films. Figures 3.7(a) and 3.7(b) show the HAXPES O 1s core spectra of the IGZO:H film deposited at R[H_2] of 8% along with conventional IGZO before and after annealing, respectively. In Figure 3.7(b), the 300 °C annealed conventional IGZO and the 150 °C-annealed IGZO:H films were compared. A noticeable difference as a shoulder in the higher binding energy region was observed for the IGZO:H film both before and after annealing, as can be seen in Figure 3.7(a)-3.7(b), respectively. All peaks were similarly fitted by three Gaussian–Lorentzian curves corresponding to the *M-O*, V_O and *OH*. For the as-deposited films, the relative area ratio of *OH* bonds significantly increased from 4.95% for the conventional IGZO film to 12.63% for the IGZO:H film due to an incorporation of hydrogen into the film. On the other hand, that of V_O in the as-deposited IGZO:H film was 26.08%, which is slightly less than that of the conventional as-deposited IGZO film (27.35%). This suggests that the termination of the V_O occurred even during the deposition process in a H containing atmosphere. The area ratio of V_O in the IGZO:H film further decreased after annealing at 150 °C to 25.08%, which is lower than that in the conventional IGZO film after annealing at 300 °C. Relative area ratios of the IGZO and IGZO:H films are summarized in Table 3.6. Note that the oxygen diffusion into the IGZO:H film deposited at R[H_2] of 8% was observed at a temperature more than 100 °C as shown in Figure 3.6(c).

Table 3.6 Relative area ratio of the metal-oxygen (*M-O),* oxygen vacancies (V_O), and oxygen-hydrogen (*OH*) in the IGZO and IGZO:H films before and after annealing in air for 1 h after deconvolution of O 1s spectra.

Temperature	R[H_2] (%)	*M–O*	V_O	*–OH*
as-deposited	0	67.70	27.35	4.95
	8	61.28	26.08	12.63
T_{ann} = 300 °C	0	68.63	26.42	4.95
T_{ann} = 150 °C	8	64.09	25.08	10.83

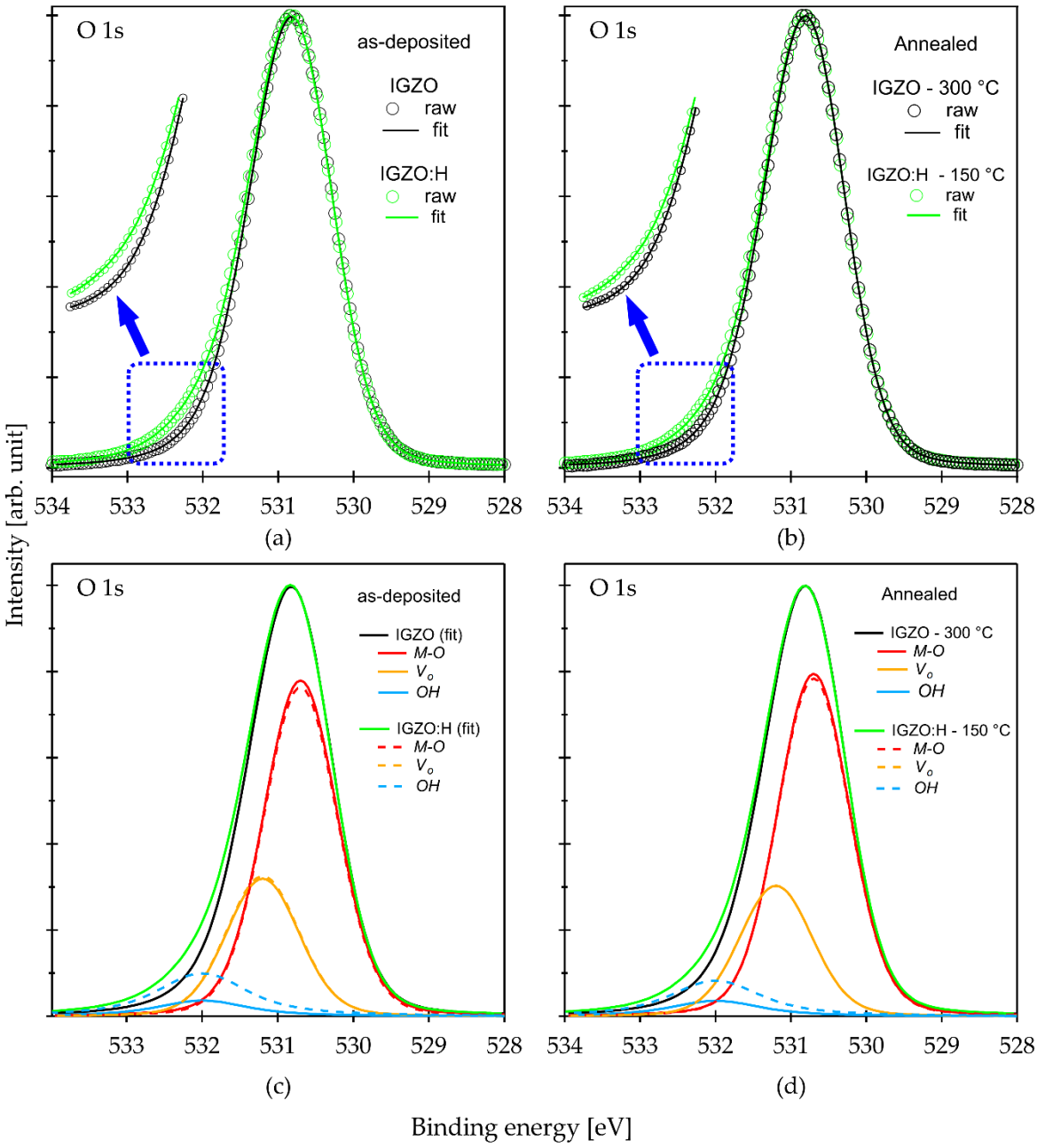

Figure 3.7 O 1s spectra of IGZO and IGZO:H films: (a) and (c) as-deposited before and after de-convolution, respectively; (b) and (d) annealed films in air for 1 h before and after deconvolution, respectively.

Figure 3.8 shows the valence band configuration from E_F of the (a) as-deposited and (b) annealed films, respectively. As can be seen in Figure 3.8(a), both the near-VBM and near E_F states of as-deposited IGZO:H film deposited at $R[H_2] = 8\%$ were slightly increased as compared with the as-deposited conventional IGZO film. It is known that the oxygen-deficiencies (i.e. V_O) in a-IGZO can be classified into two different groups, which are reasons for the subgap states. First one is the non-bonding state of metal cation since the CBM is formed by the overlapped indium

5s-orbitals responsible for electron transport in the film [44]. First principle calculation showed that the V_O defects due to the formation of *M-M* bonds between In and Zn atoms are located near-CBM [29]. It has also been shown experimentally that the step-wise shape near-CBM states can be attributed to a metallic indium [45]. Moreover, the uncoordinated In is proposed as an origin of electron traps which deteriorate the TFT performance [11,46].

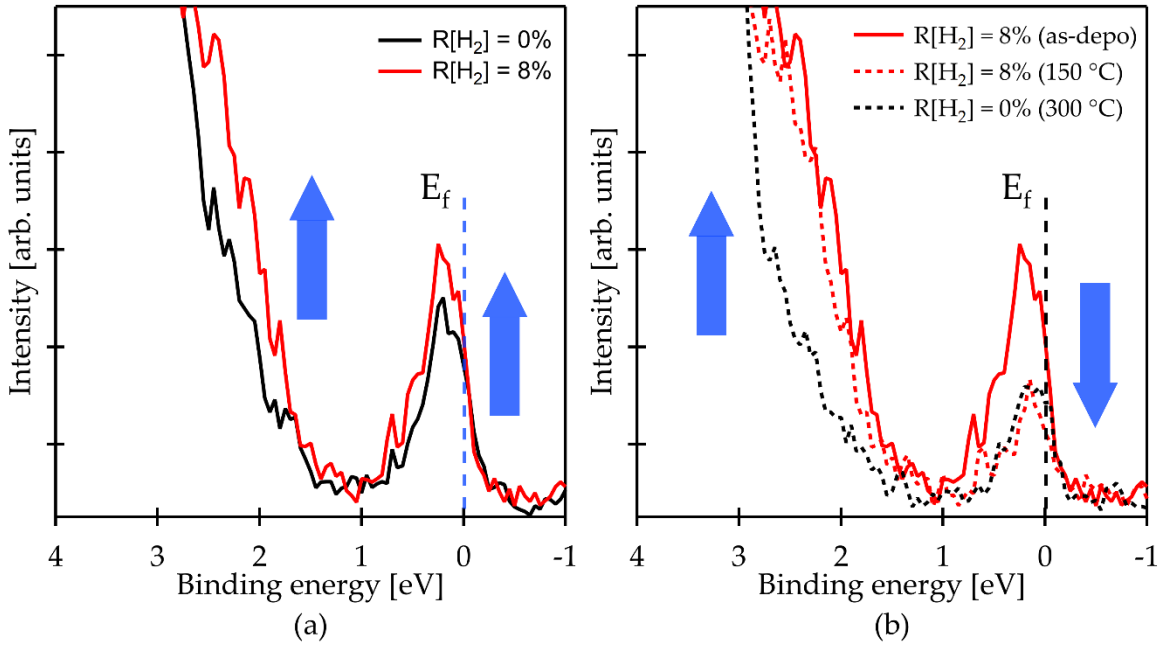

Figure 3.8 HAXPES spectra around band gap of the IGZO films deposited at different R[H_2] and at fixed R[O_2] = 1%: (a) as-deposited; (b) before and after annealing for 1 h in air.

Second one is deep fully-occupied V_O states which can be found above the VBM at 0.4 – 1.0 eV [44]. On the one hand, part of the surface defects can be effectively terminated by formation of the *OH* bonds reducing the near-VBM states, as was reported by wet annealing [39]. On the other hand, by doping with hydrogen, the V_O located near-CBM can be terminated by H stabilization at the V_O site, therefore resulting in reduction of near-CBM states, but which causes the increase in the near-VBM states due to additional formation of *M-H* bonds. These *M-H* bonds are located above the VBM within 0.4 eV [31]. In addition, it was also reported that incorporation of H_2O impurities resulted in increase in the near-VBM states [47]. Therefore, since the IGZO:H film was deposited by hydrogen-contained reduction atmosphere, promoting oxygen deficiency, the increased near E_F states in as-deposited H doped IGZO film can be attributed to additionally

formed *M-M* bonds since the *M-O* bonds decreased as was shown by O 1s spectra. Whereas the increased near-VBM states can be attributed to the additionally formed *OH* and *M-H* bonds.

After the annealing at 150 °C as shown in Figure 3.8(b), the near E_F defects of the IGZO:H film significantly decreased to the same level as that of the conventional IGZO film after annealing at 300 °C. It should be noted that the decrease of the near E_F defects of the IGZO film strongly correlated with the oxygen diffusing into the film during annealing as was previously discussed. The decrease of the near E_F defects of the IGZO:H was observed after annealing at 150 °C. This result can also be explained by the oxygen diffusion into the film during the annealing. The *in-situ* Hall measurement in Figure 3.3(a) and Figure 3.5(c) revealed the starting temperature of O diffusion in the IGZO and IGZO:H ($R[H_2]$ = 8%) films was approximately 240 °C and 100 °C, respectively. These results demonstrate that hydrogen doping in the IGZO film reduces the starting temperature of oxygen diffusion into the film; as a consequence, the near E_F defects can be effectively reduced by O diffusion at relatively low-temperature annealing. On the other hand, a slight decrease in the near-VBM states was also observed from the IGZO:H film after annealing at low temperature, which can be due to a termination of the deep V_O by O diffusion. However, inefficient elimination of these states by O diffusion can be explained by the thermally stable *M-M:H* bonds with high binding energy [31]. Therefore, hydrogen doping is a promising way to reduce the near E_F defects in the IGZO film at low temperature for improving the TFT performances of flexible devices.

3.5.3. Structural property analysis

In order to elucidate the possible cause of enhanced oxygen diffusion into the H doped IGZO films the structural properties were analysed. The Cauchy relationship (equation 3.1), as one of the most common dispersion models used in ellipsometry, was utilized to determine the refractive index of the deposited films [48].

$$n(\lambda) = A + \frac{B}{\lambda^2} + \frac{C}{\lambda^4}, \tag{3.1}$$

where A, B and C are fit parameters that control the shape of the n(λ). In particular, A is the index of refraction of the material when λ tends to ∞. B and C affect the curvature and the amplitude of the refractive index for medium wavelengths in the visible and ultraviolet range, respectively. Since neither the thickness nor the refractive index of the analyzed films is known, the solution of such problems is based on a regression analysis consisting of several basic stages, namely: (i) measuring the sample, (ii) constructing a model with assumed film thickness and refractive index parameters, (iii) comparing the constructed model with the measurement data, (iv) clarifying the main parameters. This regression analysis is finished when minimum mean square (MSE) error between theoretical model and experimental data is achieved. Figure 3.9 depicts the flow chart for ellipsometry data analysis.

The Cauchy model consisting of the IGZO as top layer and 0.7 mm thick glass substrate as a bottom layer was utilized. The measurements were done at three angles of incidence of 55°, 60° and 65°. The fitting was performed within 1 eV to 3 eV with backside correction. Then the calculated values were fitted till the minimum Mean Square Error (MSE) between the fit and experimental results was achieved. The corresponding film thickness for electrical and structural properties was extracted from the ellipsometry analysis. The refractive index (n) was extracted at a wavelength of the 632.8 nm HeNe laser source. Figure 3.10 shows the best fitting results and difference between the experimental and generated model after regression analysis of as-deposited conventional IGZO film obtained by using Cauchy model. Obtained MSE values were between 3.7 and 4.5, which indicates that the model obtained was sufficiently accurate compared to

the experimental data during the measurement process. Obtained MSE, refractive index and other Cauchy model values extracted from the ellipsometry results of as-deposited film and after annealing at 150 °C are summarized in Table 3.7 and Table 3.8, respectively. Thus, the refractive index (n) gradually decreased as R[H_2] increased for both as-deposited and annealed films. These results suggest that H incorporation into the IGZO film during deposition affects the film structure, decreasing the film density.

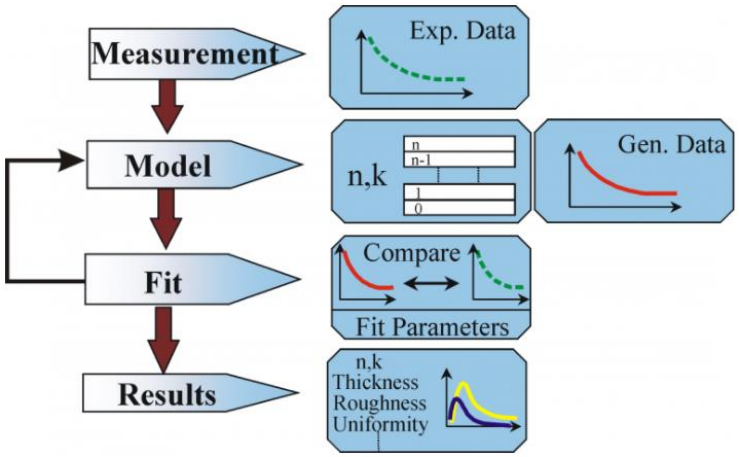

Figure 3.9 Regression analysis flow chart for the ellipsometry data analysis [49].

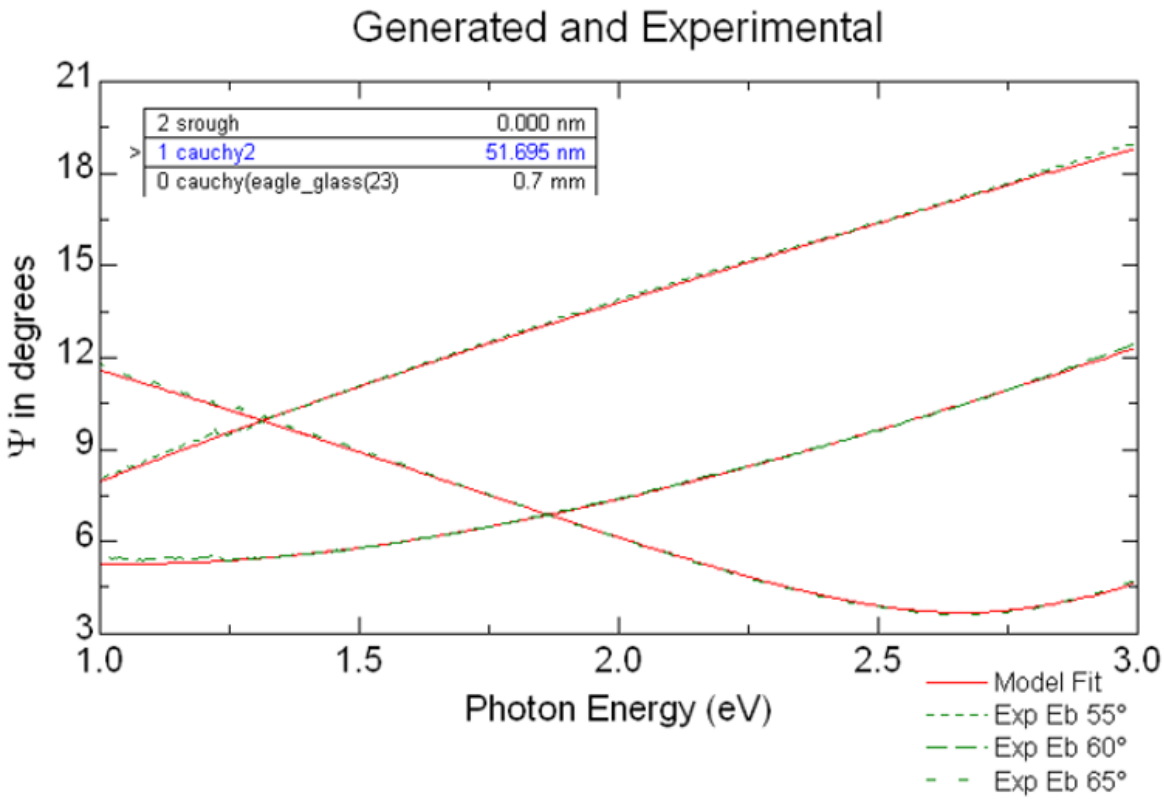

Figure 3.10 Generated and experimental results of regression analysis for as-deposited IGZO film.

Table 3.7 Extracted values of as-deposited IGZO and IGZO:H films from ellipsometry

	$R[H_2]$ = 0%	$R[H_2]$ = 2%	$R[H_2]$ = 5%	$R[H_2]$ = 8%
Thickness, (nm)	51.7	55.5	53.5	51.1
Refractive index (n)	1.966	1.949	1.936	1.928
A	1.9193	1.8901	1.8692	1.8637
MSE	4.1	4.5	3.9	3.7

Table 3.8 Extracted values of IGZO and IGZO:H films after annealing at after annealing at 150 °C from ellipsometry

	$R[H_2]$ = 0%	$R[H_2]$ = 2%	$R[H_2]$ = 5%	$R[H_2]$ = 8%
Thickness, (nm)	50.6	54.2	52.3	56.0
Refractive index (n)	1.971	1.955	1.949	1.946
A	1.9244	1.8998	1.9036	1.9002
MSE	4.2	4.2	4.1	4.2

Next, XRR film analysis was performed in order to determine and confirm the film density. The evaluation of the film was done at grazing angles of incidence from 0 to 3 degree as shown in Figure 3.11. The XRR results were analysed by fitting the model with the corresponding film thickness obtained from the ellipsometry analysis to the experimental data. Thickness of the films used in this study was in the range 45–53 nm.

Table 3.9 shows the extracted values of the film density after the fitting. It can be seen that H incorporation gradually decreased the initial density of the as-deposited films by 1.2 %, 3.2 % and 3.5 %, which were deposited at $R[H_2]$ = 2 %, 5 % and 8 %, respectively. Decrease of the film density observed from the IGZO:H is due to the increased content of *OH* groups as was revealed by HAXPES analysis since the film density decreased with an increase of $R[H_2]$. The tendency for the decrease in film density remained after annealing at 150 °C. The tendency for the decrease in film density remained after annealing at 150 °C and amounted to 0.6 %, 1.5 %, and 2.5 % toward a higher $R[H_2]$.

Table 3.9 IGZO film density (g/cm^3) changes after deposition at different $R[H_2]$.

$R[H_2]$ (%)	0	2	5	8
as-deposited	6.124	6.049	5.926	5.913
T_{ann} = 150 °C	6.075	6.035	5.985	5.922

It was reported that structural relaxation without noticeable densification occurs at a low-temperature range (< 300 °C) [50]. Thus, the film densification through low-temperature (150 °C) annealing, which was observed from the IGZO:H films deposited at R[H_2] of 5% and 8%, would be caused by the oxygen diffusion in the films.

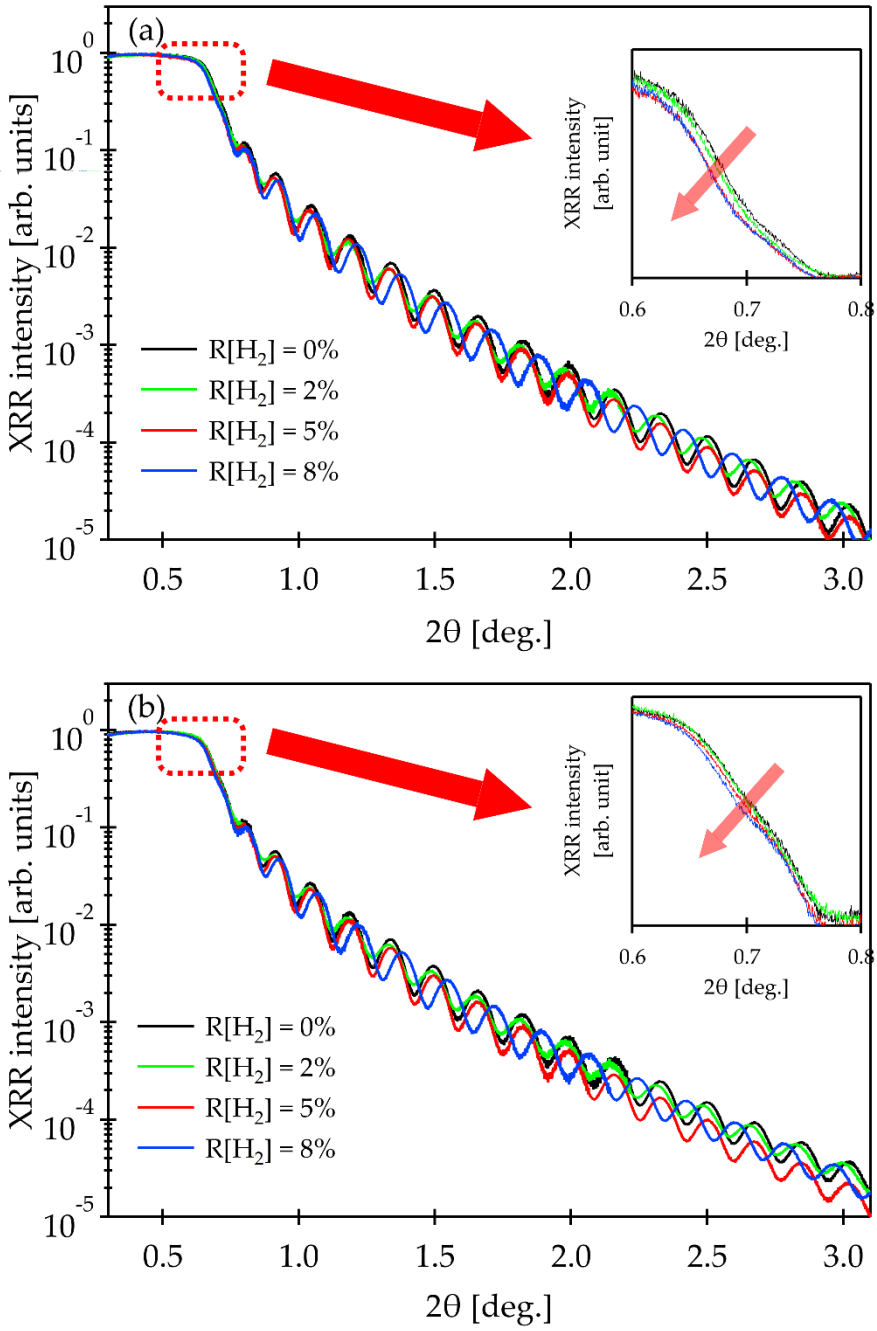

Figure 3.11 XRR results of the IGZO films deposited at different R[H_2] and at fix R[O_2] of 1%: (a) as-deposited; (b) after annealing in air for 1 h at the annealing temperature of 150 °C. The insets show the reflectivity intensity near the critical angle representing change in the film density upon the hydrogen incorporation.

On the other hand, the density of the IGZO film depends on the deposition pressure during synthesis, affecting the microstructure. It was reported that deposition at high pressure leads to the formation of a low density film with a porous columnar structure, compared to deposition at low pressure with a more uniform structure [51]. It is assumed that such microstructural change (film density reduction) is caused by the incorporation of weakly bonded O and H at higher deposition pressure, which was experimentally detected by TDS, as shown in Figure 3.12 [51].

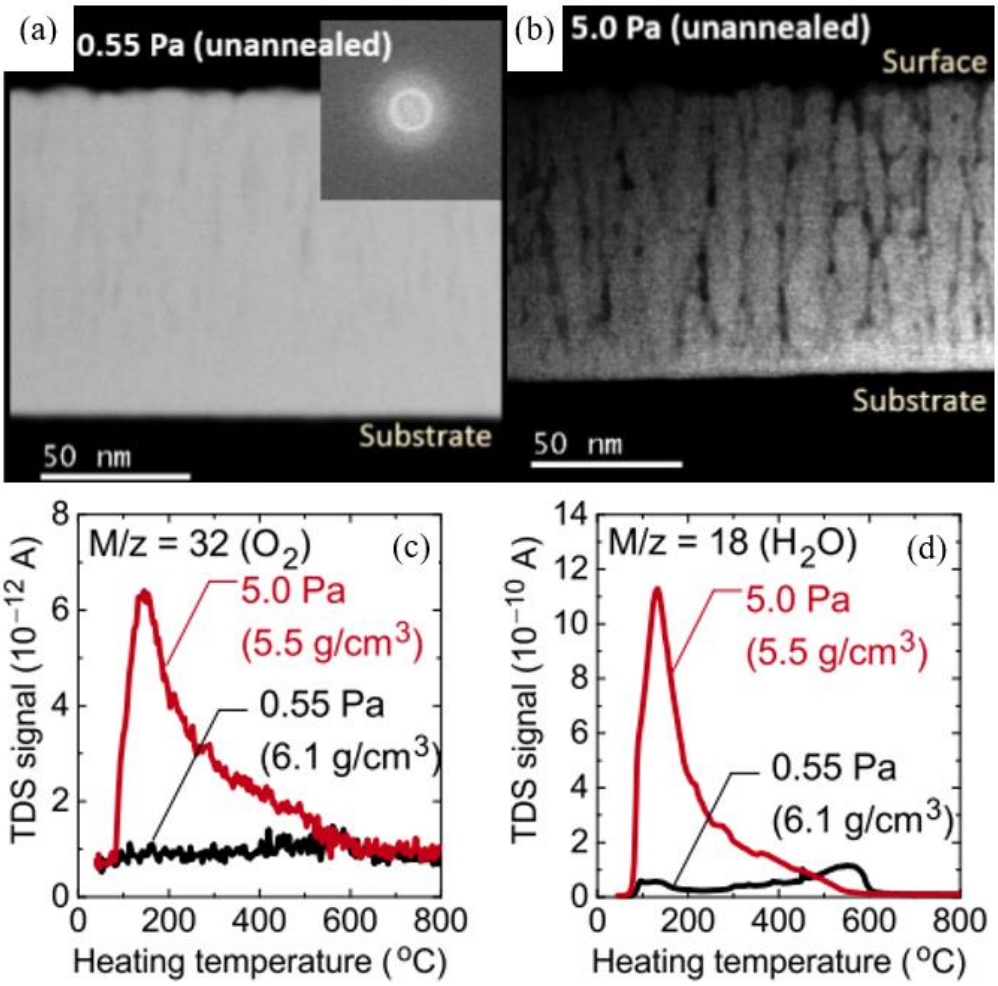

Figure 3.12 (a) and (b) High-angle annular dark-field imaging in the scanning transmission electron microscopy of as-deposited a-IGZO films deposited at different base pressure; TDS spectra of (c) O_2 and (d) H_2O for IGZO films with different film density [51].

In contrast, Amit et. al has performed the first principle calculation for H doped In_2O_3 and analyzed the role of defects. It was shown that the interstitial H^+ has low formation energy and bonds to lattice oxygen forming *O-H* bonds. Formation of these *O-H* bonds leads to a displacement of O in the lattice, even though H is much lighter than O [52]. In addition, a water molecule

in In_2O_3 is split into H^+ and OH^- resulting in higher H^+ concentration compared to the deposition in the H atmosphere [53]. This split can be considered as an additional source of H^+ formation since the back pressure before the deposition is related to residual water.

Thus, the film densification through low-temperature (150 °C) annealing, which was observed from the IGZO:H films deposited at R[H_2] of 5% and 8%, would be caused by the oxygen diffusion in the films and OH desorption during the annealing. The XRR result is in good agreement with the *in-situ* Hall measurements. Comparing the film density as listed in Table 3.9 and *in-situ* Hall measurements of the N_e variation shown in Figure 3.5(a)-3.5(c), the higher the H content showed lower the film density and the shift of the O diffusion starting temperature toward a lower temperature side. Thus, it can be considered that the hydrogen doping into the IGZO film led to structural modification facilitating the diffusion of O into the bulk film structure. As a consequence, the amount of V_O and the defects near E_F could be reduced by oxidation of the films.

3.6. Conclusion

1. Analysis of the electrical properties of conventional and hydrogen-doped IGZO films deposited at various hydrogen ratios showed that N_e continuously decreased after air annealing. However, the point where N_e began to decrease strongly correlates with H content, and this point shifted toward a lower temperature for higher $R[H_2]$. Thus, mechanism causing such N_e variation and activation temperature reduction in the IGZO:H films was investigated.
2. *In-situ* Hall measurements of conventional IGZO film performed in air revealed that the oxygen diffusion from the ambient air into the conventional IGZO film begins at a temperature of > 240 °C promoting subsequent oxidation, effective N_e and near E_F defects reduction.
3. Incorporation of H into the IGZO film resulted in a significant decrease of the oxygen diffusion start temperature from 240 °C to approximately 100 °C. In addition, results of the time-dependence annealing in air at 150 °C showed the decrease in the initial slope of the N_e decrease suggesting higher oxygen diffusion coefficient for higher hydrogen content in the film. Whereas, the same analysis of time-dependence annealing performed in N_2 atmosphere showed that N_e remained at a relatively high level of 10^{18} - 10^{19} cm^{-3} for all the films with different $R[H_2]$ values, additionally supporting an importance of the O presence in the annealing ambient.
4. HAXPES results showed that the near E_F defects of the H doped IGZO film after low-temperature annealing at 150 °C were comparable to that of the conventional IGZO film annealed at 300 °C. This indicates that the near E_F defects can be effectively reduced by the enhanced O diffusion at low temperature.
5. XRR analysis revealed structural changes upon H incorporation which resulted in a decrease of the film density, which might be the reason facilitating the O diffusion into the bulk region at low-temperature.
6. Hydrogen introduction into the IGZO films holds promise for low-temperature applications, such as flexible electronics.

Chapter contribution

Based on this chapter the manuscript titled ***«Defect Passivation and Carrier Reduction Mechanisms in Hydrogen-Doped In-Ga-Zn-O (IGZO:H) Films upon Low-Temperature Annealing for Flexible Device Applications»***, **Rostislav Velichko**, Y. Magari, and M. Furuta, Materials **2022**, 15, 334, *https://doi.org/10.3390/ma15010334*, was published.

References

1. Hideo Hosono, Masahiro Yasakawa, H.K. Novel oxide amorphous semiconductors : transparent conducting amorphous oxides Possible Candidate for HMCs. *J. Non. Cryst. Solids* **1996**, *203*, 334–344.
2. K. Nomura; H. Ohta; A. Takagi; T. Kamiya; M. Hirano; Hosono, H. Room-temperature fabrication of transparent flexible thin-film transistors using amorphous oxide semiconductors. *Nature* **2004**, *432*, 488.
3. Kim, J.; Bang, J.; Nakamura, N.; Hosono, H. Ultra-wide bandgap amorphous oxide semiconductors for NBIS-free thin-film transistors. *APL Mater.* **2019**, *7*, doi:10.1063/1.5053762.
4. Shiah, Y.S.; Sim, K.; Ueda, S.; Kim, J.; Hosono, H. Unintended Carbon-related Impurity and Negative Bias Instability in High-Mobility Oxide TFTs. *IEEE Electron Device Lett.* **2021**, doi:10.1109/LED.2021.3101654.
5. Fortunato, E.; Barquinha, P.; Martins, R. Oxide semiconductor thin-film transistors: A review of recent advances. *Adv. Mater.* **2012**, *24*, 2945–2986, doi:10.1002/adma.201103228.
6. Matsuo, T.; Mori, S.; Ban, A.; Imaya, A. Advantages of IGZO oxide semiconductor. *Dig. Tech. Pap. - SID Int. Symp.* **2014**, *45*, 83–86, doi:10.1002/j.2168-0159.2014.tb00023.x.
7. Kamiya, T.; Nomura, K.; Hosono, H. Present status of amorphous In-Ga-Zn-O thin-film transistors. *Sci. Technol. Adv. Mater.* **2010**, *11*, doi:10.1088/1468-6996/11/4/044305.
8. Kamiya, T.; Hosono, H. Material characteristics and applications of transparent amorphous oxide semiconductors. *NPG Asia Mater.* **2010**, *2*, 15–22, doi:10.1038/asiamat.2010.5.
9. Nomura, K.; Kamiya, T.; Yanagi, H.; Ikenaga, E.; Yang, K.; Kobayashi, K.; Hirano, M.; Hosono, H. Subgap states in transparent amorphous oxide semiconductor, In-Ga-Zn-O, observed by bulk sensitive x-ray photoelectron spectroscopy. *Appl. Phys. Lett.* **2008**, *92*, doi:10.1063/1.2927306.

10. Aman, M.; Takeda, Y.; Ito, K.; Yamamoto, K.; Tanaka, K.; Matsukizono, H.; Nakamura, W.; Makita, N. Reliability improvement of IGZO-TFT in hybrid process with LTPS. *J. Soc. Inf. Disp.* **2021**, *29*, 416–427, doi:10.1002/jsid.1032.
11. Ide, K.; Nomura, K.; Hosono, H.; Kamiya, T. Electronic Defects in Amorphous Oxide Semiconductors: A Review. *Phys. Status Solidi Appl. Mater. Sci.* **2019**, *216*, 1–28, doi:10.1002/pssa.201800372.
12. Ji, K.H.; Kim, J.I.; Jung, H.Y.; Park, S.Y.; Choi, R.; Mo, Y.G.; Jeong, J.K. Comprehensive studies of the degradation mechanism in amorphous InGaZnO transistors by the negative bias illumination stress. *Microelectron. Eng.* **2011**, *88*, 1412–1416, doi:10.1016/j.mee.2011.03.069.
13. Mativenga, M.; Haque, F.; Billah, M.M.; Um, J.G. Origin of light instability in amorphous IGZO thin-film transistors and its suppression. *Sci. Rep.* **2021**, *11*, 1–12, doi:10.1038/s41598-021-94078-8.
14. Hanyu, Y.; Abe, K.; Domen, K.; Nomura, K.; Hiramatsu, H.; Kumomi, H.; Hosono, H.; Kamiya, T. Effects of high-temperature annealing on operation characteristics of a-In-Ga-Zn-O TFTs. *IEEE/OSA J. Disp. Technol.* **2014**, *10*, 979–983, doi:10.1109/JDT.2014.2352860.
15. Jallorina, M.P.A.; Bermundo, J.P.S.; Fujii, M.N.; Ishikawa, Y.; Uraoka, Y. Significant mobility improvement of amorphous In-Ga-Zn-O thin-film transistors annealed in a low temperature wet ambient environment. *Appl. Phys. Lett.* **2018**, *112*, doi:10.1063/1.5026515.
16. Ide, K.; Kikuchi, Y.; Nomura, K.; Kimura, M.; Kamiya, T.; Hosono, H. Effects of excess oxygen on operation characteristics of amorphous In-Ga-Zn-O thin-film transistors. *Appl. Phys. Lett.* **2011**, *99*, 1–4, doi:10.1063/1.3633100.
17. Kim, W.G.; Tak, Y.J.; Du Ahn, B.; Jung, T.S.; Chung, K.B.; Kim, H.J. High-pressure gas activation for amorphous indium-gallium-zinc-oxide thin-film transistors at 100 °c. *Sci. Rep.* **2016**, *6*, 1–7, doi:10.1038/srep23039.
18. Miyakawa, M.; Nakata, M.; Tsuji, H.; Fujisaki, Y. Highly stable low-temperature aqueous solution-processed oxide thin-film transistors by the hydrogen injection and oxidation method. *Flex. Print. Electron.* **2018**, *3*, 025005, doi:10.1088/2058-8585/aac125.
19. Jang, S.C.; Park, J.; Kim, H. Do; Hong, H.; Chung, K.B.; Kim, Y.J.; Kim, H.S. Low temperature activation of amorphous In-Ga-Zn-O semiconductors using microwave and e-beam radiation, and the associated thin film transistor properties. *AIP Adv.* **2019**, *9*, doi:10.1063/1.5082862.

20. Liu, C.; Sun, Y.; Qin, H.; Liu, Y.; Wei, S.; Zhao, Y. Low-Temperature, High-Performance InGaZnO Thin-Film Transistors Fabricated by Capacitive Coupled Plasma-Assistant Magnetron Sputtering. *IEEE Electron Device Lett.* **2019**, *40*, 415–418, doi:10.1109/LED.2019.2896111.

21. Lee, I.S.; Tak, Y.J.; Kang, B.H.; Yoo, H.; Jung, S.; Kim, H.J. Mechanochemical and Thermal Treatment for Surface Functionalization to Reduce the Activation Temperature of In-Ga-Zn-O Thin-film Transistors. *ACS Appl. Mater. Interfaces* **2020**, *12*, 19123–19129, doi:10.1021/acsami.9b22831.

22. Aman, S.G.M.; Magari, Y.; Shimpo, K.; Hirota, Y.; Makino, H.; Koretomo, D.; Furuta, M. Low-temperature (150°C) activation of Ar+O2+H2-sputtered In–Ga–Zn–O for thin-film transistors. *Appl. Phys. Express* **2018**, *11*, 081101, doi:10.7567/APEX.11.081101.

23. Magari, Y.; Aman, S.G.M.; Koretomo, D.; Masuda, K.; Shimpo, K.; Furura, M. Low-Temperature (150 °c) processed metal-semiconductor field-effect transistor with a hydrogenated In-Ga-Zn-O stacked channel. *Jpn. J. Appl. Phys.* **2020**, *59*, 6–11, doi:10.7567/1347-4065/ab65af.

24. Koretomo, D.; Hamada, S.; Mori, M.; Magari, Y.; Furuta, M.; Furuta, M.; Furuta, M. Marked improvement in reliability of 150 °c processed IGZO thin-film transistors by applying hydrogenated IGZO as a channel material. *Appl. Phys. Express* **2020**, *13*, doi:10.35848/1882-0786/ab9478.

25. Van De Walle, C.G. Hydrogen as a cause of doping in zinc oxide. *Phys. Rev. Lett.* **2000**, *85*, 1012–1015, doi:10.1103/PhysRevLett.85.1012.

26. Oh, S.I.; Choi, G.; Hwang, H.; Lu, W.; Jang, J.H. Hydrogenated IGZO thin-film transistors using high-pressure hydrogen annealing. *IEEE Trans. Electron Devices* **2013**, *60*, 2537–2541, doi:10.1109/TED.2013.2265326.

27. Miyase, T.; Watanabe, K.; Sakaguchi, I.; Ohashi, N.; Domen, K.; Nomura, K.; Hiramatsu, H.; Kumomi, H.; Hosono, H.; Kamiya, T. Roles of Hydrogen in Amorphous Oxide Semiconductor In-Ga-Zn-O: Comparison of Conventional and Ultra-High-Vacuum Sputtering. *ECS J. Solid State Sci. Technol.* **2014**, *3*, Q3085–Q3090, doi:10.1149/2.015409jss.

28. Omura, H.; Kumomi, H.; Nomura, K.; Kamiya, T.; Hirano, M.; Hosono, H. First-principles study of native point defects in crystalline indium gallium zinc oxide. *J. Appl. Phys.* **2009**, *105*, doi:10.1063/1.3089232.

29. Körner, W.; Urban, D.F.; Elsässer, C. Origin of subgap states in amorphous In-Ga-Zn-O. *J. Appl. Phys.* **2013**, *114*, doi:10.1063/1.4826895.

30. Magari, Y.; Aman, S.G.M.; Koretomo, D.; Masuda, K.; Shimpo, K.; Makino, H.; Kimura, M.; Furuta, M. Record-High-Performance Hydrogenated In-Ga-Zn-O Flexible Schottky Diodes. *ACS Appl. Mater. Interfaces* **2020**, doi:10.1021/acsami.0c12638.

31. Bang, J.; Matsuishi, S.; Hosono, H. Hydrogen anion and subgap states in amorphous In-Ga-Zn-O thin films for TFT applications. *Appl. Phys. Lett.* **2017**, *110*, doi:10.1063/1.4985627.

32. Toda, T.; Wang, D.; Jiang, J.; Hung, M.P.; Furuta, M. Quantitative analysis of the effect of hydrogen diffusion from silicon oxide etch-stopper layer into amorphous In-Ga-Zn-O on thin-film transistor. *IEEE Trans. Electron Devices* **2014**, *61*, 3762–3767, doi:10.1109/TED.2014.2359739.

33. Nam, Y.; Kim, H.O.; Cho, S.H.; Ko Park, S.H. Effect of hydrogen diffusion in an In-Ga-Zn-O thin film transistor with an aluminum oxide gate insulator on its electrical properties. *RSC Adv.* **2018**, *8*, 5622–5628, doi:10.1039/c7ra12841j.

34. Nomura, K.; Kamiya, T.; Hosono, H. Effects of Diffusion of Hydrogen and Oxygen on Electrical Properties of Amorphous Oxide Semiconductor, In-Ga-Zn-O. *ECS J. Solid State Sci. Technol.* **2013**, *2*, P5–P8, doi:10.1149/2.011301jss.

35. Lin, T.C.; Huang, W.C.; Lan, W.C. A study on the electrical and optical characteristics of IGZO films. *J. Mater. Sci. Mater. Electron.* **2014**, *25*, 3077–3084, doi:10.1007/s10854-014-1986-z.

36. Song, A.; Park, H.W.; Chung, K.B.; Rim, Y.S.; Son, K.S.; Lim, J.H.; Chu, H.Y. Modulation of the electrical properties in amorphous indium-gallium zinc-oxide semiconductor films using hydrogen incorporation. *Appl. Phys. Lett.* **2017**, *111*, doi:10.1063/1.5003186.

37. Nomura, K.; Kamiya, T.; Ohta, H.; Hirano, M.; Hosono, H. Defect passivation and homogenization of amorphous oxide thin-film transistor by wet O2 annealing. *Appl. Phys. Lett.* **2008**, *93*, 1–4, doi:10.1063/1.3020714.

38. Kamiya, T.; Nomura, K.; Hosono, H. Origin of definite Hall voltage and positive slope in mobility-donor density relation in disordered oxide semiconductors. *Appl. Phys. Lett.* **2010**, *96*, 1–4, doi:10.1063/1.3364131.

39. Nomura, K.; Kamiya, T.; Ikenaga, E.; Yanagi, H.; Kobayashi, K.; Hosono, H. Depth analysis of subgap electronic states in amorphous oxide semiconductor, a-In-Ga-Zn-O, studied by hard x-ray photoelectron spectroscopy. *J. Appl. Phys.* **2011**, *109*, doi:10.1063/1.3560769.

40. Shin, Y.; Kim, S.T.; Kim, K.; Kim, M.Y.; Oh, S.; Jeong, J.K. The Mobility Enhancement of Indium Gallium Zinc Oxide Transistors via Low-temperature Crystallization using a Tantalum Catalytic Layer. *Sci. Rep.* **2017**, *7*, 1–10, doi:10.1038/s41598-017-11461-0.

41. Chou, T.-C.; Kao, Y.-W.; Chiu, K.-C. Effect of Oxygen Amount on Electrical and Transparency Characteristics of Amorphous IGZO Thin Film Fabricated by Sputtering. *Trans. Mater. Res. Soc. Japan* **2013**, *38*, 593–596, doi:10.14723/tmrsj.38.593.

42. de Jamblinne de Meux, A.; Bhoolokam, A.; Pourtois, G.; Genoe, J.; Heremans, P. Oxygen vacancies effects in a-IGZO: Formation mechanisms, hysteresis, and negative bias stress effects. *Phys. Status Solidi Appl. Mater. Sci.* **2017**, *214*, doi:10.1002/pssa.201600889.

43. Peng, C.; Yang, S.; Pan, C.; Li, X.; Zhang, J. Effect of Two-Step Annealing on High Stability of a-IGZO Thin-Film Transistor. *IEEE Trans. Electron Devices* **2020**, *67*, 4262–4268, doi:10.1109/TED.2020.3017718.

44. Kamiya, T.; Nomura, K.; Hosono, H. Origins of High Mobility and Low Operation Voltage of Amorphous Oxide TFTs: Electronic Structure, Electron Transport, Defects and Doping*. *J. Disp. Technol.* **2009**, *5*, 468–483, doi:10.1109/jdt.2009.2034559.

45. Tang, H.; Ishikawa, K.; Ide, K.; Hiramatsu, H.; Ueda, S.; Ohashi, N.; Kumomi, H.; Hosono, H.; Kamiya, T. Effects of residual hydrogen in sputtering atmosphere on structures and properties of amorphous In-Ga-Zn-O thin films. *J. Appl. Phys.* **2015**, *118*, doi:10.1063/1.4936552.

46. Nahm, H.H.; Kim, Y.S. Undercoordinated indium as an intrinsic electron-trap center in amorphous InGaZnO4. *NPG Asia Mater.* **2014**, *6*, 1–5, doi:10.1038/am.2014.103.

47. Orui, T.; Herms, J.; Hanyu, Y.; Ueda, S.; Watanabe, K.; Sakaguchi, I.; Ohashi, N.; Hiramatsu, H.; Kumomi, H.; Hosono, H.; et al. Charge compensation by excess oxygen in amorphous In-Ga-Zn-O films deposited by pulsed laser deposition. *IEEE/OSA J. Disp. Technol.* **2015**, *11*, 518–522, doi:10.1109/JDT.2014.2358251.

48. Patel, D.; Shah, D.; Hilfiker, J.N.; Linford, M. A Tutorial on Spectroscopic Ellipsometry (SE), 2. The Cauchy Model. *Vac. Technol. Coat.* **2019**, 29–33.

49. Ellipsometry Data Analysis - J.A. Woollam Available online: https://www.jawoollam.com/resources/ellipsometry-tutorial/ellipsometry-data-analysis.

50. Ide, K.; Nomura, K.; Hiramatsu, H.; Kamiya, T.; Hosono, H. Structural relaxation in amorphous oxide semiconductor, a-In-Ga-Zn-O. *J. Appl. Phys.* **2012**, *111*, doi:10.1063/1.3699372.

51. Ide, K.; Kikuchi, M.; Ota, M.; Sasase, M.; Hiramatsu, H.; Kumomi, H.; Hosono, H.; Kamiya, T. Effects of working pressure and annealing on bulk density and nanopore structures in amorphous In-Ga-Zn-O thin-film transistors. *Jpn. J. Appl. Phys.* **2017**, *56*, doi:10.7567/JJAP.56.03BB03.

52. Samanta, A.; Varley, J.B.; Lordi, V. The role of water vapor during the synthesis of hydrogen doped in 2 O 3. *Appl. Phys. Lett.* **2020**, *117*, 1–5, doi:10.1063/5.0011975.

53. Samanta, A.; Varley, J.B.; Lordi, V. Analysis of defects in In2O3:H synthesized in presence of water vapor and hydrogen gas mixture. *J. Appl. Phys.* **2021**, *129*, 1–10, doi:10.1063/5.0023216.

Chapter 4

Hydrogenated polycrystalline n-type In-Ga-O (IGO:H) for high-mobility TFTs

In this chapter the properties of hydrogenated polycrystalline (poly) n-type In-Ga-O films are discussed.

According to recent reports, active research in further increasing the mobility of the OS TFTs is focused on the use of materials with high-In content (In-rich). Thus, the mobility of monocrystalline In_2O_3 has been reported to be 160 cm^2/Vs, which makes polycrystalline InO_x a potential candidate material for high-mobility TFT application. However, such materials tend to be polycrystalline due to their ease of crystallization at low temperature, as well as spontaneous crystallization even during room temperature deposition. In addition, the electron concentration in In-rich OS is high, about 10^{20} cm^{-3}, which requires the development of methods to reduce the electron concentration for application in TFTs.

It was reported that the transparent conductive oxide (TCO) of polycrystalline InO_x can be formed by solid-phase crystallization at 200 °C by a sputtering process in the H_2O vapour contained in the Ar and O_2 atmosphere. In this study we investigated the H doping effects on electrical and structural properties of the IGO film. It was found that intensive H doping suppressed the crystallization during the film deposition. Hydrogen incorporation into the IGO film reduced the electron concentration by two orders of magnitude from 10^{20} cm^{-3} to below 10^{18} cm^{-3} through the crystallization process. On the other hand, the unintentional H doping can also occur in subsequent TFT fabrication steps. Therefore, the formation of a passivation layer is necessary to protect the channel and ensure TFT reliability. However, H can diffuse into the TFT channel, both during the passivation layer deposition and from it at a later stage. Thus, film properties and influence of H originated from the related processes are investigated. In addition, the film property in relation to TFT performance is discussed.

4.1. Introduction

Oxide semiconductors are expected to be a promising replacement for a-Si:H technology in next-generation flat panel displays because of their high mobility, high transparency, ease of synthesis. Two decades have passed since the first publications, and thanks to active development, AOS technology has progressed rapidly, strengthening the position of these materials. Nevertheless, for further progress, it is important to develop methods to further increase the mobility of OS-based TFTs. However, it is well-known that mobility in OS strongly depends on the composition materials, as shown in Figure 4.1(b) [1]. As can be seen, higher mobility is directly related to the content of In in the materials.

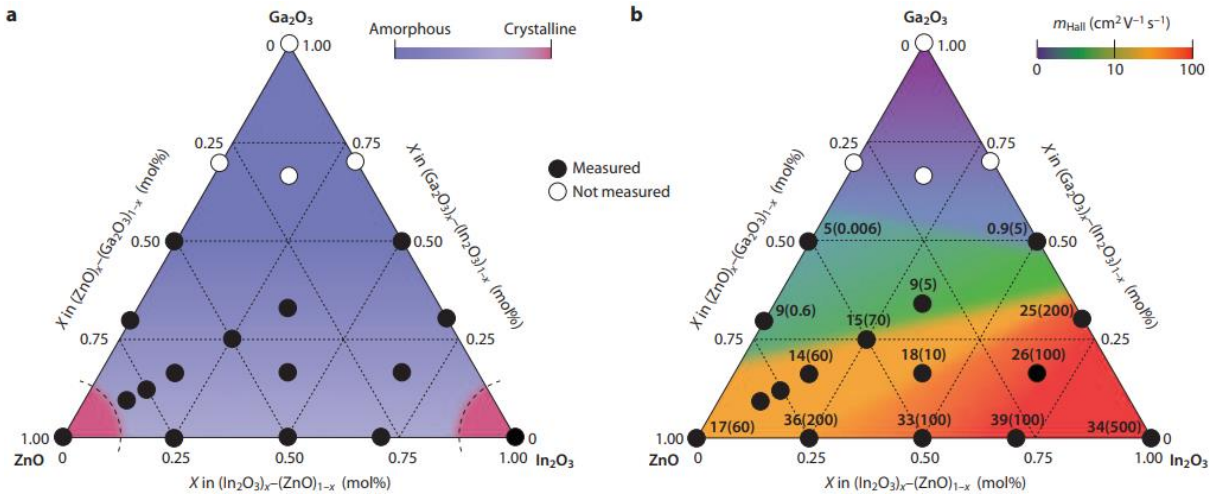

Figure 4.1 (a) Amorphous and crystalline formation map; (b) electron transport properties of thin films in relation to different composition [1]

According to the recent reports, active research in further increasing the mobility of the OS TFTs is focused on the use of materials with high-In content (In-rich), Figure 4.2 [2,3]. Thus, the mobility of monocrystalline In_2O_3 has been reported of 160 cm^2/Vs, which makes polycrystalline InO_x a potential candidate material for high-mobility TFT application [4,5]. However, such materials tend to be polycrystalline due to their ease of crystallization at low temperature, as well as spontaneous crystallization even during room or relatively low deposition temperature as low as < 100 °C [6]. Koida et. al reported that the polycrystalline In_2O_3 with mobility about 130 cm^2/Vs for transparent conductive oxide (TCO) application can be formed by solid-phase crystallization

(SPC) at 200 °C by a sputtering process in the H_2O vapour contained Ar and O_2 atmosphere [7,8]. However, despite the high value of the resulting mobility, a significant drawback is high electron concentration in In-rich OS, which is about 10^{20} cm^{-3} and attributed to the native defects such as oxygen vacancies. This implies the development of methods to reduce the electron concentration for application in TFTs with suitable and moderate values of threshold voltage (V_{th}) and ON/OFF current ratio.

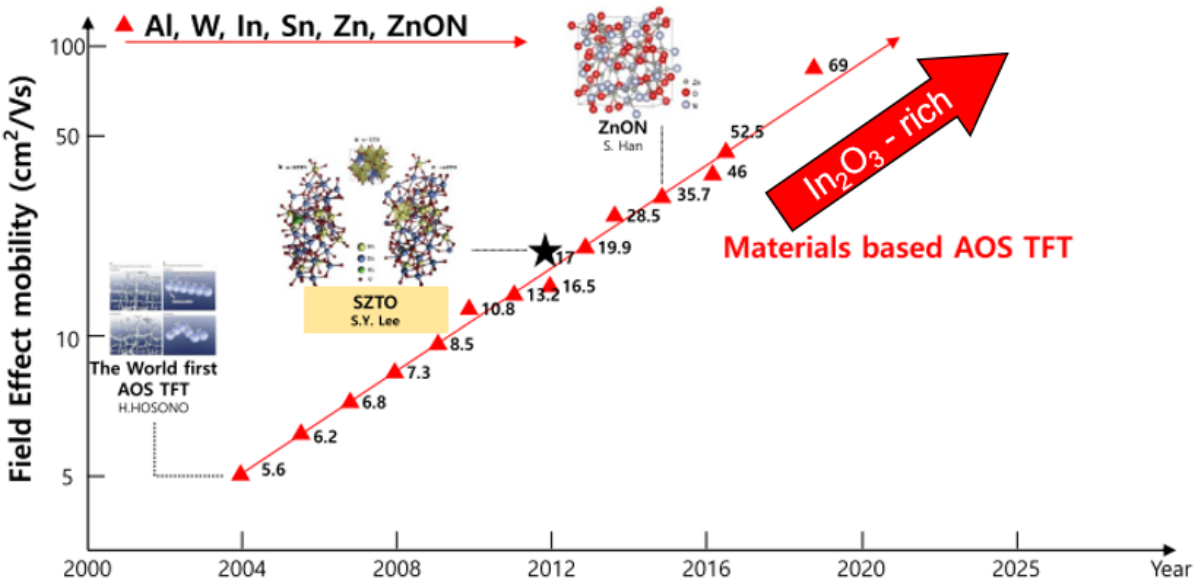

Figure 4.2 TFT field effect mobility based on various oxide semiconductors [2].

One of the methods to effectively control the oxygen deficiency in In_2O_3 is doping by different atoms which can create stable bonds with oxygen atoms. Ebata et. al reported that doping by Ga^{3+} with content less than 10% led to a suppression of carrier concentration in In-Ga-O (IGO) due to its high ionic potential resulting in a bonding to oxygen ions with high dissociation energy [9]. Thus, a TFT with a channel based on poly-IGO with a field effect mobility of 39.1 cm^2/Vs and carrier concentration of 10^{17} cm^{-3} was fabricated, demonstrating the possibility of using In-rich materials. Our research group has reported that H_2 doping during the RF magnetron sputtering of IGO in the Ar and O_2 atmosphere can be considered as an effective approach to achieve high-performance polycrystalline OS TFTs for future displays. In this work, we carried out studies on the improvement and optimization of the synthesis process IGO:H films, as well as the influence of secondary effects associated with the TFT fabrication process.

4.2. Substrate heating, base pressure and residual water effect

InO_x based materials are known to easily crystallize to a polycrystalline structure after the annealing step at relatively low temperatures or even during the deposition in vacuum. Thus, this leads to the inevitable formation of grains and, as a consequence, defects at the grain boundary including carrier scattering and trapping defects, which in turn directly affect the electrical properties and performance of the devices. Consequently, increasing grain size is one of the ways for improvement. Substrate temperature is known as an effective parameter affecting the crystallinity and in determining the grain size [10–12]. In order to investigate the possibility of controlling the grain size, IGO and IGO:H films were deposited on a glass substrate at room temperature as a reference sample, and at 200 °C for comparison. The deposition technique and parameters are summarized are shown and summarized in Figure 4.3 and Table 4.1, respectively.

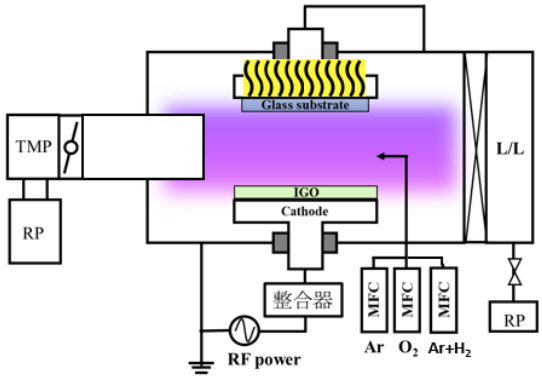

Figure 4.3 Deposition technique of IGO and IGO:H films by RF magnetron sputtering

Table 4.1 Deposition parameters of the IGO films.

Target	50 mm InGaO
Substrate	100 mm glass
Film thickness (nm)	50
Deposition time (min)	6′ 20″
Base pressure (Pa)	$< 5\times10^{-5}$
Deposition pressure (Pa)	0.3 Pa
RF power (W)	60
Total gas flow ($Ar+O_2+H_2$) (sccm)	10
Deposition temperature (°C)	RT / 200°C
$R[O_2] = O_2 / (Ar+O_2+H_2)$ (%)	4
$R[H_2] = H_2 / (Ar+O_2+H_2)$ (%)	0 & 5
Substrate to target distance	80 mm

Since the heat transfer in a vacuum is hampered, the actual substrate temperature may differ significantly from the set heater temperature. In order to ensure and stabilize the appropriate temperature of the substrate before deposition, the samples were kept in a vacuum deposition chamber for two hours. The actual temperature of the substrate after deposition was about 150 °C, which was confirmed by the temperature tape as shown in Figure 4.4

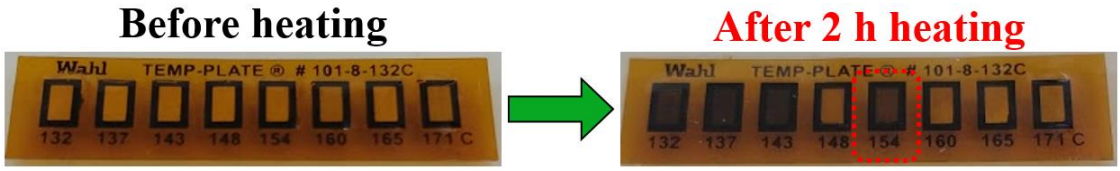

Figure 4.4 Temperature tape used to check the real substrate temperature prior to IGO deposition.

Figure 4.5(a) and (b) shows the XRD peaks of IGO films without and with substrate heating, respectively. The sample deposited at room temperature (RT) the substrate showed a crystal structure along (222) direction already after deposition without any post-annealing. The base pressure (P_{base}) of IGO without heating was 5.7×10^{-5} Pa. In contrast, the heated sample showed amorphous nature after deposition and diffraction pattern was observed after annealing at 150 °C. This suppression of crystallization during deposition can be due to an increase in P_{base} during heating the substrate, which was 1.2×10^{-4} Pa. As a consequence, the residual water content in the chamber increased due to desorption from the inner walls of the deposition chamber.

However, the main peak along (222) for the IGO film deposited at RT showed an intensity peak at 30.2°, and on subsequent annealing this peak shifted uniformly toward 30.8° according to annealing temperature, exhibiting a double-peak structure, as shown in Figure 4.6(a). Position of the main peak of IGO deposited at 200 °C remained unchanged at 30.8°over the entire annealing temperature range. This double-peak phenomenon was observed and investigated in ITO films. Yi et. al performed a wet etching and found that the left peak is less stable than the right one. Authors concluded that diffraction peak at 30.2° is formed due to vapor-phase crystallization. This strongly strained layer is located on top (surface) of the ITO film, while the bottom layer is more stable and formed through the solid-phase crystallization (SPC) during the film annealing, as shown in Figure 4.7 [13]. This lower layer formed by SPC provides a diffraction peak at 30.8°.

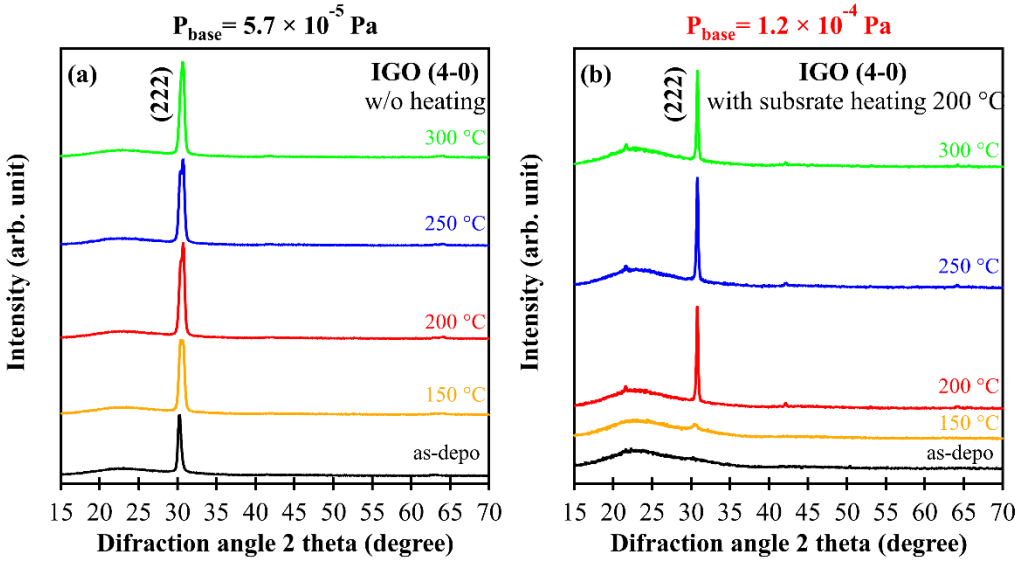

Figure 4.5 XRD diffraction pattern of the IGO film deposited at: (a) room temperature; (b) with substrate heating at 200 °C.

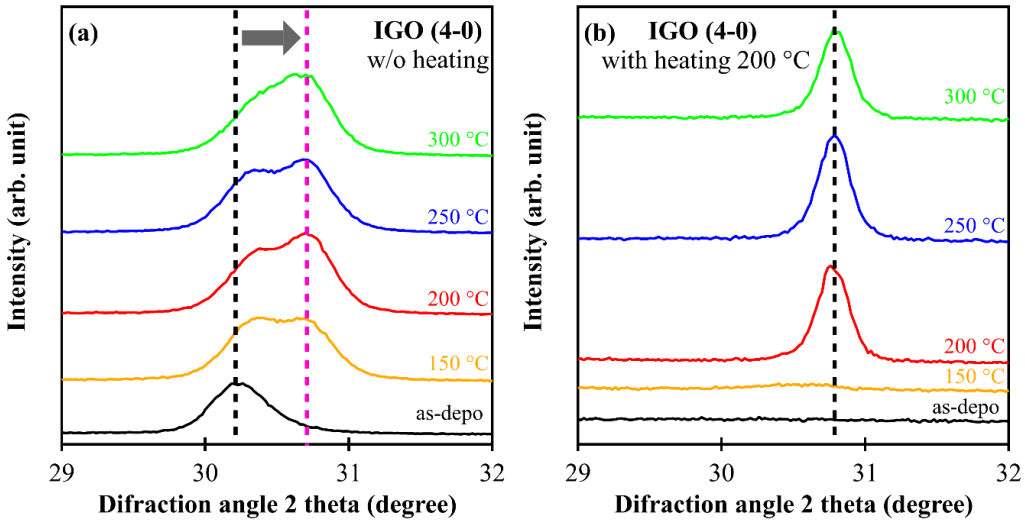

Figure 4.6 XRD diffraction pattern of the main peak along (222) direction of the IGO films: (a) deposited at room temperature; (b) deposited after 2 h substrate heating at 200 °C.

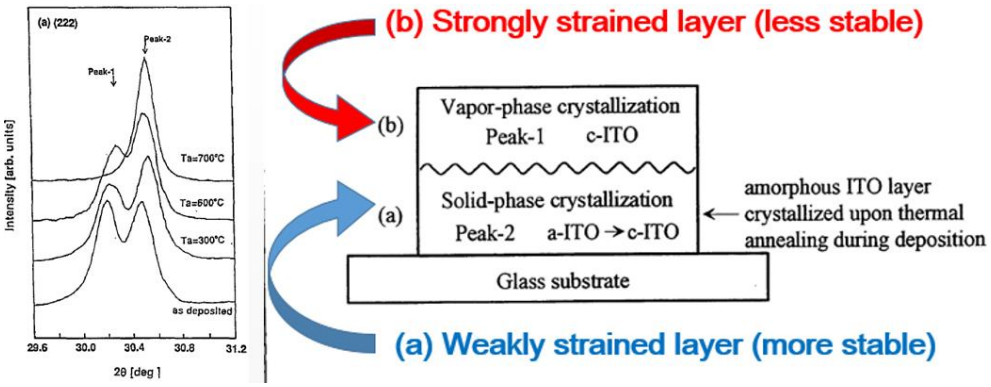

Figure 4.7 (a) XRD peaks of ITO film deposited at 175 °C and post-annealed in air; (b) schematic cross section of ITO films deposited at low substrate temperature [13].

Figure 4.8 shows the XRD diffraction patterns of the hydrogen doped IGO (IGO:H) films deposited at hydrogen ratio of (R[H_2]) of 5% and oxygen ration (R[O_2]) of 4% (sample is denoted as IGO:H (4-5) on the graph). XRD results indicate that H addition during the IGO:H film deposition suppressed the crystallization during the deposition at room temperature, since the clear polycrystalline nature was observed only after annealing at a temperature of 250 °C and above. On the other hand, for the IGO:H deposited on a heated substrate the crystallization was observed at 200 °C. These results clearly show that solid phase crystallization (SPC) was observed at below 250 °C from amorphous to polycrystalline IGO:H.

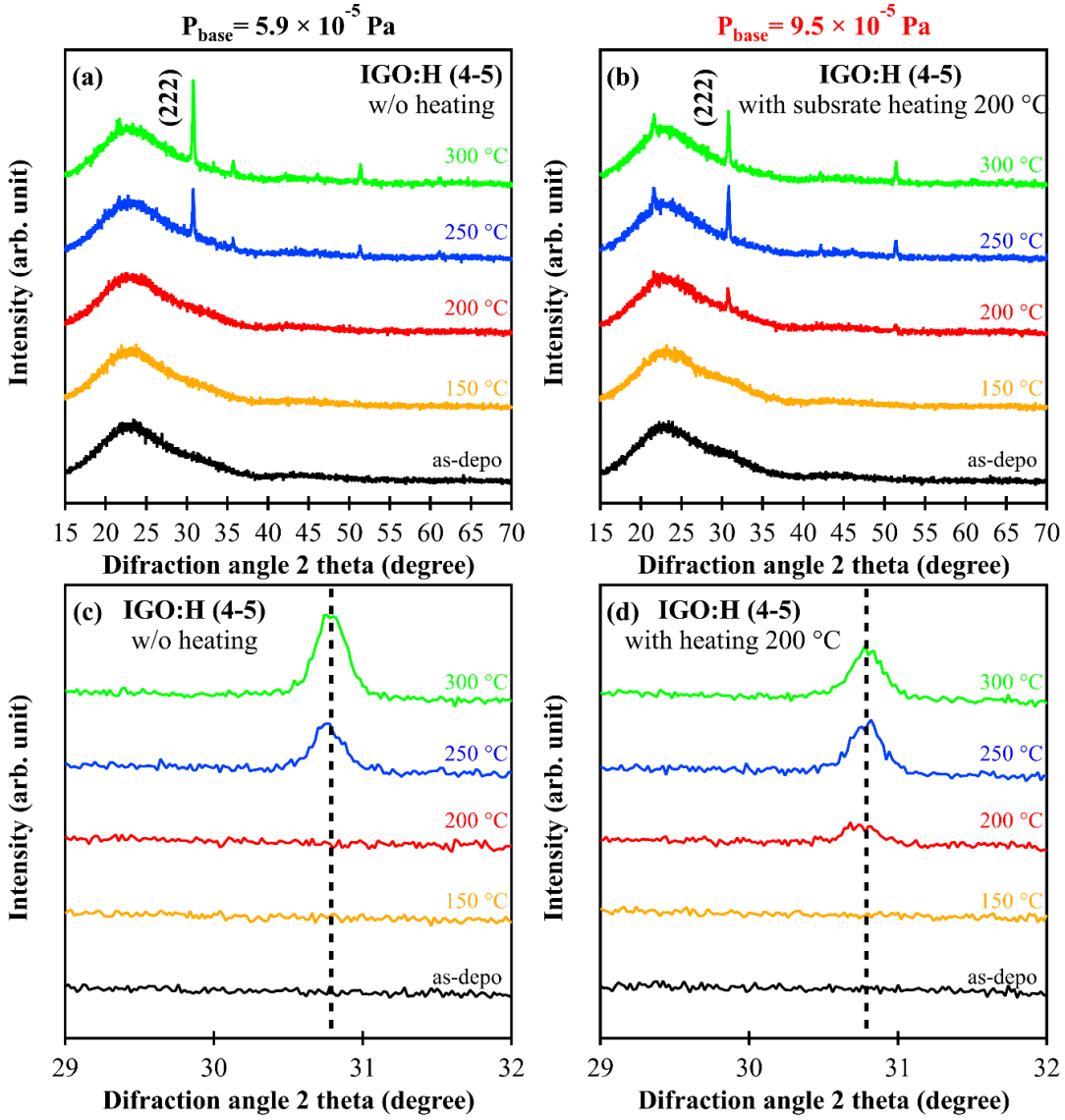

Figure 4.8 XRD diffraction pattern of hydrogen doped IGO films: (a) without substrate heating; (b) with substrate heating; (c) main peak along (222) direction without substrate heating; (d) main peak along (222) direction with substrate heating at 200 °C.

It is known that the deposition of ITO films when water vapor is added leads to suppression of crystallite growth due to passivation by hydrogen of oxygen defects in the amorphous structure. Thus, it impedes the reconstruction and formation of *In-O* bond networks, which ultimately suppresses crystallization [14,15]. On the other hand, the melting temperature of In is relatively low (< 160 °C) and for relatively thin film, this melted In can affect the shift in the crystallization temperature toward the lower region leading to unintentional crystallization even under TEM observation [16]. As a result, this may additionally promote the increase of nuclei density in the initial amorphous film, resulting in lowering of the crystallization temperature, as was found for IGO:H film deposited on heated substrate in Figure 4.8(b). Therefore, XRD results suggest that H incorporation during the deposition can reduce the nuclei density in the as-deposited IGO:H film changing the crystallinity to amorphous. Thus, the effect of Hydrogen has a more significant influence on the onset temperature of crystallization than the deposition on a heated substrate.

Figure 4.9 shows the surface of the IGO and IGO:H films deposited at RT and on heated glass substrate before and after annealing in air using a hot plate analyzed by scanning electron microscope (SEM). All films after deposition showed a smooth and uniform morphology without any significant and obvious boundaries and grains, Figures 4.9(a)-(d). Subsequent annealing with a hot plate up to 200 °C resulted no change in the morphology of the films. Slight noticeable appearance of the grains was observed only for the IGO (4-0) film deposited on heated substrate after annealing at 250 °C. However, the grain size is still small, and boundaries are hardly distinguishable, as can be seen in Figures 4.9(f) and (g). In contrast, the morphology of the IGO:H films changed drastically, as shown in Fig. 4.9(g), (k), (h), (l), due to the strong H effect on the crystallization as was mentioned earlier. Figure 4.9(g) shows that after 1 h of annealing the amorphous phase was still present, but grains were also clearly observed, indicating the difference in the volume fraction of amorphous and crystalline phases in the film. These results additionally suggest that the initial nuclei density decreased after incorporation of H, which promotes the growth of larger grains compared to the conventional IGO film. The average estimated grain size for IGO:H film deposited at RT was 1.6 μm after post-annealing at 300 °C, as shown in Fig. 4.9(k).

However, the grain size of the IGO:H film deposited on the heated substrate was halved to about 0.87 μm, which is the opposite of the expected result, as can be seen in Figure 4.9(l). This decrease in the grain size can be attributed to the increased residual water in the sputtering chamber during the heating process since the base pressure was 9.5×10^{-5} Pa for deposition performed on the heated subsrate than that for RT deposition (5.9×10^{-5} Pa). Therefore additionally changing the initial nuclei density and resulting in the higher volume fraction toward amorphous phase.

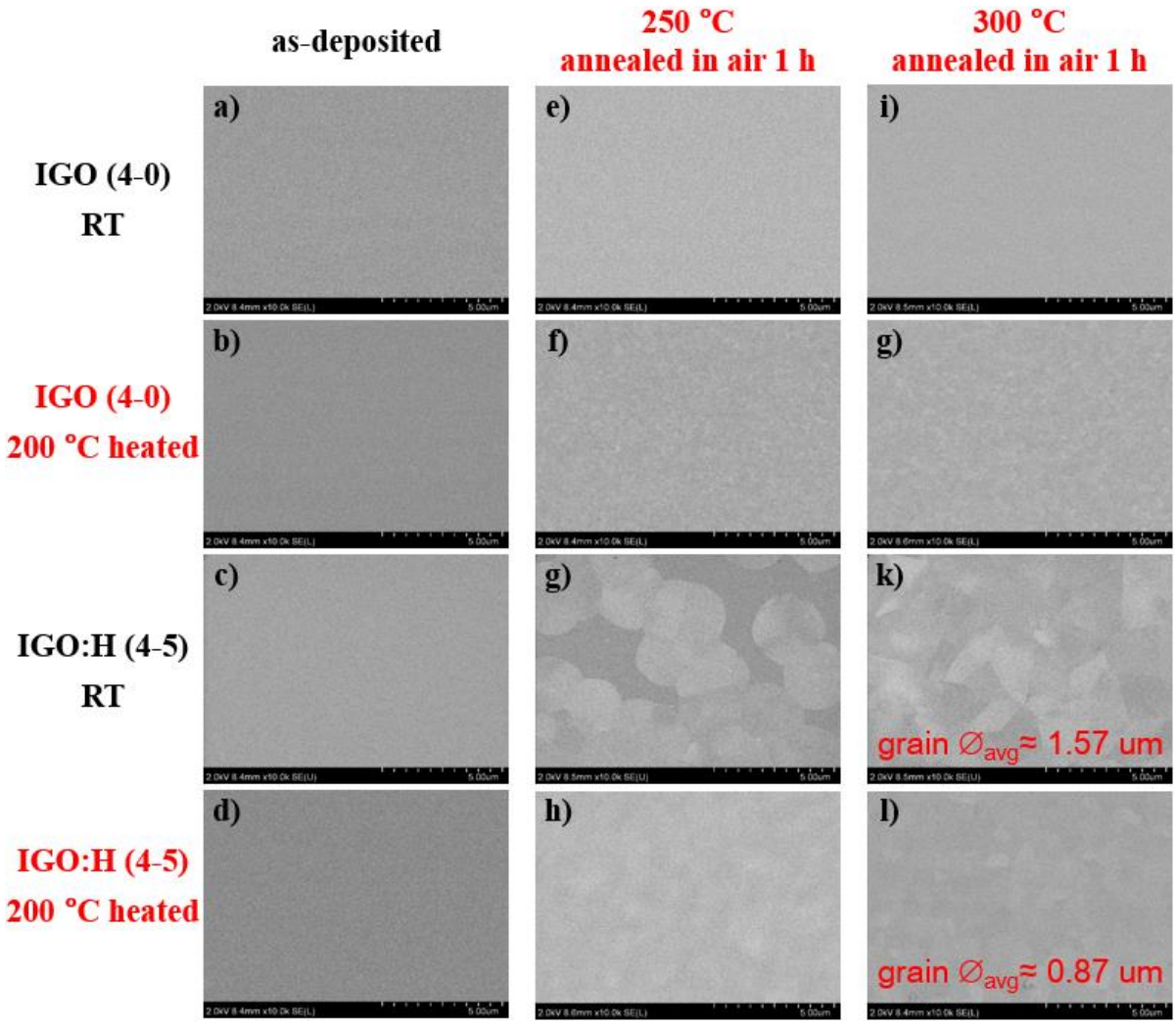

Figure 4.9 SEM images of the IGO (4-0) and IGO:H (4-5) films morphology deposited at room temperature and on heated substrate: (a)-(d) as-deposited; (e)-(h) after 1 h annealing in air at 250 °C; (i)-(l) after 1 h annealing in air at 300 °C.

Figure 4.10 shows the electrical properties variation of IGO and IGO:H films as a function of annealing temperature performed in ambient air for 1 h using a hot plate. As can be seen on Figure 4.10(a), the substrate heating resulted in minor increase of the N_e for conventional IGO

(4-0) film after annealing (i.e. SPC) up to 250 °C. However, after annealing at 300 °C the N_e for IGO (4-0) deposited on heated substrate was 2.0×10^{18} cm^{-3}, which is comparable but slightly less than that of IGO (4-0) deposited at RT (7.1×10^{18} cm^{-3}). In contrast, the obtained Hall mobility (μ_{Hall}) within annealing temperature range up to 250 °C was markedly improved.

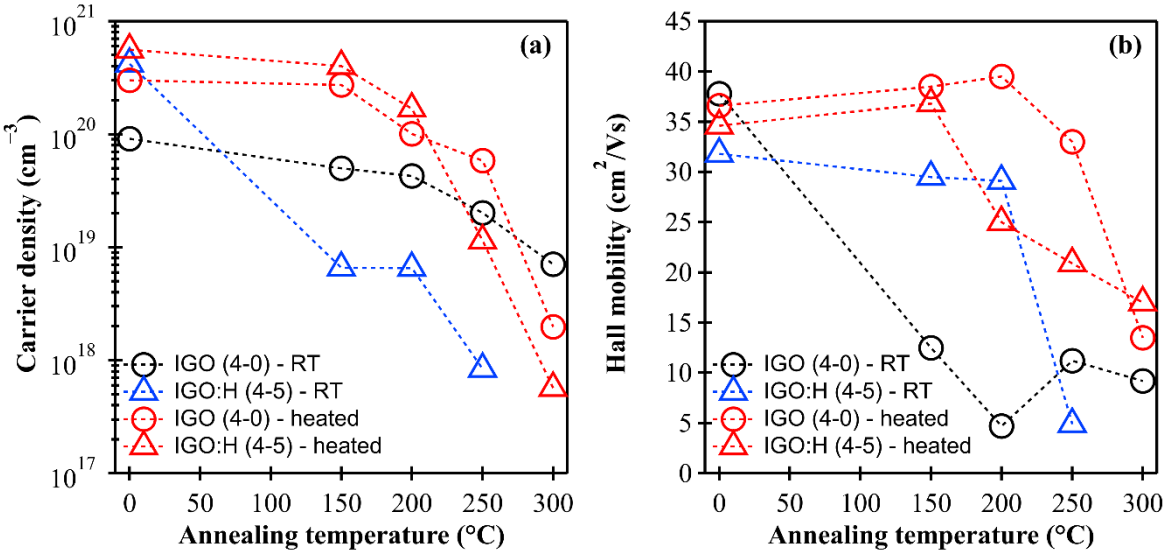

Figure 4.10 Electrical properties of IGO and IGO:H films deposited at RT and on heated glass substrate: (a) carrier density; (b) Hall mobility.

This improvement can be attributed to the lack of the double-peak nature of the main XRD diffraction pattern along (222) direction, as was observed for IGO (4-0) deposited at RT, and discussed earlier in Figure 4.6. Nevertheless, the annealing at 300 °C showed a similar value of 13.5 cm^2/Vs which is slightly higher than 9.2 cm^2/Vs obtained for IGO (4-0) deposited at RT. Regarding the H doped IGO:H film (4-5) deposited on a heated substrate, the N_e was higher over the entire temperature range after annealing and was 5.7×10^{17} cm^{-3} after annealing at 300 °C, while IGO:H deposited at RT showed high resistivity (data not shown). The N_e after annealing at 300 °C is expected to be even lower than for the deposition on heated substrate. These results suggest that the deposition on a heated substrate has almost no effect on the electrical properties and morphology (grain size) for conventional IGO films. At the same time, for the IGO:H films the substrate heating even leads to a decrease in grain size after annealing. Therefore, the conclusions are ambiguous, since the change in the base pressure due to substrate heating additionally introduces inaccuracy into the obtained results.

Next, IGO and IGO:H films were deposited at similar parameters, but using the different equipment with a typical base pressure of ~ 3×10^{-4} Pa in order to establish a more detailed relationship between heating, base pressure, and water vapor. Furthermore, this system (3-inch target ⌀) has a quadrupole mass spectrometer (QMS) for residual gas analysis. Pre-deposition preparation included two main steps: (1) loading the sample into the chamber and subsequent pumping for 1 hour until the base pressure was reached (Stage #1); (2) turning on the substrate heater and waiting for 2 hours to stabilize and normalize the substrate temperature, since heat transfer is problematic in a vacuum (Stage #2). At each stage, changes in residual water gases were analyzed using a spectrometer. Figure 4.11 shows the change in the partial pressure of residual water in the sputtering chamber, starting from the moment of loading the sample into the chamber, and ending with the deposition process after 3 hours.

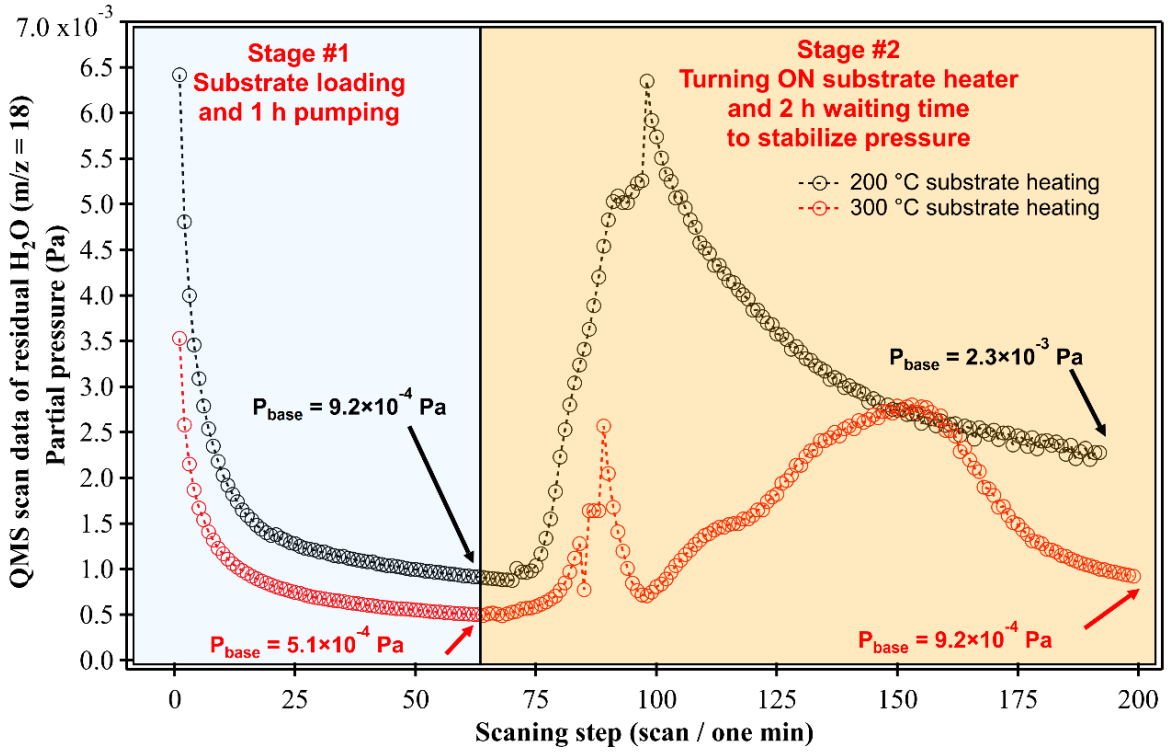

Figure 4.11 Change of the partial pressure of H_2O inside the sputtering chamber prior to IGO film deposition on heated substrate at different temperatures analyzed by using a quadrupole mass spectrometer installed on 3-inch target sputtering equipment.

It can be seen that after loading the sample from the loadlock into the main chamber, the partial pressure of water (P_{H2O}) increased sharply from the atmosphere (Stage #1). Then, during

the next hour of pumping, it sharply decreased and led to a decrease in the P_{base} in the chamber. The corresponding P_{base} in the chamber is shown on the figure. However, it should be noted that the P_{H2O} differs in each particular case. Turning on the heater in the chamber (Stage #2) led to a sharp increase in P_{H2O} to comparable values, as at loading on Stage #1 due to desorption from the inner walls of the vacuum chamber. In addition, even after 2 h of pumping, the P_{base} was not fully recovered. Thus, these results show that the total amount of water involved and participating in the deposition process is higher, which further contributes to the results obtained. Ultimately, this leads to difficulty in drawing unambiguous conclusions, since the substrate heating, the base pressure, and the residual vapor pressure are interrelated with each other.

Figure 4.12 shows the electrical properties of the deposited IGO (4-0) and IGO:H (4-5) film at RT and on heated substrate. Thus, deposition of conventional IGO (4-0) films on the heated substrate led to a significant decrease in carrier density after air annealing for 1 h at 250 and 300 °C, as shown in Figure 4.12(a). The N_e after SPC for 1 h in air at 300 °C was 5.2×10^{19} cm^{-3}, 4.6×10^{17} cm^{-3}, and 3.6×10^{18} cm^{-3} for the IGO (4-0) films deposited at RT, 200 °C, and 300 °C, respectively. The higher N_e for IGO deposited on heated substrate at 300 °C was higher than that of 200 °C, which can be due to the less residual water content in the chamber was revealed by QMS analysis (Figure 4.11). However, μ_{Hall} (Figure 4.12b) practically did not change within entire SPC temperature range and was 9.8, 16.2 and 11.2 cm^2/Vs after SPC at 300 °C for RT, 200 °C, and 300 °C deposition, respectively. The average grain size decreased during both SPC at 300 °C and deposition on heated substrate at 300 °C (set point), as shown in the Figure 4.13(b), (c).

Surprisingly, the deposition of IGO:H (4-5) film on a heated substrate showed the opposite effect. Heating the substrate led to a significant increase in the N_e over the entire SPC temperature range. The N_e after SPC for 1 h in air at 300 °C was higher by three order of magnitude than that for IGO deposited at RT, being 4.7×10^{16} cm^{-3}, 2.2×10^{19} cm^{-3}, and 3.7×10^{19} cm^{-3}, for the IGO:H (4-5) films deposited at RT, 200 °C, and 300 °C, respectively. In contrast, the peak of μ_{Hall} was observed after SPC at 250 °C being 45.1 and 49.6 cm^2/Vs for both IGO:H films deposited on heated substrate at 200 °C, and 300 °C, respectively. Morphology analysis showed no noticeable

differences in the grain size, as shown in Figure 4.14(a) and (c). Therefore, this mobility peak can be attributed to the structural change during the SPC process and increase in the volume fraction of the crystalline phase in the films. Further annealing at 300 °C resulted in a drastic reduction of μ_{Hall} by a factor of three. This decrease can be attributed to the generation of intra-grain defects after crystallization due to desorption of H related species, and decomposition of *In-OH* bonds at higher temperature. As a consequence this may lead to an increase of the scattering centers limiting the mobility by carrier trapping, as was previously reported [8,17].

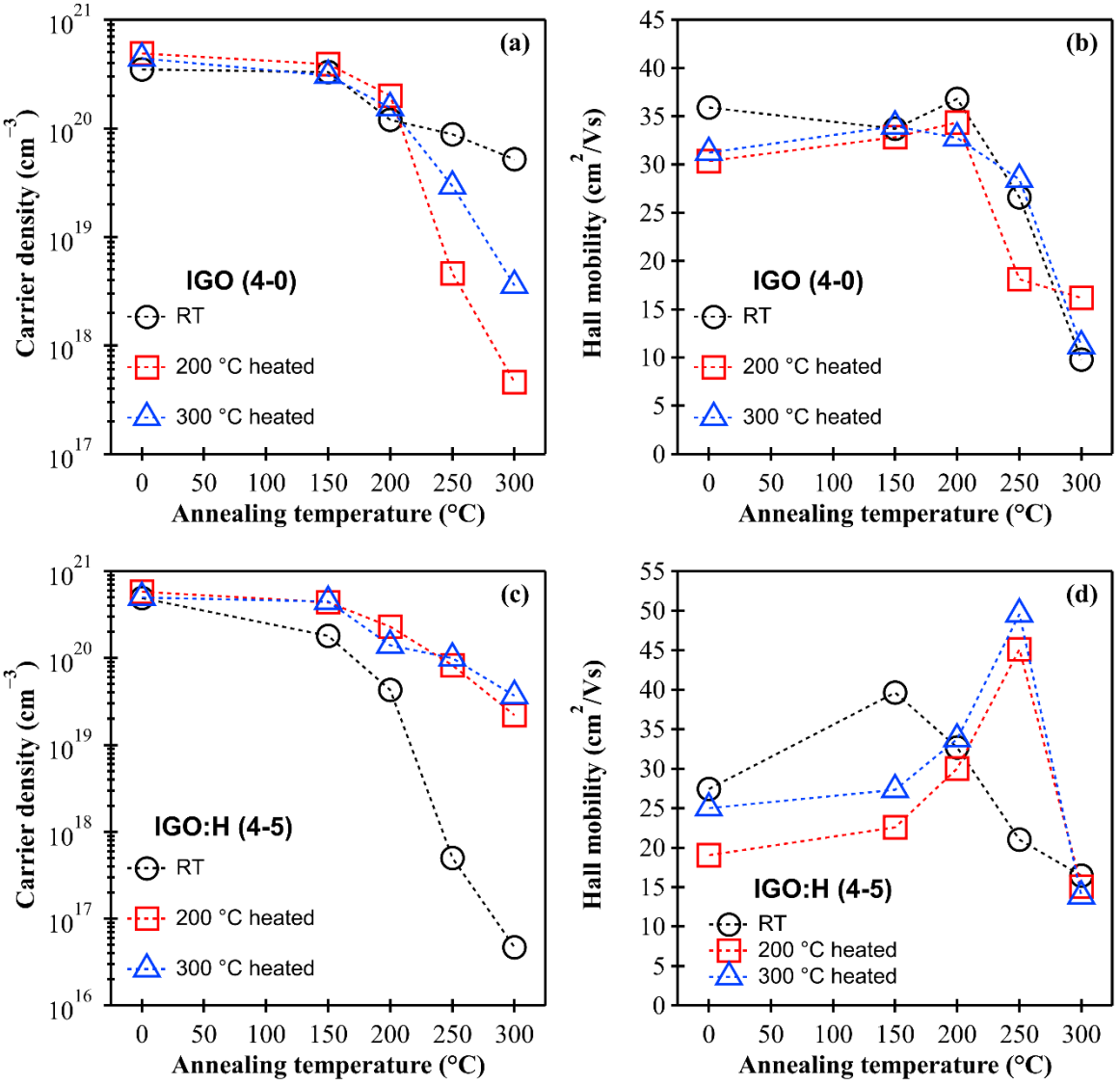

Figure 4.12 Electrical properties of the films deposited at different substrate temperatures as a function of annealing temperature performed in ambient air for 1 h: (a) and (b) conventional IGO film. *Note: Deposition was performed by a 3-inch sputtering tool.*

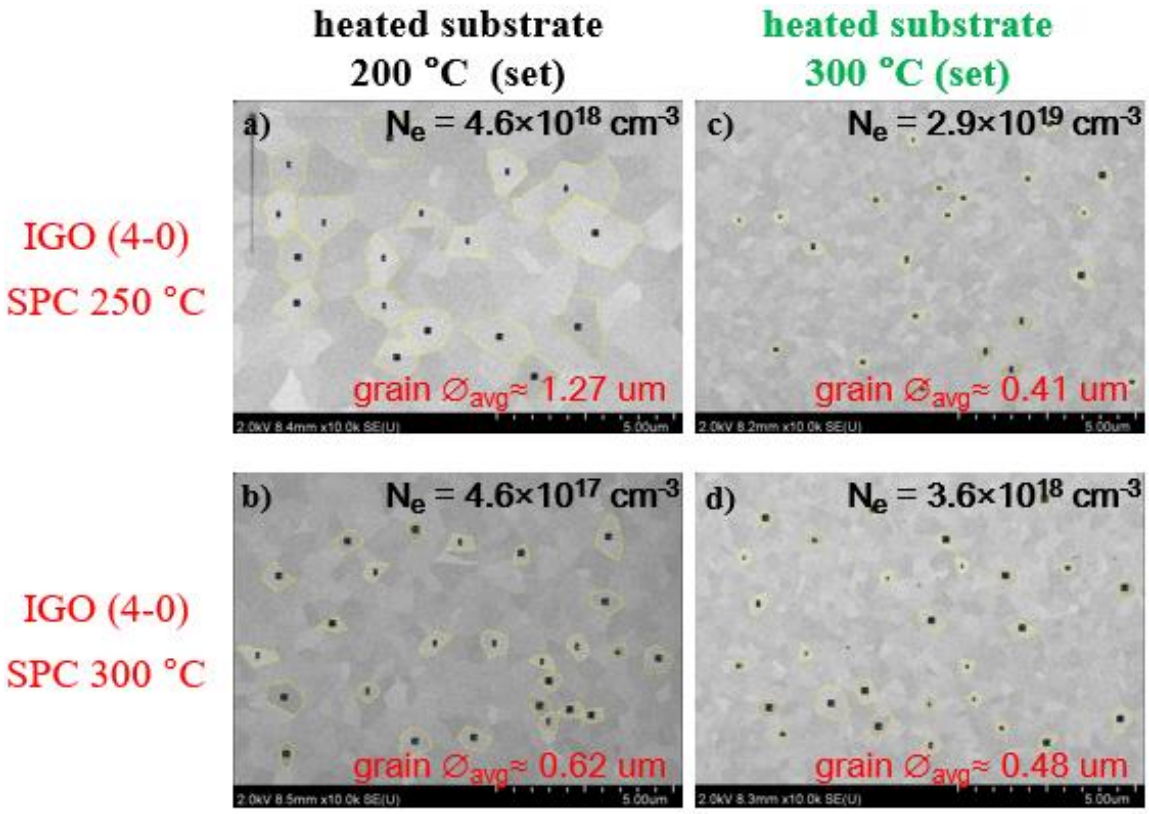

Figure 4.13 SEM images of IGO (4-0) films after SPC at different temperatures on heated substrate at a temperature of: (a) and (b) 200 °C; (c) and (d) 300 °C.

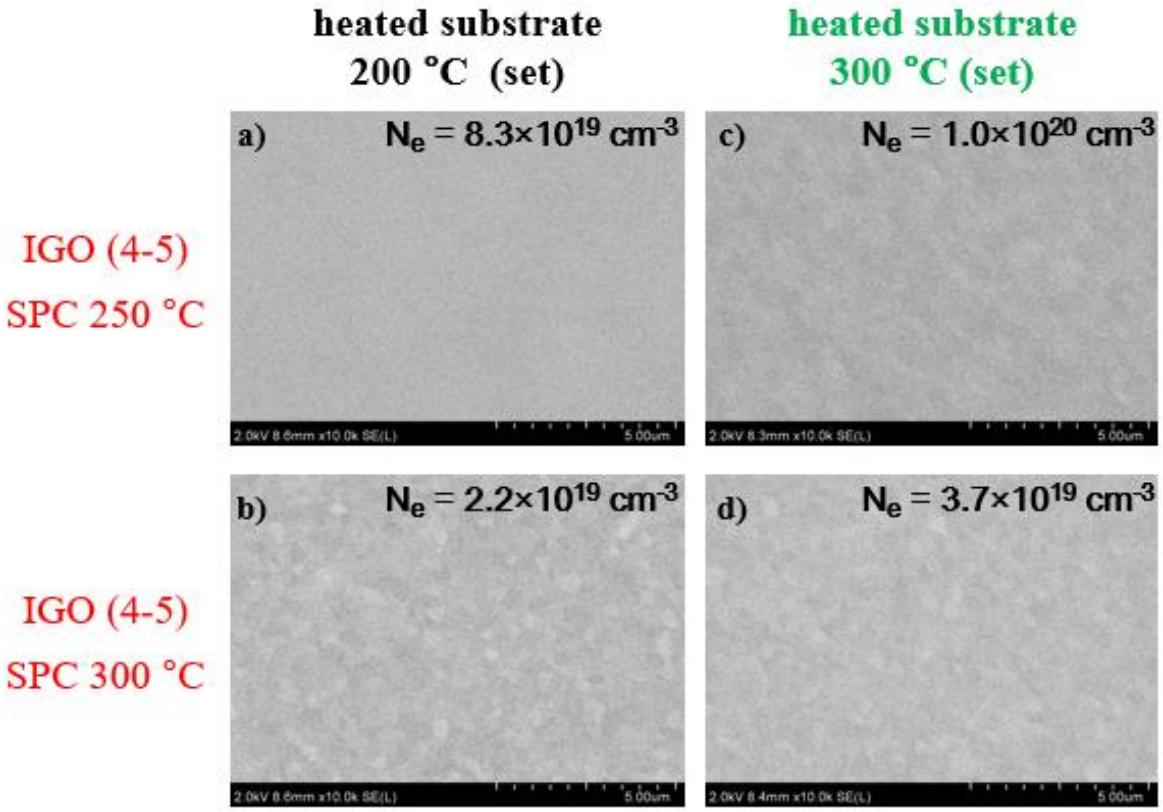

Figure 4.14 SEM images of IGO:H (4-0) films after SPC at different temperatures on heated substrate at a temperature of: (a) and (b) 200 °C; (c) and (d) 300 °C.

Next, deposition of hydrogen-free IGO films (4-0) was carried out to assess the degree of influence of residual water on the film properties. Liquid nitrogen (LN_2) was added to a vacuum trap in order to reduce the base pressure. This trap binds the gas inside the vacuum chamber by condensing gas molecules on its walls. The change in the partial pressure of residual water vapor (P_{H2O}) before and after the addition of LN_2 is shown in Figure 4.15(e). Thus, the use of LN_2 further reduced the P_{H2O} from 1.96×10^{-4} Pa to 1.4×10^{-4} Pa after additional pumping for 1 h. As shown in Figure 4.15(a), film deposited after LN_2 addition showed intensity peak without further SPC, while IGO deposited at normal condition (w/o LN_2) remained amorphous.

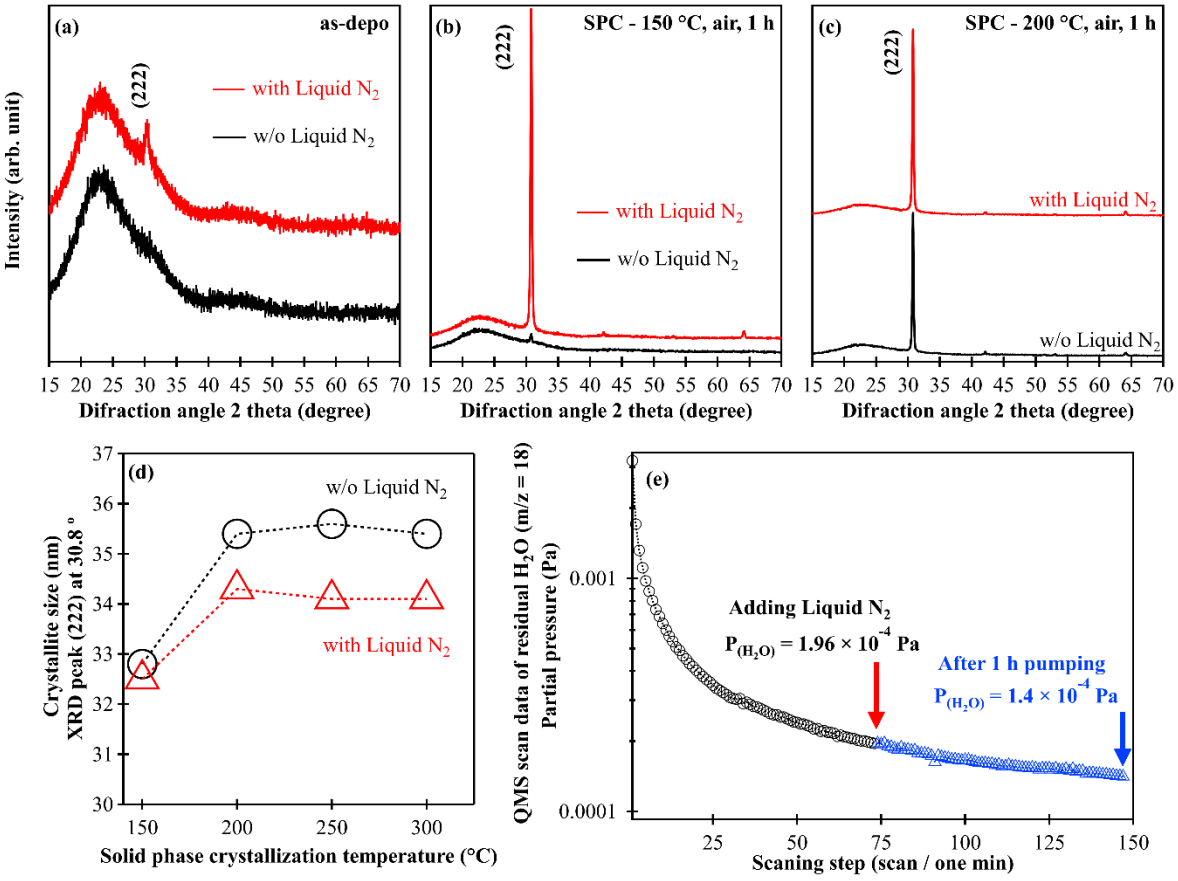

Figure 4.15 IGO (4-0) film deposited at different base pressures. XRD patterns before and after SPC at different temperatures: (a) as-deposited; (b) 150 °C; (c) 200 °C; (d) crystallite size estimated from the Scherrer equation at FWHM of main diffraction peak (222). (e) Change of the P_{H2O} in the sputtering chamber prior to film deposition before and after adding liquid N_2.

All films showed polycrystalline structure after the SPC process at 150 °C and 200 °C, as can be seen in Figure 4.15(b) and (d), respectively. Additionally, deposition at higher P_{H2O} (black color) resulted in a shift in the beginning of the crystallization point to 200 °C because of the

effect of water on the initial density of the nuclei, as discussed earlier. Since the main diffraction peak was observed along orientation (222) at 30.8°, the crystallite size can be estimated by using the Scherrer equation [18,19],

$$D = \frac{K\lambda}{\beta \cos \Theta} \qquad 4.1$$

where D is estimated crystallite size, *K* is a dimension shape factor of crystallite, λ is X-ray wavelength, θ is diffraction peak position, and β is a full-width at half-maximum (FWHM) of the X-ray diffraction peak. For calculation the shape factor K = 0.9 (sphere shape) due to lack of the information about the exact shape was utilized. Calculated crystallite size as a function of SPC temperature is shown in Figure 4.15(d). Thus, the crystallite size for the IGO (4-0) film deposited at low P_{H2O} (red triangle) was lower over the entire SPC temperature range. These results suggest that even a slight change in the base pressure prior to deposition caused by residual water vapor has an effect on grain growth during solid-phase crystallization. In other words, the sensitivity of the *In-O*$_x$ based films is extremely high and must be carefully controlled and taken into account during film synthesis. The electrical properties of the obtained films are shown in Figure 4.16. Thus, both N_e and μ_{Hall} were comparable before and after SPC. However, the IGO film deposited after using a LN_2 trap showed insignificantly lower N_e and μ_{Hall} values.

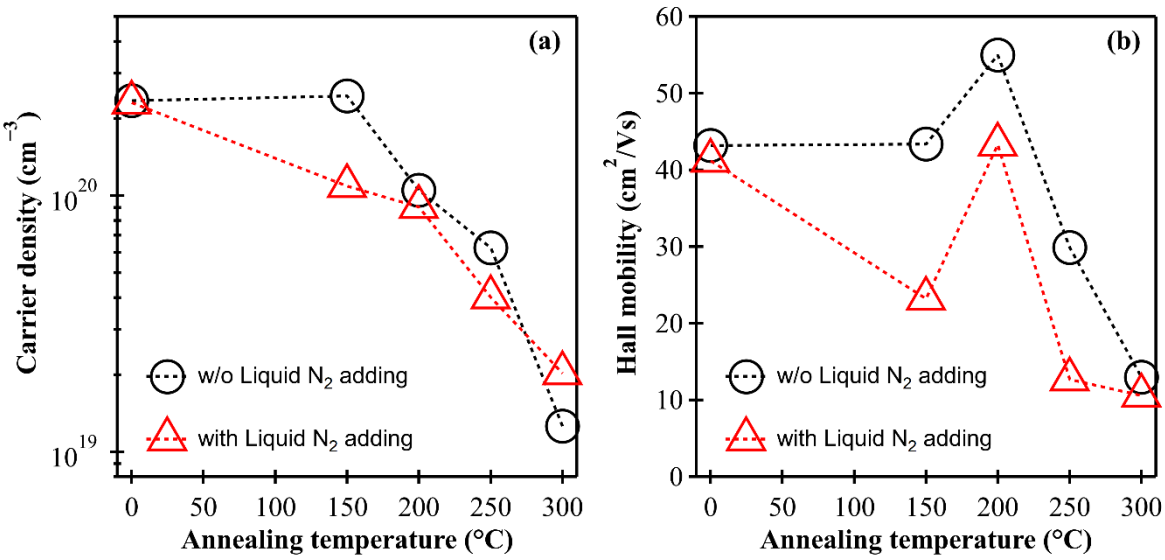

Figure 4.16 Electrical properties of IGO (4-0) film deposited at different partial pressures of water before and after SPC: (a) carrier density; (b) Hall mobility.

These electrical properties are consistent with the observed morphology of the films analyzed by SEM, images of which are shown in Figure 4.17. The grain size for the IGO (4-0) film deposited at high P_{H2O} (w/o LN_2) was slightly higher than that of the film deposited at low P_{H2O} after SPC at 300 °C, Figure 4.17(e) and (f). These results indicate the importance of the residual water vapor control in the sputtering chamber prior to deposition.

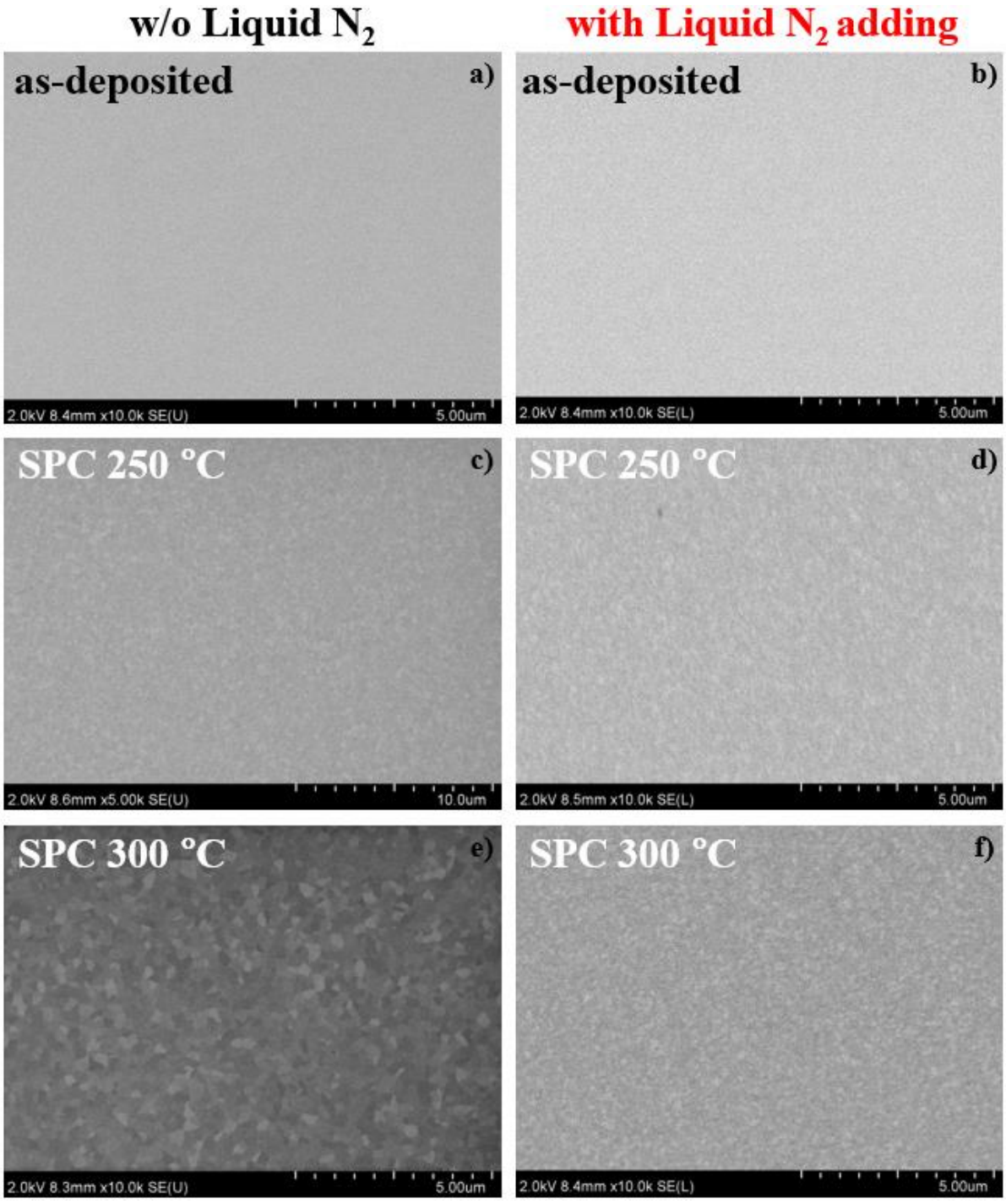

Figure 4.17 SEM images of the IGO (4-0) films before and after SPC: (a), (c), (e) deposited at high P_{H2O}; (a), (c), (e) deposition at low P_{H2O}.

4.3. SiO_2 passivation layer and oxygen plasma treatment effect

The fabrication process of devices involves a varying number of technological steps. Depending on the final structure of the device, the semiconductor channel is subjected to various treatments after crystallization, which can cause unintended changes in the electrical properties. Thus, the study and analysis of the influence of the fabrication steps must be considered when analyzing the performance of the final devices.

In this work, TFTs with a staggered bottom-gate structure by the metal mask process were fabricated including the following technological steps after SPC of the IGO (4-5) channel: formation of the passivating layer of SiO_2 by Plasma-enhanced chemical vapor deposition (PECVD), photolithography and subsequent Inductively Coupled Plasma-Reactive Ion Etching (ICP-RIE) of the SiO_2 layer to form the windows for source and drain deposition. The TFT fabrication process and the state of the conductive channel after SPC are shown in Figure 4.18.

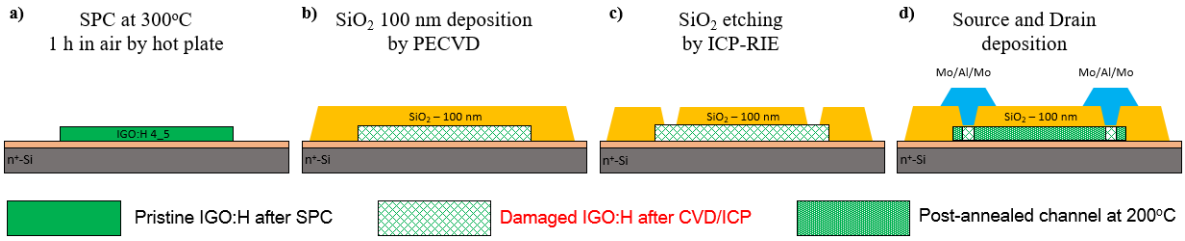

Figure 4.18 Fabrication steps of the IGO:H (4-5) TFT with staggered bottom-gate structure.

First, SiO_2 film is grown by the PECVD system using liquid tetraethoxysilane (TEOS) as a source of Si. Grown is based on the TEOS decomposition in plasma by the following reaction:

$$Si(OC_2H_5)_4 + O_2 \xrightarrow{Plasma\ +\ 180\ ^{\circ}C} SiO_2 + CO_2 \uparrow + H_2O \uparrow \qquad 4.1$$

This reaction suggests that additionally formed H_2O and/or H related species during the SiO_2 layer growth may interact with the IGO:H TFT channel after SPC, while O based plasma radicals can promote film damage and local oxidation. As discussed in the section above, the effect of H_2O in *In-O*$_x$ based materials plays a key role and should be carefully considered. Second, the ICP-RIE takes place in two steps: (i) SiO_2 layer etching by $CF_4 + O_2$ based plasma for 100 nm; (ii) oxygen plasma ashing to remove remained photoresist.

This ashing step can be considered as a local oxidation in the S and D regions of the IGO:H channel as shown in Figure 4.19.

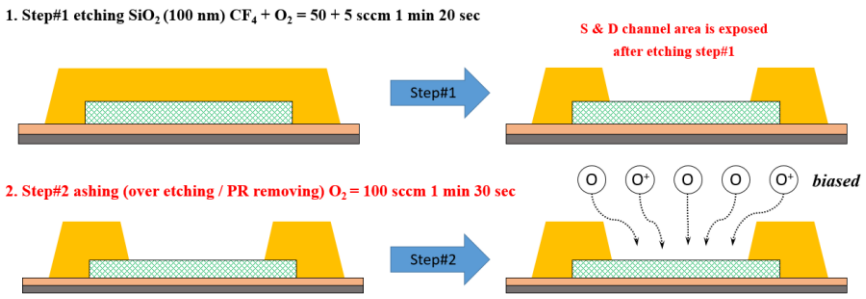

Figure 4.19 ICP-RIE etching two steps process and schematic drawing of the IGO:H channel at TFT source and drain areas after each processing step.

In order to evaluate the possible side effects on the change of conductive IGO:H (4-5) channel properties after SPC at 300 °C, the following plan of experiment was carried out, simulating this impact, and also allowing to separate the result of the impact of each step independently from each other. Since this experiment can be quite complicated to understand, a schematic explanation of the details and approach are presented in Figure 4.20. First, four groups were presented, each representing the possible impact of a different technological process. Group #1 represents the pristine properties of the IGO:H (4-5) film, and which is the reference for comparison. Group #2 samples with a 100 nm thick SiO_2 layer deposited on top of the IGO:H (4-5) film. Group #3 samples with deposited SiO_2 layer with subsequent ICP-RIE etching of the SiO_2. In other words, the surface of the IGO:H (4-5) film was obtained again, but in a renewed form after CVD and ICP-RIE processing. The analysis of this group of samples makes it possible to evaluate what changes occur in the drain and source regions. Finally, group #4 is the IGO:H (4-5) film after oxygen plasma treatment, performed on different equipment to independently evaluate and compare the similarity with etching steps 2 (ashing). This group emulates local channel oxidation in the S & D area during the ashing step by O_2 plasma. For further discussion, all groups are denoted as Ref, CVD, CVD + ICP-RIE, and O_2 plasma for Group #1, #2, #3, and #4, respectively. This was followed by film analysis of each step of the heat treatment to which the TFT is subjected in the manufacturing process: after SPC for 1 h in air at 300 °C, and post-device annealing for 1 h at 200 °C.

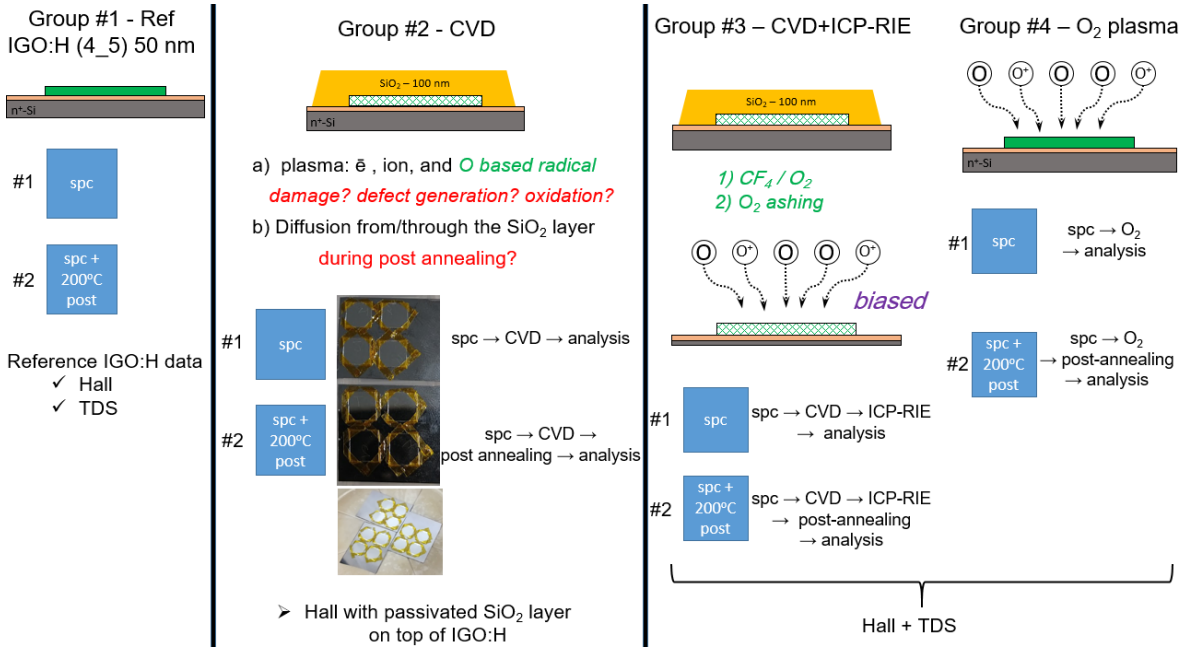

Figure 4.20 Schematic representation of the experimental plan for simulating the effect of technological steps during TFT fabrication on the properties of IGO:H (4-5) film after SPC.

Figure 4.21 shows the electrical properties (Hall mobility vs carrier density) variation of the IGO:H films: (a) film analysis was performed after subsequent processing of the films after SPC at 300 °C for 1 h; (b) film analysis was performed after subsequent processing and post-annealing at 200 °C for 1 h in air of the film after SPC. Results of film analysis after corresponding processing (Fig. 4.21a) indicate the following. First, the CVD process of SiO_2 layer deposition did not affect the electrical properties change, because the N_e for CVD samples (green triangles) slightly decreased in comparison with Ref samples (black circles). In contrast, N_e for the samples both after ICP-RIE and after O_2 plasma treatment increased by 1.5 orders of magnitude, blue and red squares, respectively. This suggests that O incorporation (interstitial) can significantly change the IGO:H film conductivity in the S and D region after ICP-RIE etching. However, the mechanism is not clear and requires further investigation. Second, the slight decrease in N_e for CVD samples can be attributed to H_2O and/or surface defects passivated by H, since the deposition of the SiO_2 layer is TEOS based and involves additional H_2O formation, as reaction 4.1 shows.

As can be seen from Figure 4.21b, an additional post-annealing at 200 °C for 1 h made no change in the electrical properties of the Ref IGO: (4-5) film (black circles). Thus, μ_{Hall} was from 22 to 25 cm^2/Vs, with N_e of ~ 3.5×10^{17} cm^{-3}. In addition, the electrical properties with the 100-

nm thick SiO_2 layer (green triangles in Figure 4.22b) on top of the IGO:H (4-5) also showed slightly lower values similar to film analysis performed without post-annealing (green triangles in Figure 4.22a). On the other hand, the initial N_e increase after O_2 and ICP-RIE plasma treatment disappeared with post-annealing, and those values were recovered to the comparable values of Ref sample, as shown in Figure 4.21b and depicted by red and blue squares.

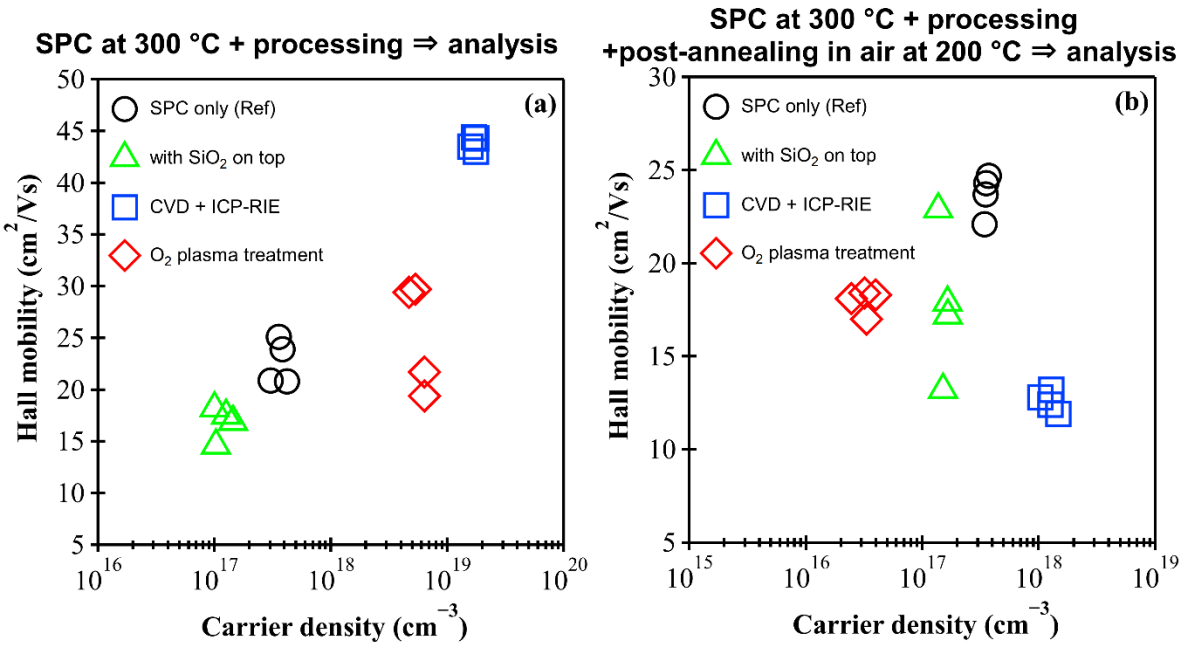

Figure 4.21 Electrical properties of the 50 nm thick IGO:H (4-5) films after SPC at 300 °C for 1 h and analysed after different processing steps: (a) subjected to processing and further analysis; (b) subjected to processing and post-annealing at 200 °C, and only then analysed.

Thermal desorption spectroscopy (TDS) analysis was performed in order to investigate observed electrical properties variation. It was found that desorption of H-related species including H (m/z = 1) and OH (m/z = 17) increased within temperature range from 100 to 600 °C for IGO:H (4-5) film subjected to CVD and ICP-RIE processing prior to analysis (Fig. 4.22a and c). Post-annealing at 200 °C resulted in a decrease in desorption from 100 to 200 °C and was comparable to the Reference IGO:H (4-5). Nevertheless, the residual desorption peak of H-related species was still clearly observed at a high temperature range from 300 to 500 °C (Fig. 4.22d, f), although it was reduced by post annealing. Therefore, this result suggests that TEOS based deposition process of SiO_2 passivation layer promotes intensive formation of H_2O resulting in electrical properties variation of IGO:H channel after SPC. One part of these states is unstable and

are weakly-bonded, and that can be eliminated by post-device-annealing of the fabricated TFT device. By contrast, the other part of the states is more stable and can only be reduced at a higher temperature. This is consistent with the SiO_2 grown reaction 4.1 and observed N_e and μ_{Hall} decrease in Figure 4.21a.

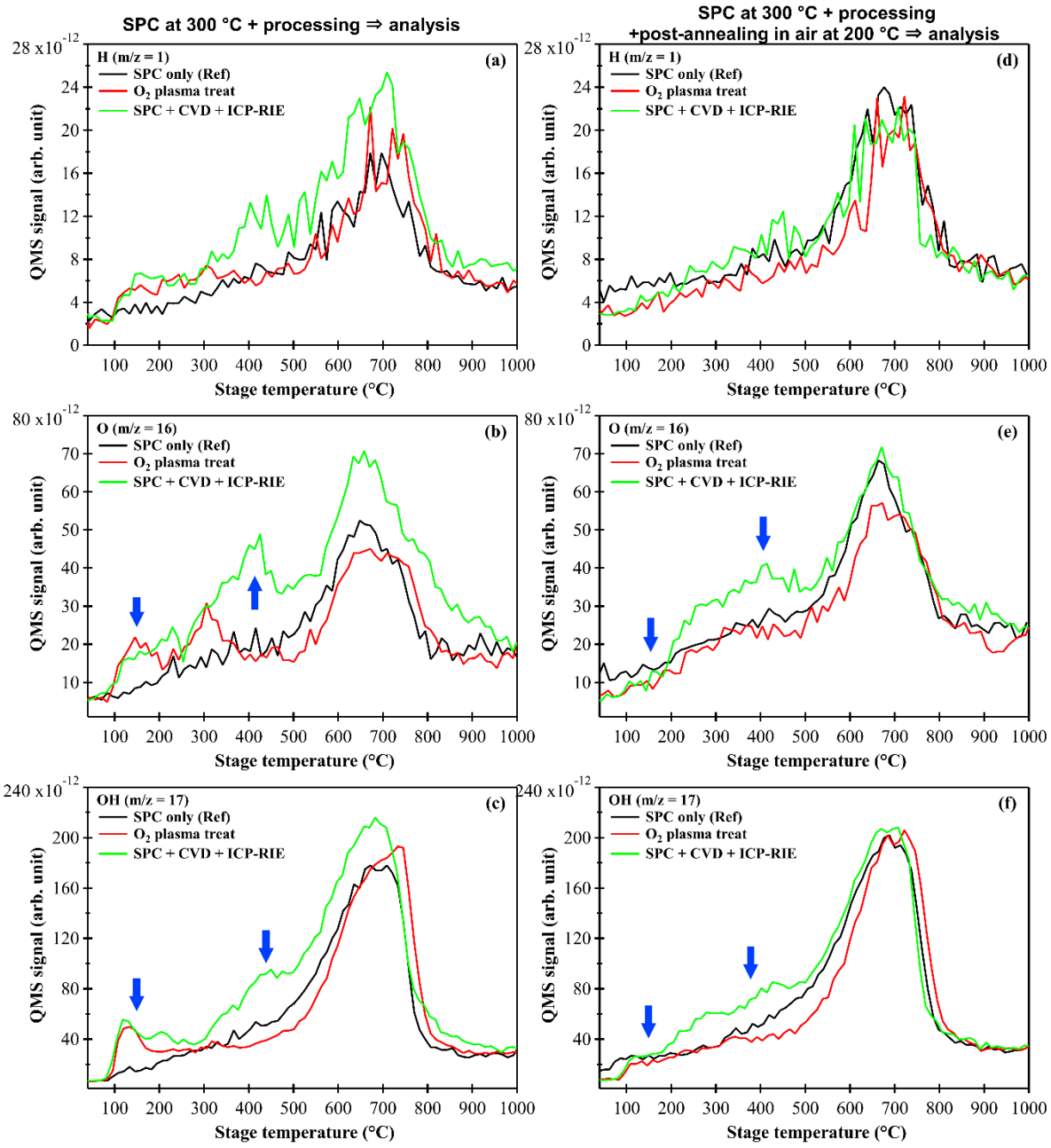

Figure 4.22 TDS analysis of the 50 nm thick IGO:H (4-5) films after SPC at 300 °C and analysed after different processing steps: (a) and (d) m/z = 1 (H); (b) and (e) m/z = 16 (O); (c) and (f) m/z = 17 (OH)

In contrast, analysis of the film after O_2 plasma treatment also revealed a slight increase in O desorption but mostly at low temperatures ranging from 100 to 200 °C (Fig. 4.22b). Whereas

the subsequent annealing at 200 °C resulted in a decrease of this desorption peak (Fig 4.22e). These results suggest that additionally formed oxygen states are not stable and weakly bonded, and that can be successfully removed after post-annealing of the TFT. However, given that the post-annealing is the final fabrication step (after the deposition of the drain and the source contacts), an important question to investigate is how this additionally generated oxygen during ICP-RIE etching (Ashing step#2) affects the properties of both the TFT channel itself in the S-D regions, and the channel-S/D interface. For example, the bottom Mo layer of S and D contact can be unintentionally oxidized. Thus, the question arises about the nature of these states. Are they related to the surface, resulting in passivation and reduction of defects at the grain boundary? On the other hand, can these states penetrate into the bulk structure of the film but have no effect on eliminating defects like oxygen vacancies. Since the opposite trend in N_e was observed.

Next, TFTs using metal mask process were fabricated to check the effect of weakly- and strongly-bonded states formed in consequence of the CVD TEOS deposition process. One TFT was used as a reference for comparison fabricated by standard process, while three other TFTs with additional annealing step for 1 h at 300, 400, and 500 °C next after the 100 nm deposition of the SiO_2 passivation layer. Figure 4.23(a) shows transfer characteristics of the as-fabricated TFT before post-device-annealing. Threshold voltage (V_{th}) of the Ref TFT without additional post-CVD annealing step was below -30 V, while the TFT subjected to post-CVD annealing step at 300 °C showed similar behaviour. In contrast, V_{th} of the TFTs annealed after CVD at higher temperature of 400 and 500 °C markedly improved being approximately -9 V and -7 V, respectively. In addition, subthreshold swing (S.S.) and hysteresis also improved. As-fabricated TFT transfer characteristics are summarized in Table 4.2. These results suggest that the TEOS-based SiO_2 deposition CVD process leads to an unintended increase of the IGO channel conductivity. Presumably, this increase can be attributed to the additional diffusion of H, which acts as a donor in oxide semiconductors. On the other hand, since one of the main drawbacks of the TEOS process is the formation of water vapor, it implies that H_2O can adsorb on the surface of the IGO which results in the formation of a thin conductive layer. In addition, it is known that low-temperature TEOS

CVD also results in significant incorporation of the residual silanol (Si-OH) and H_2O into the as-deposited film [20–22]. Therefore, it may lead to the current flow mainly through the back channel (IGO – SiO_2 interface), while annealing after CVD allows to improve the transfer characteristics of the TFT presumably due to removal of the residual hydroxyl moieties, and that improving the back channel interface. Thus, given the sensitivity of the *In-O*$_x$ based OS to H_2O and the obtained TFT transfer characteristics, careful optimization of the parameters of the SiO_2 deposition by low-temperature TEOS-based PECVD process is necessary to determine a more detailed mechanism of influence on the properties of the IGO:H TFT channel.

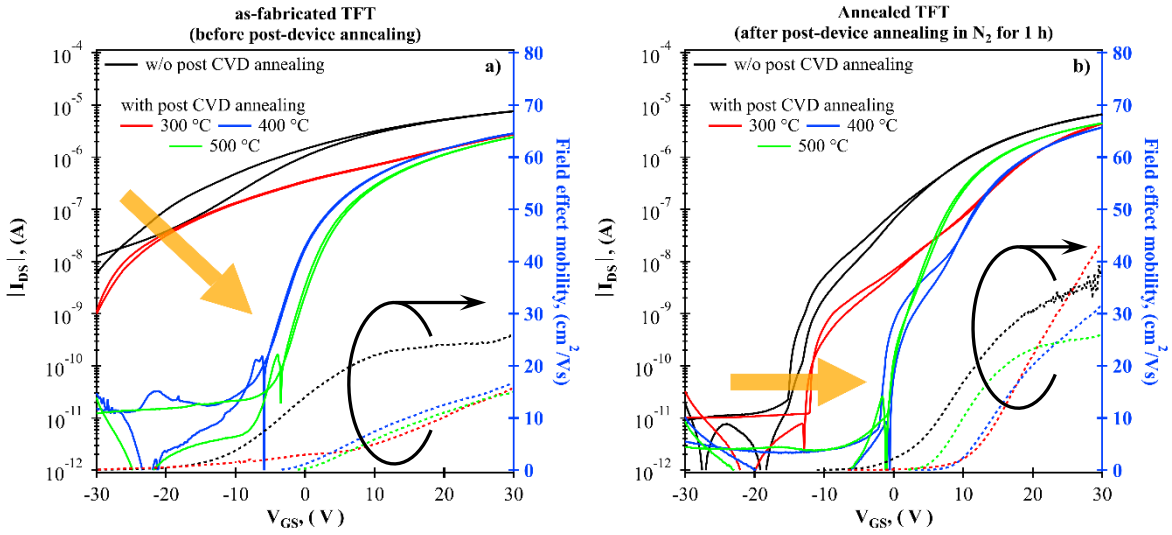

Figure 4.23 Transfer characteristics of SPC-IGO:H (4-5) TFT fabricated with and without post-CVD annealing: (a) as-fabricated; (b) after post-device annealing at 200 °C for 1 h in N_2.

Table 4.2 Summary of electrical properties of as-fabricated SPC-IGO:H (4-5) TFTs.

Post-CVD annealing temperature (°C)	μ_{FE} (cm^2/Vs)	S.S. (V/dec.)	V_{th} (V)
w/o	26.2	–	< - 30
300	15.8	–	< - 30
400	16.9	6.1	- 9
500	15.1	3.2	- 7

Post-device annealing at 200 °C for 1 h in N_2 improved the transfer characteristics of the all TFTs (Fig. 4.23b), indicating defects reduction generated during the ICP-RIE etching step in

the S and D regions. The best performance was shown by the TFT subjected to the post-CVD annealing at 500 °C, while other TFTs showed hump behaviour and deterioration of hysteresis. TFT transfer characteristics after final annealing are summarized in Table 4.3. However, despite the improvement achieved by the additional annealing step after the CVD, a trade-off between the temperature and μ_{FE} was found.

Table 4.3 Summary of SPC-IGO:H (4-5) TFTs properties after PDA at 200 °C for 1 h in N_2.

Post-CVD annealing temperature (°C)	μ_{FE} (cm^2/Vs)	S.S. (V/dec.)	V_{th} (V)
w/o	45.5	hump	~ - 15
300	43.5	hump	~ - 12
400	31.6	hump	- 0.5
500	26.2	0.4	~ - 3.5

Several possible causes of the hump phenomena in oxide-based TFT have been reported by theoretical and experimental studies [23–25]. Therefore, hump phenomena is typically attributed to the two possible reasons namely (i) shallow donor defects states near the conduction band minimum (CBM) [26], (ii) abnormal current flow by two or more paths, especially at a back-channel interface [27]. 3D Atlas technology computer-aided design device simulation results revealed that the presence of a parasitic conductive channel in the active layer near the back-channel leads to a change in current density. Moreover, the current predominantly flows through this parasitic channel with higher conductivity than the bulk region [26]. Therefore, the contamination or damage occurring during the TFT fabrication process can lead to the formation of the parasitic conductive channel. These TCAD simulation results are consistent and support the observed variation in both film and TFTs properties shown in Figures 4.22, 4.23, and 4.24.

Lastly, it is also worth noting that despite the found effect of the SiO_2 passivation layer deposition on the IGO:H (4-5) channel electrical properties variation, which can be partially minimized by the introduction of an additional annealing step after deposition, the reproducibility and repeatability of the IGO:H TFT results requires further improvement and research.

Figure 4.24 shows the transfer characteristics of the SPC-IGO:H TFT fabricated with the same metal mask process as was shown in Figure 4.19, but without the introduction and use of

an additional annealing step after CVD. Thus, comparable and suitable TFT characteristics can be obtained without an additional annealing step. The μ_{FE}, S.S value, and V_{th} of as-fabricated TFT were 59.9 cm^2/Vs, 0.3 V/dec., and -13 V, respectively (Fig. 4.24a). Nevertheless, the final post-device annealing step (Fig. 4.24b) is necessary to reduce V_{th} and improve S.S. value, which were -2.7 V and 0.04 V/dec., respectively. These results suggest that the TEOS-based CVD process has a significant impact on the final performance characteristics of the IGO:H TFT even after crystallization. In other words, the optimization of the IGO fabrication process requires careful analysis and approach. In addition, the optimized process for IGZO cannot be fully implemented due IGO sensitivity especially for H_2O. On the other hand, another possible cause of such TFT properties variations could be contamination of the IGO target. Thus, film deposition was performed by magnetron sputtering with a multi-cathode configuration, where the deposition of other materials (especially metals) could lead to the contamination of the IGO target by by-products. This, in turn, can lead to changes in the crystallization process during SPC. This issue requires further research, analysis, and optimization.

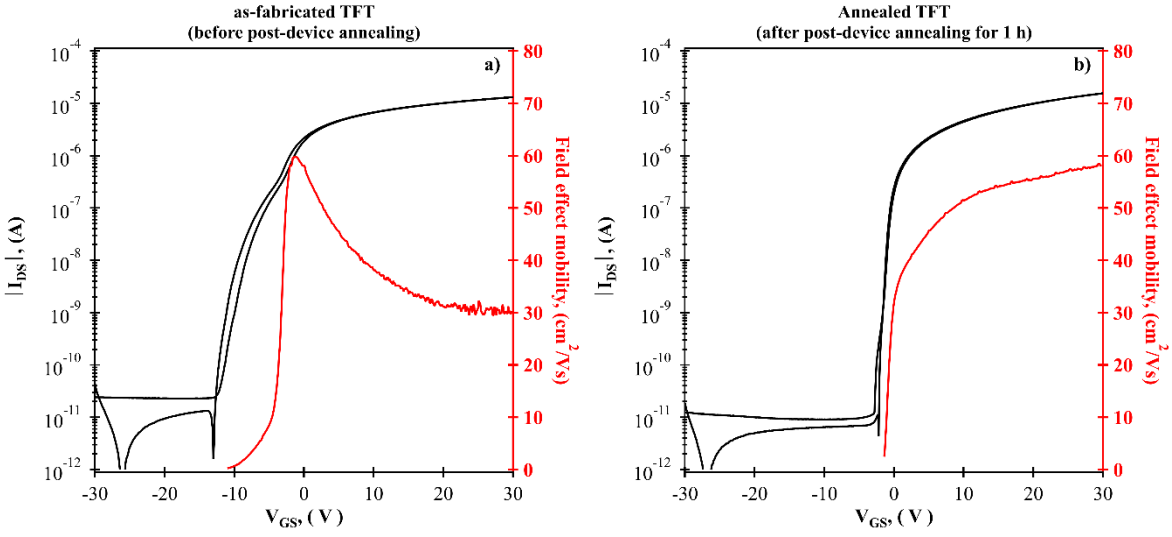

Figure 4.24 Transfer characteristics of SPC-IGO:H (4-5) TFT at V_{DS} = 0.1 V fabricated without post-CVD annealing: (a) as-fabricated; (b) after annealing for 1 h.

4.4. Conclusion

1. The effects of deposition of IGO and IGO:H films on a heated substrate, deposition at different base pressures were investigated. It was found that deposition on a heated substrate has barely any effect on grain size growth during SPC. Nevertheless, a slight increase in N_e and μ_{Hall} was still observed after SPC for hydrogen-doped IGO films, while the values after SPC at 300 °C were comparable to that for conventional IGO deposited at room temperature.
2. On the other hand, deposition on a heated substrate leads to an increase in the base pressure due to desorption from the inner walls of the vacuum chamber. This, in turn, leads to an increase in residual water vapor, which introduces additional inaccuracies due to stronger effect of the H and H_2O on the properties than substrate heating.
3. Analysis of conventional IGO films deposited at RT but at different partial pressures of residual water vapor (P_{H2O}) showed a variation in crystallite size and electrical properties. Thus, the film deposited at low $P_{H2O} = 1.4\times10^{-4}$ Pa with the use of a liquid nitrogen trap showed decrease in crystallite size by 1-3% in comparison with deposition performed at $P_{H2O} = 1.96\times10^{-4}$ Pa. The N_e and μ_{Hall} values were comparable, but still slightly lower for low P_{H2O} deposition. These results indicate the importance of the residual water vapor control in the sputtering chamber prior to deposition.
4. Due to the sensitivity of *In-O_x* based materials to residual water, direct transfer of established and optimal parameters of the IGO film synthesis from one equipment to another is limited and requires a separate optimization and selection. As was found during investigating the influence of the base pressure by deposition using equipment with different vacuum systems with P_{base} of 1×10^{-4} Pa and 5×10^{-4} Pa, while other parameters were fixed.
5. A study of the side effects of the SiO_2 passivation layer deposition and oxygen plasma treatment revealed the electrical properties variation of the IGO:H films after SPC. It was found that a TEOS-based CVD deposition of a SiO_2 layer tends to form weakly- and strongly-bonded H states at low (100-200 °C) and high-temperature range (300-500 °C), respectively.

6. These states originated from a major drawback: a low-temperature TEOS CVD with significant incorporation of the residual Si-OH and H_2O into the SiO_2 layer. These states can be considered as a source of unintentional H doping, which can diffuse into the IGO film. On the other hand, adsorbed H_2O on the surface of the IGO may affect the back-channel interface. Thus, the formed unintentional parasitic channel with higher conductivity eventually changes the current flow and deteriorates the TFT transfer characteristics.
7. Additional post-CVD annealing step can reduce these states resulting in a decrease in V_{th} from < -30 V to approximately -7 V for the as-fabricated TFTs. However, a trade-off was found, higher post-CVD annealing temperature improved the V_{th} and S.S., but reduced the μ_{FE} from 45.5 to 26.2 cm^2/Vs.
8. It was found that the repeatability and reproducibility of the obtained TFT characteristics depend on the SiO_2 deposition process. Thus, it is possible to obtain acceptable TFT transfer characteristics with μ_{FE}, V_{th}, and S.S. of 60 cm^2/Vs and - 2.7 V, and 0.04 V without additional annealing after the SiO_2 CVD process, respectively. These results show that the sensitivity of the IGO films to the TEOS process is higher than that of the IGZO. Therefore, the IGO:H based TFT fabrication process require separate optimization.
9. Oxygen plasma treatment significantly increases the N_e of the IGO:H film even after SPC. TDS analysis revealed an increase of oxygen (m/z = 16) desorption in the low temperature range of 100-200 °C. These states are weakly-bonded and can be effectively terminated by annealing at 200 °C, followed by a decrease in the N_e. However, further study of this phenomenon is required. First, whether they are surface states and affect only defects associated with grain boundaries or also affect the bulk defects such as oxygen vacancies. Second, how does this excess of oxygen affect the IGO:H-Source/Drain interface, as the final annealing is performed on the fabricated device. Consequently, this fact can lead to oxidation of the lower Mo layer of Mo/Al/Mo stack S and D contacts during post-device annealing.

References

1. Kamiya, T.; Hosono, H. Material characteristics and applications of transparent amorphous oxide semiconductors. *NPG Asia Mater.* **2010**, *2*, 15–22, doi:10.1038/asiamat.2010.5.
2. Lee, S.Y. Comprehensive Review on Amorphous Oxide Semiconductor Thin Film Transistor. *Trans. Electr. Electron. Mater.* **2020**, *21*, 235–248, doi:10.1007/s42341-020-00197-w.
3. Diego, S. Fundamental and recent progress in p-channel oxide-TFT development.
4. Weiher, R.L. Electrical properties of single crystals of indium oxide. *J. Appl. Phys.* **1962**, *33*, 2834–2839, doi:10.1063/1.1702560.
5. Noh, J.H.; Ryu, S.Y.; Jo, S.J.; Kim, C.S.; Sohn, S.W.; Rack, P.D.; Kim, D.J.; Baik, H.K. Indium oxide thin-film transistors fabricated by RF sputtering at room temperature. *IEEE Electron Device Lett.* **2010**, *31*, 567–569, doi:10.1109/LED.2010.2046133.
6. Buchholz, D.B.; Ma, Q.; Alducin, D.; Ponce, A.; Jose-Yacaman, M.; Khanal, R.; Medvedeva, J.E.; Chang, R.P.H. The structure and properties of amorphous indium oxide. *Chem. Mater.* **2014**, *26*, 5401–5411, doi:10.1021/cm502689x.
7. Koida, T.; Fujiwara, H.; Kondo, M. Hydrogen-doped in2O3 as high-mobility transparent conductive oxide. *Japanese J. Appl. Physics, Part 2 Lett.* **2007**, *46*, doi:10.1143/JJAP.46.L685.
8. Koida, T.; Kondo, M.; Tsutsumi, K.; Sakaguchi, A.; Suzuki, M.; Fujiwara, H. Hydrogen-doped In2O3 transparent conducting oxide films prepared by solid-phase crystallization method. *J. Appl. Phys.* **2010**, *107*, doi:10.1063/1.3284960.
9. Ebata, K.; Tomai, S.; Tsuruma, Y.; Iitsuka, T.; Matsuzaki, S.; Yano, K. High-mobility thin-film transistors with polycrystalline In-Ga-O channel fabricated by DC magnetron sputtering. *Appl. Phys. Express* **2012**, *5*, doi:10.1143/APEX.5.011102.
10. Rozati, S.M. The effect of substrate temperature on the structure of tin oxide thin films obtained by spray pyrolysis method. *Mater. Charact.* **2006**, *57*, 150–153, doi:10.1016/j.matchar.2005.12.019.
11. Ikhmayies, S.J. The Influence of the Substrate Temperature on the Properties of Solar Cell Related Thin Films. *Mod. Asp. Bulk Cryst. Thin Film Prep.* **2012**, doi:10.5772/29646.
12. Simdar, M.; Mousavi, S.S.; Sajad, B.; Hassani, F. Distinctive ZnO film's structures and morphologies for different modes of the heating substrate. *Mater. Lett.* **2021**, *297*, 129914, doi:10.1016/J.MATLET.2021.129914.
13. Journal, J.; You, A.P. Microstructure of Low-Resistivity Tin-Doped Indium Oxide Films Deposited at 150 ~ 200 ° C. **1995**.

14. Ishibashi, S.; Higuchi, Y.; Ota, Y.; Nakamura, K. Low resistivity indium–tin oxide transparent conductive films. I. Effect of introducing H 2 O gas or H 2 gas during direct current magnetron sputtering . *J. Vac. Sci. Technol. A Vacuum, Surfaces, Film.* **1990**, *8*, 1399–1402, doi:10.1116/1.576889.

15. Ando, M.; Takabatake, M.; Nishimura, E.; Leblanc, F.; Onisawa, K.I.; Minemura, T. Roles of bonded hydrogens and oxygen vacancies on crystallization of hydrogenated amorphous indium tin oxide (a-ITO:H) films. *J. Non. Cryst. Solids* **1996**, *198–200*, 28–32, doi:10.1016/0022-3093(95)00648-6.

16. Muydinov, R.; Steigert, A.; Wollgarten, M.; Michalowski, P.P.; Bloeck, U.; Pflug, A.; Erfurt, D.; Klenk, R.; Körner, S.; Lauermann, I.; et al. Crystallisation phenomena of In 2 O 3 :H films. *Materials (Basel).* **2019**, *12*, doi:10.3390/ma12020266.

17. Koida, T. Amorphous and crystalline In2O3-based transparent conducting films for photovoltaics. *Phys. Status Solidi Appl. Mater. Sci.* **2017**, *214*, doi:10.1002/pssa.201600464.

18. Scherrer, P. Bestimmung der inneren Struktur und der Größe von Kolloidteilchen mittels Röntgenstrahlen. *Kolloidchem. Ein Lehrb.* **1912**, *277*, 387–409, doi:10.1007/978-3-662-33915-2_7.

19. Langford, J.I.; Wilson, A.J.C.; IUCr Scherrer after sixty years: A survey and some new results in the determination of crystallite size. *urn:issn:0021-8898* **1978**, *11*, 102–113, doi:10.1107/S0021889878012844.

20. Shareef, I.A.; Rubloff, G.W.; Anderle, M.; Gill, W.N.; Cotte, J.; Kim, D.H. Subatmospheric chemical vapor deposition ozone/TEOS process for SiO2 trench filling. *J. Vac. Sci. Technol. B Microelectron. Nanom. Struct.* **1995**, *13*, 1888–1892, doi:10.1116/1.587830.

21. Deshmukh, S.C. Investigation of low temperature SiO2 plasma enhanced chemical vapor deposition. *J. Vac. Sci. Technol. B Microelectron. Nanom. Struct.* **1996**, *14*, 738, doi:10.1116/1.588707.

22. Romet, S.; Couturier, M.F.; Whidden, T.K. Modeling of Silicon Dioxide Chemical Vapor Deposition from Tetraethoxysilane and Ozone. *J. Electrochem. Soc.* **2001**, *148*, G82, doi:10.1149/1.1342186.

23. Jeong, C.Y.; Lee, D.; Song, S.H.; Kim, J.I.; Lee, J.H.; Kwon, H.I. A study on the degradation mechanism of InGaZnO thin-film transistors under simultaneous gate and drain bias stresses based on the electronic trap characterization. *Semicond. Sci. Technol.* **2014**, *29*, 045023, doi:10.1088/0268-1242/29/4/045023.

24. Cho, Y.J.; Lee, Y.H.; Kim, W.S.; Kim, B.K.; Park, K.T.; Kim, O. Effect of illumination on the hump phenomenon in I–V characteristics of amorphous InGaZnO TFTs under positive gate-bias stress. *Phys. Status Solidi Appl. Mater. Sci.* **2017**, *214*, doi:10.1002/pssa.201600503.

25. Nomura, K.; Kamiya, T.; Hirano, M.; Hosono, H. Origins of threshold voltage shifts in room-temperature deposited and annealed a-In-Ga-Zn-O thin-film transistors. *Appl. Phys. Lett.* **2009**, *95*, 1–4, doi:10.1063/1.3159831.

26. Lee, H.J.; Abe, K.; Noh, H.Y.; Kim, J.S.; Lee, H.; Lee, M.J. Analysis of the hump phenomenon and needle defect states formed by driving stress in the oxide semiconductor. *Sci. Rep.* **2019**, *9*, 1–9, doi:10.1038/s41598-019-48552-z.

27. Valletta, A.; Gaucci, P.; Mariucci, L.; Fortunato, G.; Templier, F. "Hump" Characteristics and Edge Effects in Polysilicon Thin Film Transistors. *J. Appl. Phys.* **2008**, *104*, doi:10.1063/1.3050323.

Chapter 5

Conclusion

5.1. Findings of this study

Chapter 2. Development and analysis of the SnO_x material for p-type channel TFT application

In this chapter, we developed the deposition process of the SnO_x films for p-type channel TFT application. Process window is very narrow due to the contribution of the Sn and SnO_2 components with n-type conductivity, and therefore the composition ratio between SnO with p-type conductivity and n-type components should be well controlled and optimized. The fundamental instability of SnO_x with high density of holes limits the possibility of synthesis at high oxygen flows and at high annealing temperature leading to oxidation to Sn^{4+} and formation of SnO_2. The optimal deposition parameters were found being: $R[O_2]$ = 8%, P_{Dep} =1.0 Pa with the annealing in the N_2 atmosphere for 1 h, with the highest Hall mobility of 1.65 cm^2/Vs and density of holes 5×10^{17} cm^{-3}. In order to improve the p-type properties we attempted to deposit the SnO_x in a hydrogen-containing atmosphere. Hydrogen doping resulted in a redistribution of the ratio of Sn/SnO/SnO_2 components, as was evaluated by HAXPES. Thus, H incorporation suppressed the metal Sn phase promoting additional V_{Sn} formation and V_{Sn}-H complexes, which both exhibit p-type conductivity. Furthermore, the average transmittance in the visible range was increased by 17% compared to hydrogen-free SnO_x film. However, it was found that undesired development of SnO_2 also occurred in the hydrogen-doped SnO_x presumably due to increased OH groups which can lead to additional oxidation, as was found by TDS analysis. Therefore, the SnO_x doping by H can reduce the point defects including V_{Sn} and V_O compensating the undesired impact of additionally formed n-type SnO_2, and TFT performance with μ_{FE} of 2.59 cm^2/Vs can be obtained. Nevertheless, further research on improving the transfer characteristics, namely μ_{FE}, V_{th}, and S.S. should be continued, to obtain comparable values as n-type devices.

Chapter 3. Low-temperature activation mechanism in Hydrogen-doped In-Ga-Zn-O films for flexible device applications

In Chapter 3, the mechanisms of defect passivation and carrier reduction in Hydrogen-doped In-Ga-Zn-O (IGZO:H) films upon low-temperature annealing for flexible device applications were investigated. *In-situ* Hall measurement results revealed that the activation temperature for conventional IGZO films should be higher than > 240 ˚C to properly reduce defects such as oxygen vacancies especially near the Fermi level, through the oxidation caused by oxygen diffusion from ambient atmosphere, as was revealed by HAXPES analysis. Incorporation of H into the IGZO film resulted in a significant decrease in the oxygen diffusion start temperature from 240 °C to approximately 100 °C, and diffusion start temperature strongly correlates with the H content in the film. In addition, the results of time-dependence annealing in air at 150 °C showed the decrease in the initial slope of the N_e decrease, suggesting higher oxygen diffusion coefficient for higher H content in the film. HAXPES results showed that the near E_F defects of the H doped IGZO film after low-temperature annealing at 150 °C were comparable to that of the conventional IGZO film annealed at 300 °C. This indicates that the near E_F defects can be effectively reduced by the enhanced oxygen diffusion at low temperature. XRR analysis revealed structural changes upon H incorporation which resulted in a decrease in the film density, which might be the reason facilitating the oxygen diffusion into the bulk region at low temperature. However, the hydrogen doping has a stronger effect on the change in carrier density compared to the change in film density upon low-temperature annealing. Therefore, additional studies are needed to establish the relationship between structural and electrical changes in hydrogen-doped IGZO films to further improve controllability. We believe that hydrogen introduction into the IGZO films holds promise for low-temperature applications, such as flexible electronics.

Chapter 4. Hydrogenated polycrystalline n-type IGO:H for high-mobility TFTs

In Chapter 4, the properties of n-type IGO:H films and the effect of H originating from the TFT fabrication process were investigated. In-O_x based materials were found to be very sensitive to the residual water content in the vacuum chamber. Deposition at a higher base pressure (P_{base}) leads to formation of a strained layer due to vapor phase crystallization. This layer results in reduced mobility over the entire annealing temperature. In addition, deposition using a liquid nitrogen trap and with QMS control of residual water (P_{H2O}) revealed that even a slight reduction in P_{H2O} leads to a 1-3% decrease in crystallite size in as-deposited films. As a consequence, it is assumed that the density of the nuclei increases. Further, it was found that heating the substrate for IGO film deposition leads to increase in the P_{base} and P_{H2O} due to desorption. Thus, these three parameters (T_{sub}, $P_{base,}$ and P_{H2O}) are inextricably linked and it is difficult to unambiguously identify the effect of T_{sub} on grain growth. In contrast, IGO deposition in a hydrogen-containing atmosphere can suppress the crystallization by changing the nuclei density and resulting in the higher volume fraction toward amorphous phase. Polycrystalline IGO:H film can be achieved through solid-phase crystallization at a temperature of > 200 ˚C with an average grain size of 0.87 – 1.57 μm depending on the process. Furthermore, H doping can significantly reduce the N_e by more than two orders of magnitude to < 5×10^{17} cm^{-3}, and it is possible to obtain TFT with the μ_{FE}, V_{th}, and S.S. of 60 cm^2/Vs , - 2.7 V, and 0.04 V, respectively. However, due to H and H_2O influence on the crystallization, transfer of optimal parameters of the IGO film synthesis to another equipment is limited and requires a separate optimization. Analysis of the effect of TFT fabrication steps on the IGO:H channel after SPC revealed increased desorption of OH and O groups within temperature range of 100-500 ˚C. These groups formed due to the low-temperature TEOS-based CVD process of SiO_2. Thus, the additional diffusion of H and the formation of a parasitic channel in the region of the back-channel can deteriorate the TFT characteristics. Extra annealing step at 500 ˚C after CVD improved the V_{th} and S.S., but degrades the μ_{FE}. Finally, the sensitivity of IGO films to the TEOS process is higher due to the presence of H/H_2O than that of IGZO, and requires additional investigation and optimization.

5.2. Summary

The purpose of this study was to investigate the effects of H_2 doping to improve the electrical properties of OSs, to establish the mechanism of H influence in p- and n-type materials, and to determine the positive and negative effects of H addition both on the film and device properties.

From the research results described in Chapter 2, the evaluation of the bulk structure using HAXPES revealed that H_2 doping can suppress the Sn-metal phase formation and promote point defects termination, improving the mobility of holes from 1.1 cm^2/Vs to 1.5 cm^2/Vs in p-type SnO:H films. On the other hand, the incorporation of H contributes to additional oxidation due to the formation of OH groups, and this formation leads to redistribution of the Sn, SnO, and SnO_2 components in the film. These results show that the Sn valence control is crucial for improving the p-type properties. Fabricated TFTs based on p-type SnO:H demonstrated μ_{FE} of 2.59 cm^2/Vs.

In Chapter 3, we clarified the mechanism causing low-temperature activation (T_A) of IGZO:H films. Activation of IGZO occurs at >240 ˚C through oxygen diffusion (O_{Dif}) and subsequent oxidation, which plays an important role in carrier density control and defect reduction. We demonstrated that the T_A of IGZO:H films is caused by a decrease in the temperature at which O_{Dif} into the film begins. T_A correlates with the H content and can be reduced up to 100 ˚C. Film density of the IGZO:H decreased with an increase in $R[H_2]$ which would be the possible cause for facilitating the O_{Dif} at low temperature. Thus, defects near the Fermi level can be effectively decreased by O_{Dif} at low temperature, making IGZO:H films suitable for flexible electronics.

In Chapter 4, we found that the H_2 doping can suppress the crystallization during the IGO:H film deposition, polycrystalline films through SPC at 250 ˚C can be achieved, and carrier density can be reduced to $< 5\times10^{17}$ cm^{-3}. Poly-IGO:H based TFT with a μ_{FE} of 60 cm^2/Vs was demonstrated. In addition, increased sensitivity to both residual H_2O and H/OH groups was found, which can have a negative impact on the TFT performance during device fabrication. Thus, research in the field of *In-O_x* based materials should be continued, to improve the controllability and stability.

We do hope that the above results will contribute to the further development and expansion of the oxide semiconductor materials for their use in the next generation of displays.

Research Achievements

Papers

1. R. Velichko, Y. Magari, H. Makino, and M. Furuta, “Investigation of the effect of adding a moderate amount of hydrogen on the properties of tin oxide films deposited by DC magnetron sputtering”, Japanese Journal of Applied Physics, 60, 055503 (2021). https://doi.org/10.35848/1347-4065/abf49d
2. R. Velichko, Y. Magari, and M. Furuta, “Defect Passivation and Carrier Reduction Mechanisms in Hydrogen-Doped In-Ga-Zn-O (IGZO:H) Films upon Low-Temperature Annealing for Flexible Device Applications”, Materials 2022, 15, 334. https://doi.org/10.3390/ma15010334

Conference Presentations

1. R. Velichko, Y. Magari, and M. Furuta, “Investigation of SnO films deposited by DC reactive magnetron sputtering”, The 7th International Symposium on Frontier Technology (ISFT2019), Pataya, Thailand, Aug. 23-26 2019 (Oral).
2. R. Velichko, Y. Magari, and M. Furuta, “Low-temperature activation mechanism in Hydrogen doped In-Ga-Zn-O films for flexible device applications”, The 69th Spring Meeting of the Japan Society of Applied Physics, Sagamihara Campus, Aoyama Gakuin University & Online, March 22-26, 2022, 25p-E202-4 (Oral - Online).
3. Mamoru Furuta, Kenta Shimpo, Taiki Kataoka,Daiki Tanaka, Toshihiro Matsumura, Yusaku Magari, Rostislav Velichko, Daichi Sasaki, Emi Kawashima, Yuki Tsuruma, “High Mobility Hydrogenated Polycrystalline In-Ga-O (IGO:H) Thin-Film Transistors formed by Solid Phase Crystallization”, SID Symposium Digest of Technical Papers, 52(1) 69-72, May, 2021.

Acknowledgments

First and foremost, I would like to express my enormous gratitude to my supervisor *Prof. Mamoru Furuta*, for giving me the opportunity to take this PhD journey at Kochi University of Technology. Thanks to his guidance, my perspective and thinking style have changed from a practically oriented, due to the impact of previous 6 years of company work experience, to a more detailed, close, and in-depth analysis. Discussions with him always opened up new questions and details that were not initially visible and obvious. His "hawkeyed" at the obtained results is something that always inspires and encourages to continue investigation and research. I now have a better understanding that these aspects are necessary and key in an academic approach to research. In addition, the opportunity for practical application of skills, namely working in a clean room, using and handling equipment, and making structures in-house, also allowed me to realize and utilize my engineering potential. This inspires to continue in the semiconductor technology field.

I am thankful to *Prof. Norbert Fruehauf, Prof. Hisao Makino, and Prof. Hiroshi Furuta* for their great help, valuable advices, suggestions, and feedback during carrying out this study. Especially in terms of skills and the ability to learn the XPS analysis and data processing.

Special thanks to *Prof. Eugeny Ryndin* from Saint Petersburg Electrotechnical University "LETI", whose contribution to semiconductor and device physics studies in 2011-2012 made a huge impact and allowed me to benefit from the knowledge I gained from his courses.

I am also very grateful to all the staff members of the International Relations Center, for kind support, adaptation, guidance, assistance, interesting events, hard work and commitment.

I am very thankful to *Prof. Gordon Bateson* and *Prof. Paul Daniels* for their help, extremely interesting language courses, which allowed to enhance and improve English proficiency level. Moreover, special thanks for their friendly, helpful, and always open communication.

Thanks to all of my friends and lab members. *S G Mehadi Aman* for his helpful and sensible clean room tips that allowed me to quickly start my research in the first month. *Yusaku Magari and Daichi Koretomo* who have always been helpful in literally every aspect of both research and everyday life in Japan. *Adam Pander and Vladislav Gamaleev* for amazing and funny time, friendly discussion, support, and guidance throughout this study. As well as many other friends and colleagues I have been fortunate enough to meet and get to know over these three years.

Last but not least, I am eternally grateful to my parents, my brother, my girlfriend, and my Russian friends, whose help, support, inspiration, and patience are hard to overestimate. All of this has helped tremendously in overcoming and coping with the COVID-19 during this study.

New knowledge and skills I acquired during this Doctoral Program will forever remain in my memory and will always be associated with my professor, our laboratory, friends which I met here, and KUT.

Kochi University of Technology,

Graduate School of Engineering

2022 March 17